Simulation of the electron dynamics of chiral systems in CEP-stabilized, intense laser fields

Dissertation

(kumulativ)

zur Erlangung des akademischen Grades doctor rerum naturalium
(Dr. rer. nat.)

vorgelegt dem Rat der Chemisch-Geowissenschaftlichen Fakultät der
Friedrich-Schiller-Universität Jena
von Matthias Paul, M. Sc.
geboren am 11.04.1990 in Greiz

Gutachter:

1. Prof. Dr. Stefanie Gräfe, Friedrich-Schiller-Universität Jena, DE

2. Prof. Dr. Gerhard G. Paulus, Friedrich-Schiller-Universität Jena, DE

Tag der Verteidigung: 17.07.2019

Abstract

The ionization of randomly oriented chiral molecules by circularly polarized light leads to a photoelectron angular distribution (PAD) with a characteristic forward-/backward asymmetry along the propagation direction of the laser field. The effect is known as photoelectron circular dichroism (PECD) and has been experimentally observed for many molecules. A few years ago, PECD has been experimentally observed in the multiphoton regime, investigating the organic molecules camphor and fenchone. A detailed theoretical analysis of the underlying ionization process of these molecules remains challenging, as too many degrees of freedom on different time scales are involved. Using numerical model systems of reduced complexity represents a computationally affordable way to model complex physical phenomena such as PECD. However, modeling of the photoelectron momentum distribution (PEMD) requires at least the solution of the electronic 3D time-dependent Schrödinger equation (TDSE), since the 3D-PEMDs are needed to calculate the forward-/backward asymmetry. Solving the 3D TDSE is computationally demanding, and the resulting 3D-PEMDs are very complex and difficult to analyze.

In this work, the propagation direction of the electric field (z) is therefore neglected, focusing on the ionization dynamics within the xy-plane, in which the electric field vector rotates. The molecular system is described by a 2D charge distribution lying in the xy-plane, consisting of three different nuclei and a single active electron. The ionization dynamics of such triatomic systems is simulated by means of various numerical models,

employing different approximations, which are outlined in the following.
By solving the electronic TDSE, the time-dependent electronic density at specific times and the 2D-PEMD are calculated to study the ionization dynamics for both symmetric (all nuclear charges are equal) and asymmetric (all nuclear charges are differing) triatomic model systems. The results of the TDSE for model systems with different ranges of the potential, orientations and internuclear distances are analyzed by means of classical trajectories (SMM) and different versions of the SFA. Circular dichroism in the angular distribution of photoelectron (CDAD) spectra are calculated via the difference of the PEMDs induced by left- and right-circularly polarized electric fields.
The threefold structure of the PEMDs obtained by fully ab-inito quantum dynamical methods is analyzed by means of classical trajectories. Its origin is traced back to three primary ionization events, occurring at different tunnel exits at either of the three nuclei. For Coulomb-like systems, a clockwise rotation of the threefold structure was observed, which is successfully reproduced by both approximative methods, the CTMC method and the extended strong-field approximation (SFA) [where ionization occurs via a bound superposition state, consisting of the first three eigenstates]. These findings indicate that both the excited states and the long-range Coulomb interaction induce the same clockwise rotation.
For short-range potentials and large internuclear distance, a different ionization mechanism was proposed, where the ionization takes place from the excited state at the nuclei from the so-called "up-field site" of the electric field vector. This ionization mechanism is simulated by means of classical trajectories with modified initial conditions, showing a very good agreement with TDSE simulations. Only the extended SFA is able to reproduce the results of the TDSE simulation correctly, indicating the importance of excited states during ionization of systems with large internuclear distance.
Additionally, in this work the effect of averaging over the molecular ori-

entation has been investigated. It was shown for symmetric systems that the threefold structure in the PEMD disappears in randomly orientated molecular arrangements and the spectrum only depends on electric field parameters, such as the CEP and the pulse duration.
For symmetric systems, the PEMDs induced by LCP and RCP fields are mirror images of each other. The symmetry relation between both PEMDs vanishes for asymmetric nuclear configurations. The PEMDs of asymmetric Coulomb systems, could only be reproduced by the CTMC method in the tunnel-regime for wavelengths of $\lambda = 3000$ nm. The simulation of the PEMDs of asymmetric Coulomb systems by means of CTMC was not successful in the multiphoton-regime ($\lambda = 800$ nm) as many excited states contribute to the ionization process. The averaged PEMDs and thus the CDAD spectra of the symmetric and asymmetric Coulomb-like systems generally exhibit the same features, indicating that the CDAD effect is primarily produced by the CEP of the laser field and not by the asymmetry of the potential.
The results presented in this thesis provide an important precursor to reveal sensitive details of the ionization mechanism underlying the PECD effect. An extension of the 2D-model to 3D, which includes the propagation direction of the electric field and a fourth nucleus, is straight-forward (examples of 3D simulations can be found in the Appendix.), but exceeds the scope of this thesis.

Table of Contents

List of Figures

List of Abbreviations

PEMD	Photoelectron Momentum Distribution
PAD	Photoelectron Angular Distribution
PECD	Photoelectron Circular Dichroism
TDSE	Time-Dependent Schrödinger Equation
CDAD	Circular-Dichroism in the Angular Distribution of Photoelectron
SFA	Strong-Field Approximation
CTMC	Classical Trajectory Monte-Carlo
CEP	Carrier Envelope Phase
LCP	Left Circularly Polarized
RCP	Right Circularly Polarized
SMM	Simple Man's Model
SPM	Saddle-Point Method
ATI	Above-Threshold Ionization
PES	Photoelectron Energy Spectrum
ITM	Imaginary Time Method
COLTRIMS	Cold-Target-Recoil Ion Momentum Spectroscopy
VMI	Velocity-Map Imaging
ATD	Above-Threshold Detachement
QQES	Quasistationary Quasienergy State
VUV	Vacuum Ultraviolet
CD	Circular Dichroism
REMPI	Resonance-Enhanced Multiphoton Ionization
MP	Multiphoton
HHG	High Harmonic Generation
DFT	Discrete Fourier Transforms
FFTW	Fastest Fourier Transform in the West
ITP	Imaginary Time Propagation
CVA	Coulomb-Volkov Approximation
RT-TDDFT	Real-Time Real-Space Time-Dependent Density Functional Theory

OBI	Over-the-Barrier Ionization

Chapter 1

Introduction

Soon after the invention of the laser in 1960, high intensities of coherent electromagnetic radiation became accessible, and highly non-linear optical effects in atoms and molecules were observed for the first time in experiments. Examples are ionization of Xe atoms [1] and H_2 molecules via seven- and nine-photon absorption [2].
A central idea for the theoretical description of such processes, suggested by Reiss in 1962, was to describe the wavefunction of an field-dressed electron continuum via Volkov functions $\psi_{\mathbf{p}}^{\mathbf{s}}(\mathbf{r},t)$ [3, 4]. Volkov functions are solutions of the time-dependent Schrödinger equation (TDSE) of a free electron in the presence of a laser field (within the electric dipole approximation) at time t:

$$\psi_{\mathbf{p}}^{\mathbf{s}}(\mathbf{r},t) = \frac{1}{2\pi^{3/2}} \mathrm{e}^{\mathrm{i}\mathbf{s}\mathbf{r} - \frac{\mathrm{i}}{2}\int_{-\infty}^{t}[\mathbf{p}+\mathbf{A}(\tau)]^2 \mathrm{d}\tau} \tag{1.1}$$

where $\mathbf{r}$ is the electron's position, $\mathbf{p}$ represents its canonical momentum, which characterizes the Volkov function $\psi_{\mathbf{p}}^{\mathbf{s}}(\mathbf{r},t)$ [atomic units are used throughout the thesis explicitly unless stated otherwise], $\mathbf{A}$ is the vector potential of the electric field and $\mathbf{s}$ depends on the chosen gauge: with $\mathbf{s} = \mathbf{p}$ and $\mathbf{s} = \mathbf{p} + \mathbf{A}(t)$ for velocity and length gauge, respectively. This ansatz paved the way for the development of non-perturbative theories to describe the interaction between strong electric laser fields with matter via analytical expressions to describe the transition from bound atomic states to the continuum. This framework was limited to approximate ionization rates, in which long-range Coulomb-interaction of the photoelectron with its parent ion and scattering phenomena are not taken into account. Consequently, the theory can only describe systems bound by zero-range potentials interacting with a circularly polarized field. For such systems, the interaction between the parent ion and the electron can be approximately neglected once it is emitted [5].
For linearly polarized monochromatic fields, where scattering processes may occur, and atoms, where the Coulomb-potential causes long-range interactions, ionization rates can not be derived analytically anymore and a non-perturbative approach is needed. One

ansatz was proposed by Keldysh [6],

$$M_k(\mathbf{p}) = -\mathrm{i}\int_{-\infty}^{+\infty} \langle \psi_{\mathbf{p}}^{\mathbf{s}} | \hat{V}_{int}^{\mathbf{s}}(\mathbf{r},t) | \tilde{\psi}_0 \rangle \mathrm{d}t \tag{1.2}$$

where $\hat{V}_{int}^{\mathbf{s}}$ describes the electronic interaction with the laser-field, which reads in the velocity and length gauge as $\hat{V}_{int}^{\mathbf{p}}(\mathbf{r},t) = \mathbf{p}\mathbf{A}(t) + \frac{1}{2}\mathbf{A}^2(t)$ and $\hat{V}_{int}^{\mathbf{p}+\mathbf{A}(t)}(\mathbf{r},t) = \mathbf{r}\mathbf{E}(t)$ [7,8]. Here, the ionization process is described via a transition from a field-free bound state wave function $\tilde{\psi}_0(\mathbf{r},t)$ with ionization potential I_p

$$\tilde{\psi}_0(\mathbf{r},t) = \psi_0(\mathbf{r})\mathrm{e}^{\mathrm{i}I_p t} \tag{1.3}$$

into the Volkov function $\psi_{\mathbf{p}}$ (continuum state). Employing this ansatz, Keldysh derived an analytical expression for the ionization amplitude in the length gauge. The obtained ionization probability describes systems bound by a so-called zero-range potential, as the transition occurs from the bound ground state to a potential-free continuum.
The derived ionization amplitude $M_k(\mathbf{p})$, Eq. (1.2), was evaluated by the saddle-point method (SPM) [9],

$$\begin{aligned} M_k(\mathbf{p}) &\approx \sum_\alpha \sqrt{\frac{2\pi}{\mathrm{i}\ddot{S}_0(t_{\mathbf{s}\alpha})}} P(\mathbf{p}, t_{\mathbf{s}\alpha}) \mathrm{e}^{-\mathrm{i}S_0(\mathbf{p},t_{\mathbf{s}\alpha})} \\ P(\mathbf{p},t) &= -\frac{\mathrm{i}}{(2\pi)^{3/2}} \int \mathrm{d}\mathbf{r} [\mathrm{e}^{-\mathrm{i}\mathbf{s}\mathbf{r}} V_{int}^{\mathbf{s}}(\mathbf{r},t)\psi_0(\mathbf{r})] \\ S_0(\mathbf{p},t) &= \int_t^\infty [\mathbf{p} + \mathbf{A}(\tau) + I_p] \mathrm{d}\tau, \end{aligned} \tag{1.4}$$

where the saddle points $t_{\mathbf{s}\alpha}$ satisfy the equation

$$\dot{S}_0 \equiv \frac{\partial S_0}{\partial t} = 0, \tag{1.5}$$

where $\mathbf{s}$ depends on the chosen gauge and S_0 is the Volkov-phase.
The ionization probability w_k consists of a prefactor B_k and an exponential factor and was derived via Eq. (1.4) for small momenta, corresponding to the maximum of the ionization probability [10]:

$$w_k = B_k \mathrm{e}^{-2\frac{I_p}{\omega} f_k(\gamma)} \tag{1.6}$$

The exponential part of w_k was found to be correct. The pre-exponential factor B_k on the other hand, does not reproduce the correct asymptotic behavior of the field-dressed

Coulomb-potential [11] since the long-range Coulomb interaction of the photoelectron with its parent ion is disregarded. Therefore, the application is limited to short-range potentials. In Eq. (1.6), f_k is known as the Keldysh function

$$f_k(\gamma) = \left(1 + \frac{1}{2\gamma^2}\right) \text{arcsinh}\gamma - \frac{\sqrt{1+\gamma^2}}{2\gamma}, \tag{1.7}$$

which depends on the Keldysh parameter γ [6]

$$\gamma = \sqrt{2I_p}\omega/E_0, \tag{1.8}$$

where E_0 is the electric field amplitude. The dimensionless Keldysh parameter γ represents one of the most fundamental parameters in strong field physics, allowing to assign the ionization process to the predominant strong-field regime. In the tunnel-regime where $\gamma \ll 1$, the frequency ω of the laserfield is low (typically in the mid-IR regime), while the field amplitude E_0 is high ($\sim 10^{13}$-10^{15} W/cm^2). The oscillation of the strong laser field is sufficiently slow so that at each time step a quasi-static potential barrier is created, which allows for ionization through tunneling (see left panel Fig. 1.1). This regime is often referred to as "quasistatic regime". In the so-called multiphoton regime ($\gamma \gg 1$) on the other hand, ionization occurs vertically via absorption of multiple photons since the tunnel-barrier is extremely short lived due to its very fast oscillation, rendering tunneling less probable [10].

The Keldysh ansatz was later derived from solutions of the TDSE [12], employing the following two approximations:

1. The electric field amplitude of the laser field E_0 is small compared to the atomic field: $E_0/(2I_p)^{3/2} \ll 1$.

2. The effective Coulomb potential is assumed to be short-ranged.

Later, the results found by Keldysh were generalized in a closed-form analytic expression to calculate photoelectron spectra and total ionization rates for linear and elliptically polarized fields. Thereby, new phenomena such as above-threshold-ionization (ATI) peaks were theoretically predicted [12–16]. These ATI peaks are separated by the photon energy and only occur in photoelectron energy spectrum (PES), when the system absorbs more photons than the minimum required number to ionize. However, at that time, the available intensities of the laser-fields of $10^{10} - 10^{11}$ W/cm^2 were insufficient to record the second and higher ATI peaks in the PES, and only the theoretically predicted angular distributions and the total ionization rates were measurable. The former is affected by ponderomotive scattering (see below: indirect electrons) and the latter strongly depends on the pre-factor of the ionization amplitude w_k, see Eq. (1.6). For an accurate calculation

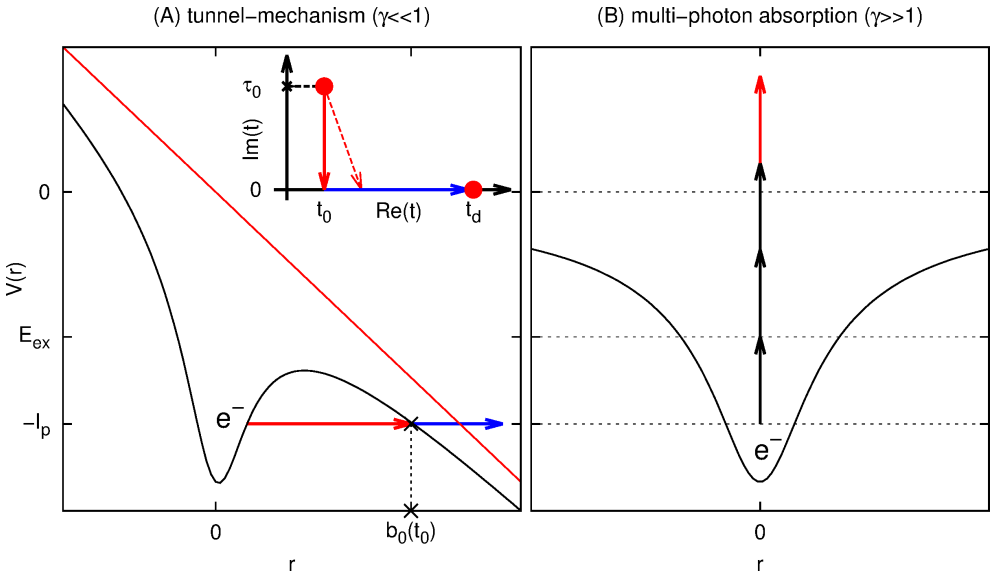

Figure 1.1: Schematic representation of the different tunnel-mechanisms. (A) Shown is the field-dressed (red line: $\mathbf{rE}$) Coulomb potential $V(\mathbf{r})$ with the red and blue arrow representing the sub-barrier ($t \in [t_0 + i\tau_0, t_0]$) and the "after" barrier motion ($t \in [t_0, t_d]$). The sub-barrier motion is related to the imaginary time τ_0 and ends at time t_0 at the classical tunnelexit $\mathbf{b}_0$. (B) Shown is ionization of the electron via multiphoton absorption; vertical arrows are representing the photons, while the red arrow is related to Above-threshold ionization. I_p is the ionization potential and E_{ex} corresponds to the energy of an arbitrary excited state.

of both, ionization rates and angular distributions, the standard Keldysh theory has to be extended to incorporate the Coulomb-interaction of the photoelectrons with their parent ion.

For this purpose, the imaginary time method (ITM) was applied, allowing for the interpretation of the Keldysh theory in terms of classical electron trajectories propagating in complex time (known as quantum trajectories or quantum orbits [17, 18]). If the complex phase in the ionization amplitude oscillates fast in time, the SPM method can be applied and the time integral in Eq. (1.2) can be replaced by a sum, see Eq. (1.4), over all saddle-point solutions $t_{s\alpha}$ of Eq. (1.5) in the upper complex half-plane ($\mathrm{Im}S_0(\mathbf{p}, t_s) > 0$). This result of the SPM can be presented in terms of classical trajectories $\mathbf{r}_\mathbf{p}(t)$

$$\mathbf{r}_\mathbf{p}(t) = \frac{\partial S_0}{\partial \mathbf{p}} = \int_{t_s}^{t} [\mathbf{p} + \mathbf{A}(\tau)]\mathrm{d}\tau = \mathbf{p}(t - t_s) + \int_{t_s}^{t} \mathbf{A}(\tau)\mathrm{d}\tau, \tag{1.9}$$

with initial (at time t_s) and final condition (at time t_d) according to: $\mathbf{r}_\mathbf{p}(t_s) = 0$, $\mathbf{v}_\mathbf{p}(t_s) = (\mathbf{p} + \mathbf{A}(t_s))\sqrt{-2I_p}$ and $\mathbf{v}_\mathbf{p}(t_d) = \mathbf{p}$. The exponential part of the ionization

amplitude, see Eq. (1.4), S_0 is defined by a classical action which satisfies Newton's equation of motion for an electron in an electric field $\mathbf{E}(t)$:

$$\ddot{\mathbf{r}}_{\mathbf{p}}(t) = -\mathbf{E}(t) \tag{1.10}$$

The initial time t_s is determined through the SPM, Eq. (1.5). The most probable final momentum $\mathbf{p}_m$, which corresponds to the peak maximum in the spectrum, is related to the smallest imaginary part of the action:

$$\frac{\mathrm{d}}{\mathrm{d}\mathbf{p}}[\mathrm{Im}(S_0)] \mid_{\mathbf{p}=\mathbf{p}_m} = \mathrm{Im}[\mathbf{r}_{\mathbf{p}_m}(t)] = 0 \tag{1.11}$$

This means that the trajectory with momentum $\mathbf{p}_m(t_d)$ is real-valued and is detected at the real-valued time t_d (see Fig. 1.1) [16, 19, 20]. Within this approach, the Coulomb interaction can be naturally included into the phase S_0. The idea of the Coulomb-corrected ITM (e.g. Coulomb-corrected strong-field-approximation [10]) is now to correct all Coulomb-free trajectories of the ITM model in such a way, that they satisfy Newton's equation in the presence of an Coulomb field in addition to the external laser field. In order to apply the ITM for the calculation of the Coulomb-corrected ionization rate, it is useful to rewrite the action S_0 as a function of $\mathbf{r}_{\mathbf{p}}(t)$:

$$\begin{aligned} -S_0(\mathbf{p}, t_d) =& \int_{t_s}^{t_d} \left(\frac{1}{2}[\mathbf{p} + \mathbf{A}(\tau)]^2 + I_p \right) \mathrm{d}\tau \\ =& \int_{t_s}^{t_d} \left(\frac{1}{2}[\mathbf{p} + \mathbf{A}(\tau)]^2 - \mathbf{E}(\tau)\mathbf{r}_{\mathbf{p}}(\tau) - I_p \right) \mathrm{d}\tau - \mathbf{r}_{\mathbf{p}}(t_d)\mathbf{p} \\ =& W_0[\mathbf{r}_{\mathbf{p}}(t), t_d] - \mathbf{r}_{\mathbf{p}}(t_d)\mathbf{p} \end{aligned} \tag{1.12}$$

If there is an extra force acting on the electron, e.g. due to the interaction of the electron with its parent ion, one can account for it by correcting W_0 and $\mathbf{r}_{\mathbf{p}}(t)$. The Coulomb-corrected trajectories $\mathbf{r}^*_{\mathbf{p}}(t)$ can be found perturbatively [21–23], if the extra force is relatively small, e.g. when the electric field is strong and the Coulomb-interaction of the photoelectron with its parent ion is relatively small. This conditions are typically fulfilled in the tunnel-regime, where the Coulomb-corrected ITM model provides accurate results. However photoelectron spectroscopy experiments at that time were only available in the multiphoton regime ($\gamma \approx 30$) [1].

To overcome this limitation, the theory has to be extended to the multiphoton regime. To this end, Faisal (1970s) derived a more general expression for the ionization amplitude. Here, the final state was not limited to one specific state, e.g. continuum state which is described by a plane wave. Thus, the theory goes beyond the standard Volkov approximation,

in which the continuum is described via plane waves [24]. Another ansatz, developed by Reiss in the 80s, was based on the S-matrix formalism [25]. Nevertheless, both generalized approaches (Faisal and Reiss) led to the same approximative pre-exponential factor, which is still limited to systems bound by short-range potentials. Furthermore, both theories achieved gauge invariance only in the limit of zero-range potentials [10]. The discrepancy between the theoretical approach being limited to the tunnel regime and experiments limited to the multiphoton regime, was the reason why the Keldysh theory was not used during this period of time.
It took until 1979 before the first theoretically predicted ATI peaks in a photoelectron spectrum could be recorded [26]. The ATI with energies E_n peaks were separated by the photon-energy ω as predicted by the Keldysh theory. However, in contrast to the Keldysh theory, the observed energies E_n of the n-th ATI peaks were found to be independent of the laser-intensity [26]. According to the energy conservation law,

$$E_n = \frac{\mathbf{p}_n^2}{2} = n\omega - I_p - U_p \tag{1.13}$$

the energy E_n depends on the ponderomotive energy U_p of the electric field (with amplitude E_0)

$$U_p = \frac{E_0^2}{4\omega^2}(1+\epsilon^2), \tag{1.14}$$

where ϵ defines the polarization of the electric field with $\epsilon = 0$ for linear and $\epsilon = \pm 1$ for right- and left- circularly polarized electric fields, respectively. The ponderomotive energy is defined as the averaged kinetic energy of a free electron over one laser period in the given time interval T [10]:

$$\begin{aligned} \left\langle \frac{\mathbf{v}_p^2}{2} \right\rangle_T &= \frac{1}{2}\left\langle [\mathbf{p} + \mathbf{A}(t)]^2 \right\rangle_T \\ &\approx \frac{\mathbf{p}^2}{2} + \underbrace{\frac{1}{2}\left\langle \mathbf{A}(t)^2 \right\rangle_T}_{U_p} \end{aligned} \tag{1.15}$$

The Keldysh theory is usually derived within the dipole approximation [$\mathbf{E}(\mathbf{r},t) \approx \mathbf{E}(t)$: see Sec. 2.1.3], in which the electric field is assumed to be spatially homogeneous over the size of the atomic or molecular system. However, in real experiments, the laser pulse features a spatial intensity profile $I(\mathbf{r})$. Here, the laser intensity decreases from its maximum at the center of the laser focus, $\mathbf{r}_0$, to zero, at $\mathbf{r}_{end}$. If the pulse duration lasts long enough, so that the electron can travel out of the focus before the field is off, the electron experiences a ponderomotive acceleration corresponding to a change of its

canonical momentum $\mathbf{p}$. For laser pulses with small focal spot radius $\mathbf{r}_f$ and long pulse duration τ, so that $\tau \gg \mathbf{r}_f/p$ is satisfied, the photoelectron energy E_f observed at the detector does not depend on the laser intensity anymore [27, 28]:

$$E_f = n\omega - I_p. \tag{1.16}$$

Consequently, the Keldysh theory is limited to electric fields with relative short laser-pulse durations. In the early 1980s, the durations of these pulses were simply too long $10^{-8} - 10^{-10}$ s (with $\mathbf{r}_f \approx 10^{-3}$ cm) and Keldysh theory was not applicable to these kind of electric fields.
Soon after the invention of the chirped pulse amplification method in the mid-1980s [29], femtosecond lasers with high intensities up to 10^{16} W/cm^2 (CO_2 laser) and short pulse durations down to 1 ps became available [30], thus allowing to reach the desired strong field regime ($E_0^2/\omega^3 \gg 1$) as well as the tunnel-regime ($\gamma \ll 1$). Both regimes were reached first with CO_2 lasers and later with infrared lasers with wavelengths of approximately 1 μm [31]. From the experimental point of view the pulse durations of the electric fields became smaller and smaller, which lead to an increasing influence of the carrier envelope phase (CEP) on the ionization dynamics. For the theoretical simulation of, for example, photoelectron momentum distribution via the Keldysh theory and Eq. (1.2) for extremely short pulses of only a low number of optical cycles, one must know the exact shape of the vector potential $|\mathbf{A}_c(t)| \propto E_0/\omega \cos(\omega t + \phi_{CEP})$, including its CEP ϕ_{CEP} (ω is the laser-frequency) [32]. From the experimental point of view, it is very difficult to measure the absolute CEP of the electric field with high precision, while an accurate metrology is needed to compare theory with experiment. In a statistical approach (shot-to-shot analysis), the influence of the absolute phase on the intense-field ionization was firstly demonstrated experimentally [33] in 2001, while the found relation can be used to determine the absolute phase of the electric field.
With this important experimental advancement, the standard Keldysh theory, which neglects scattering effects, provides a commonly accepted physical picture, in which the ionization process can be interpreted as a two step sequence [10]:

1. tunneling of the electron through the static barrier created by the electric field

2. propagation of the free photoelectron in the continuum

With the further development of photoelectron diagnostic methods, such as cold-target-recoil ion momentum spectroscopy (COLTRIMS) [34], three dimensional momentum distribution of multiple charged particles can be measured in coincidence. Also, the combination of tomographic reconstruction methods with velocity-map-imaging (VMI)

techniques allows to measure the 3D-momentum distribution of photoelectrons [35]. New features appeared in these spectra, which could not be explained within the standard Keldysh model. They can be traced back to different shortcomings of the Keldysh theory and are grouped in three major categories:

1. The Coulomb interaction between the photoelectron and the parent ion is neglected. Such a Coulomb interaction causes asymmetries for example in the photoelectron angular distributions in elliptically polarized fields [36]. As stated before, Coulomb-effects can be included within the ITM ansatz. This Coulomb correction in the phase of the ionization amplitude, Eq. (1.4), can lead to significant changes in the ionization rate. In Ref. [16], the Coulomb-corrected ITM was applied to the calculation of the total ionization rate of the atoms in the tunnel limit $\gamma \ll 1$. An analysis by Perelomov and Popov showed, that the Coulomb field significantly enhances the ionization rate by several orders of magnitude and is thus not negligible. The effect was confirmed experimentally [37]. In experiment, several other features were observed in the photoelectron momentum distribution, including Coulomb asymmetry in elliptically polarized light [36, 38, 39], cusps and double-hump structures [40–42], low-energy structures [43–47], and side lobes [48]. Within the Coulomb-corrected ITM model, all of these effects could be reproduced successfully.

2. A variety of effects are caused by laser-driven recollision [49, 50]. The standard Keldysh theory is not able to describe the rescattering mechanism, including its role in the generation of high-order harmonics, high energy photoelectron plateaus, and nonsequential double ionization. Rescattering phenomena offer also a great tool for probing the atomic and molecular structure. An extension of the Keldysh theory by including scattering effects is straight-forward [51–53]. The method is known as the extended strong-field approximation (SFA), or alternatively, as SFA with rescattering. The SFA will be discussed in Sec. 2.3.1.

3. The Keldysh model only considers transitions from the electronic groundstate. The influence of transiently populated excited states is neglected and resonances with the electric field are not included (e.g. multiphoton ionization: Fig. 1.1, right-hand side). So-called Freeman resonances [54] with excited states for example can generate an intensity-independent fine structure in the ATI peaks, which can not be described with the standard Keldysh model. Including further bound states into the Keldysh theory seems to be a difficult task. However, methods like the dressed-state SFA were developed, in which excited states were approximately included [55]. Fortunately, the application of few-cycle laser pulses with a broad spectrum reduces the influence

of such excited states since transient resonances are suppressed by spectrally broad fields [10].

In general, the standard Keldysh theory without Coulomb-correction is limited to short-range systems. Therefore, the strong-field detachment of negative ions offers a suitable area of application of the standard Keldysh-theory, since the interaction of the photoelectrons with neutral molecules is relatively short-ranged [56]. In the past, high resolution above-threshold-detachement (ATD) spectra of H^-, Br^-, and F^- were recorded with mid-infrared laser pulses [57–61]. Theoretical calculation could successfully reproduce the energy structure of the spectrum, while for the high energy part a good agreement was only achieved when scattering processes were taken into account [62]. To describe such scattering processes, advanced methods are required, e.g. the quasistationary quasienergy state (QQES) [63].
A more intuitive approach to study scattering phenomena is provided by the simple man's model (SMM). Here, the dynamics following the initial ionization step is modeled via selected classical trajectories [50], [64–66]. The initial values for the classical trajectories can be derived from the ITM model. As stated above, the starting point t_s of the complex-valued trajectories are obtained via the SPM. The final momenta $\mathbf{p}$ at a time t_d can then be obtained by solving Newton's equation of motion, with the integration path connecting t_s with t_d being chosen arbitrarily (see Fig. 1.1, left panel). Naturally, the path can be separated into a sub-barrier ($t \in [t_0 + i\tau_0, t_0]$) and an "after" barrier motion ($t \in [t_0, t_d]$) with t_0 being a vertical segment (parallel to the axis of the imaginary part) of the time path, connecting the complex-valued time t_s with its purely real valued component $t_0 = \mathrm{Re}[t_s]$. Within the SMM, the imaginary part of t_s is assumed to be negligibly small and the sub-barrier part of the motion (electron tunnels through the static barrier created by the electric field) is reduced to an instantaneous emergence of the electron at the tunnel exit b_0 [67] with a given ionization probability w_k (see Fig. 1.1, left panel). In the quasistatic limit at time t_0, the classical tunnelexit (tunnelbarrier) can be calculated analytically [68]:

$$\mathbf{b}_0 \equiv \lim_{\gamma \to 0} \mathbf{b} = -\frac{I_p \mathbf{E}(t_0)}{\|\mathbf{E}\|^2 (t_0)}. \tag{1.17}$$

The time the electron takes along the imaginary axis to cover the distance through the barrier with atomic velocity $\mathbf{v}_{at} = \sqrt{2I_p}$ is known as the Keldysh-tunneling time Δt_k

$$\Delta t_k \approx \frac{\mathbf{b}_0 \mathbf{v}_{at}}{\|\mathbf{v}_{at}\|^2}, \tag{1.18}$$

which is related to the imaginary part τ_0 of the saddle point t_s. Only if

$$\mathbf{b}_0 = \mathrm{Re}[\mathbf{r}_0(\mathbf{p}, t_0)] \tag{1.19}$$

is satisfied (with initial velocity of $\mathbf{v}_0 = \mathbf{p} + \mathbf{A}(t_0)$), the SMM and ITM provide similar results: the real part of the initial coordinate condition of the complex trajectories $\mathbf{r}_0(\mathbf{p}, t_0)$ is equal to the classical tunnelexit $\mathbf{b}_0$. Applying the ITM model for a linearly polarized, monochromatic electric field $\mathbf{E}(t) = \mathbf{E}_0 \sin \omega t$, one obtains

$$\begin{aligned} \mathbf{b}_0 =& \mathrm{Re}[\mathbf{r}_0(\mathbf{p}, t_0)] = \frac{\mathbf{E}_0}{\omega^2} \sin(\omega t_0)(\cosh \omega\tau_0 - 1) \\ \mathbf{v}(t_0) =& \mathbf{p} + \mathbf{A}(t_0) = \mathbf{v}_\perp \underbrace{-\frac{\mathbf{E}_0}{\omega} \cos(\omega t_0)(\cosh \omega\tau_0 - 1)}_{=\mathbf{v}_\parallel}, \end{aligned} \tag{1.20}$$

where $\mathbf{v}_\perp$ and $\mathbf{v}_\parallel$ are the vector components of the initial velocity $\mathbf{v}(t_0) = (\mathbf{v}_\parallel(t_0), \mathbf{v}_\perp(t_0))$ of the complex trajectories, pointing either perpendicularly ($\mathbf{v}_\perp$) or parallel ($\mathbf{v}_\parallel$) to the direction of the electric field vector. The coordinate $\mathbf{b}(t_0)$ of the complex trajectories of the ITM model only transforms into the classical tunnelexit $\mathbf{b}_0$ if the condition $\omega\tau_0 \ll 1$ is fullfilled. The SMM is therefore only valid in the tunneling limit. For $\gamma \approx 1$, the ITM and the SMM model differ significantly from each other, and in the multiphoton regime ($\gamma \gg 1$) $\|\mathbf{b}(t_0)\| = \sqrt{2I_p}/\omega$ becomes independent of the time and the electric field $\mathbf{E}(t_0)$ [see Eq. (1.17)]. The initial velocity $\mathbf{v}_0 = (\mathbf{v}_\parallel(t_0), \mathbf{v}_\perp)$ also depends on the ionization-regime. $\mathbf{v}_\parallel(t_0)$ e.g. is an unambiguously defined function of t_0 and vanishes in the tunneling limit: $\lim_{\gamma\to 0} \mathbf{v}_\parallel(t_0) = 0$ [10]. In contrast, $\mathbf{v}_\perp$ depends on the electric field $\mathbf{E}(t_0)$ and an transversal velocity spread at the instant of ionization takes place. The transversal velocity spread follows a Gaussian distribution with a standard deviation $\sigma_\perp = \sqrt{\frac{\|\mathbf{E}(t_0)\|}{2\sqrt{2I_p}}}$, in which the maximum is located at $\mathbf{v}_\perp = 0$ [69], reflecting the quantum mechanical momentum distribution of the electron in the system.

The benefit of the SMM model is the simple intuitive picture it provides of the ionization dynamics in terms of classical trajectories. The classical trajectories can be obtained by solving Newton's equation with initial phase-space coordinates of $\mathbf{v}_0 = (0, \mathbf{v}_\perp)$ and $\mathbf{r}(t_0) = \mathbf{b}_0$ (tunnel exits). Now, the inclusion of Coulomb effects is straight-forward by extending the classical force $\mathbf{F}_c$ acting on the electron in the continuum by the term $V_c(\mathbf{r})$.

$$\mathbf{F}_c = -\mathbf{E}(t) - \nabla V_c(\mathbf{r}) \tag{1.21}$$

$V_c(\mathbf{r})$ is the long-range interaction between the photoelectron and its parent ion and $\nabla = \left(\frac{\partial}{\partial x}, \frac{\partial}{\partial y}, \frac{\partial}{\partial z}\right)^\mathsf{T}$ is the nabla operator. The extension of the classical force F_c is only valid in the tunnel-regime. In the Coulomb-corrected ITM, the path of the complex-valued classical trajectories are not arbitrary anymore and no closed form analytical

expression for the classical action has been derived yet. In principle, there are many solutions of Eq. (1.21), leading to complex-valued trajectories $\mathbf{r}(t)$ with different starting points $\mathbf{r}(t_0) = \mathbf{b}^*(t_0)$ (asterisk indicates the Coulomb-correction). Within the tunneling limit, these trajectories depend only weakly on the value of the initial coordinate $\mathbf{b}^*(t_0)$, which is here chosen to be the tunnelexit $\mathbf{b}_0$. Beyond this limit, i.e. in the non-adiabatic tunneling and the multi-photon regime, the contribution of the sub-barrier motion increases and the trajectories become strongly dependent on $\mathbf{b}^*(t_0)$. Therefore, the Coulomb-corrected version of the ITM and SMM do not necessarily yield the same results in both regimes, rendering the Coulomb-corrected SMM inapplicable in these regimes [10]. However, the Coulomb-corrected SMM provides a great tool to study long-range interactions and recollision processes of photoelectrons by means of classical trajectories [see Sec. (3)] [40, 42, 45, 70–74].

However, within the ITM the trajectories are derived for the initial condition $\mathbf{r}_\mathbf{p}(t_s) = 0$, meaning that these trajectories are starting their evolution in the continuum from only one single center at the origin of the coordinate system. For centrosymmetric systems, such as atomic systems, these initial conditions are a good choice, while for molecular systems, which exhibit more than one center and centrosymmetry is inevitable broken, the condition $\mathbf{r}_\mathbf{p}(t_s) = 0$ is not able to model the complex molecular structure. Even for the simplest diatomic molecule H_2^+, the physics of the ionization dynamics depends strongly on the nuclear geometry and the orientation of the molecule with respect to the laser field [32] and the single-center Keldysh theory immediately lead to wrong results [55].

Examples for complex molecular-specific strong-field phenomena induced by near-infrared and visible laser-fields include charge-resonance enhanced ionization [75, 76] bond softening [77, 78], vibrational trapping (bond hardening) [77–79], and above-threshold dissociation [79]. A transfer of established methods for atomic systems, such as the Coulomb-corrected ITM and the Coulomb-corrected SMM in length gauge, to molecular systems is currently an active area of research. Recently developed approaches are limited to diatomic molecules with large internuclear distances, as the initial state can be approximated by a superposition of two field-dressed atomic wavefunctions (each located at its center), in which the overlap of the two atomic wavefunctions is vanishing [55, 80]. Employing a similar approach to the two molecules O_2 and N_2 [81], Milosevic derived an amplitude via a molecular SFA with field-dressed initial molecular bound states. Here, the length gauge version of the molecular SFA was found to be in good agreement with experimental data, whereas the corresponding velocity-gauge version gives incorrect results, as it generally does for atoms [82]. To describe ionization rates for diatomic molecules with arbitrary internuclear distances, several approximative methods were developed, including the quasistationary quasienergy state (QQES) approach [63], improved versions of the molecular

SFA [81, 83], and extended versions of the SMM [84]. In Ref [84], it was shown, how the three-step tunnel-mechanism of the standard SMM depends on the internuclear distance of the H_2^+ molecule. Depending on the internuclear distance of H_2^+, the electron either escapes from the "up-field" ($R_{up} < 0$) or the "down-field" ($R_{do} > 0$) side (see. Fig. 1.2) of the diatomic molecule, which eventually leads to different ionization dynamics and thus different photoelectron momentum distributions (PEMDs).

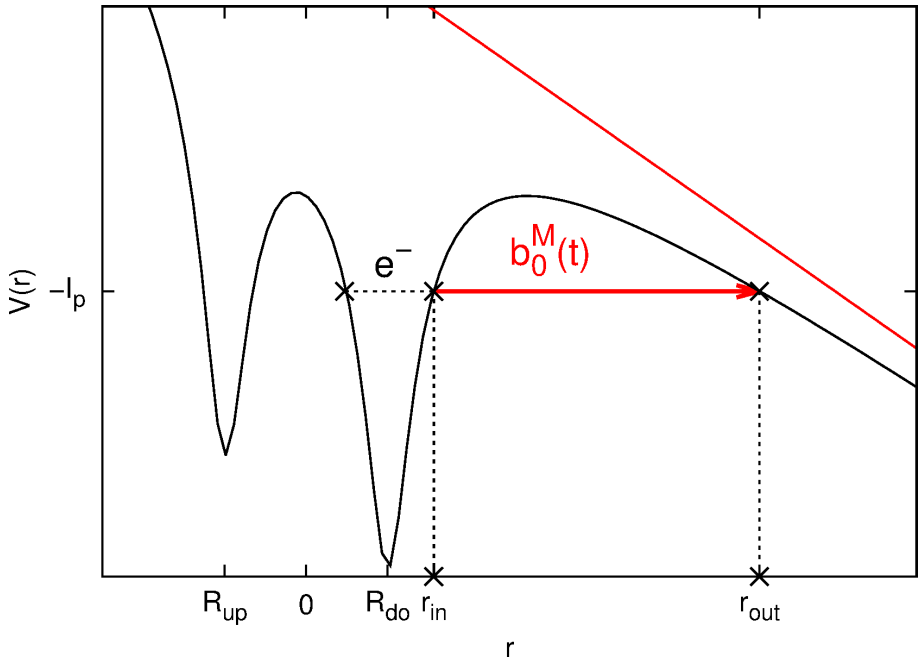

Figure 1.2: Schematic representation of the tunnel-mechanism in a H_2^+-like model potential $V(\mathbf{r})$, where ionization occurs from the groundstate of the system at the "down-field" ($R_{do} > 0$) side of the electric field vector $\mathbf{E}(t)$ [red line: $\mathbf{rE}(t)$]. Also shown is the width of the quasistatic tunnel barrier $b_0^M(t) = \|\mathbf{r}_{out} - \mathbf{r}_{in}\|$ at a certain time t, which is represented by the red arrow. $R_{up} < 0$ is related to the position of the nuclei at the "up-field" side, and I_p corresponds to the ionization potential.

Due to the ever increasing power of computing resources and the great success of theories like the SFA, the ionization behavior of larger molecules can be studied numerically [85–89]. Within the framework of the SFA, photoelectron angular distributions (PAD) of polyatomic molecules have been successfully calculated [90–92]. PADs of randomly orientated molecules show interesting features. For example, the ionization of randomly orientated chiral molecules (molecules without improper rotation axes) ionized by circularly polarized light yields PADs with a characteristic forward-/backward asymmetry along the propagation direction of laserfield [93, 94]. The effect is known as photoelectron circular dichroism (PECD). The asymmetry changes its sign upon change of the rotation direction of the circularly polarized laserfield (left to right and vice versa) or upon change

of the chirality of a molecule (left-handed enantiomer vs. right-handed enantiomer). Both enantiomers have the same number of atoms of each element, but their absolute arrangement differs, resulting in either left-(S) or right-(R) handed chirality (see Fig. 1.3). Nevertheless, both enantiomers are mirror images of each other and are therefore non-superposable [95].

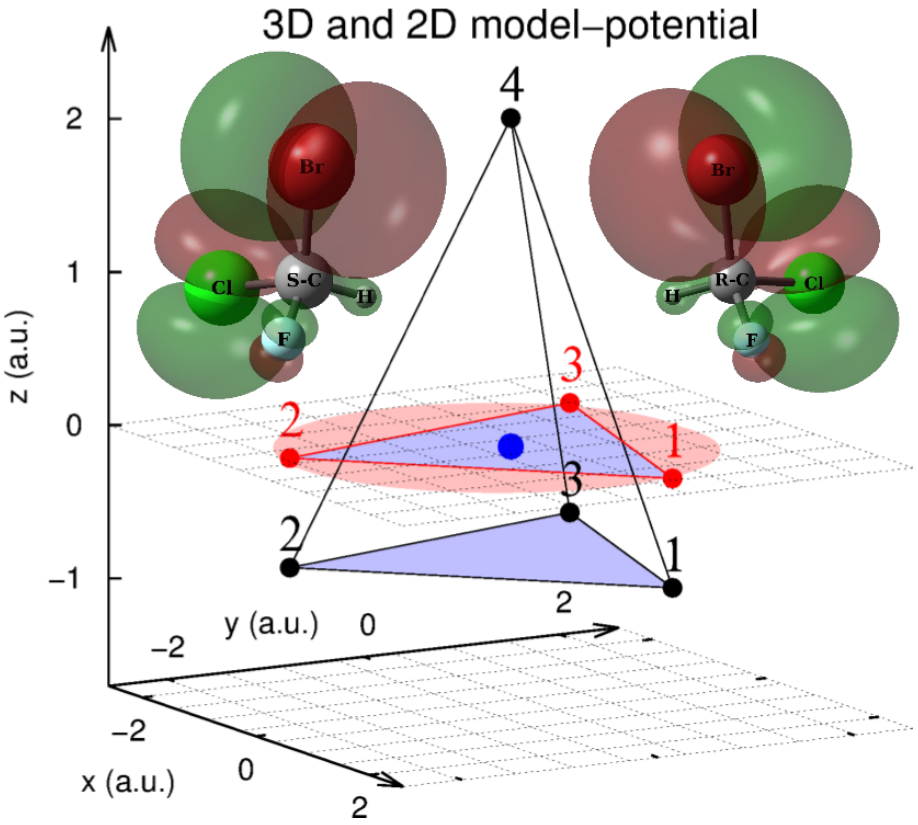

Figure 1.3: Shown are both, the S and the R handed enantiomers of the chiral molecule Bromochlorofluoromethane CHBrClF and a schematic representation of their highest occupied molecular orbitals. By comparison, the 3D (black: tetrahedron structure) and the 2D model (red: triangular structure) are presented. The points marked with the n-th number belong to the n-th nucleus of the respective model system, while the electron of each model system (blue point) is located at the origin of the coordinate system $\mathbf{r} = (0, 0, 0)$.

While sharing many physical and chemical properties, such as melting and boiling point, the absorption maxima, the vibrational spectra, and the viscosity, enantiomers can differ significantly in their chemical reactivity [96]. For example, the interaction of chiral drugs with the corresponding chiral receptors depends on the handedness of the enantiomer (examples can be found in Ref [97]), giving rise to different reactions in living organism. The latter highlights the importance of developing ultrasensitive methods for analyzing

and characterizing chiral molecules [35]. Here, the PECD provides a great spectroscopic tool to study chiral molecules in the gas phase. Compared to the optical CD-effect, where the difference in the photoabsorption spectra are relatively small ($\Delta\mathrm{OD} = 10^{-5}$), the PECD effect is two to three orders of magnitudes larger and is thus more sensitive [93]. Here, forward-/backward asymmetries (along the propagation direction of the electric field) up to 20 % could be measured in PEMDs generated via one photon ionization by vacuum ultraviolet (VUV) synchroton radiation [98–101]. The PECD effect can be explained by the electric dipole effects only, without the need to include weaker magnetic dipole effects. In 1976, Ritchie theoretically described PECD by calculating differential photoionization cross sections of chiral molecules interacting with circularly polarized light. The resulting angular distributions $I(\theta)$ of photoelelectrons were expressed in terms of Legendre-polynomials P_L,

$$I(\theta) = \sum_L b_L P_L(\cos\theta), \tag{1.22}$$

where θ is the polar angle relative to propagation direction of the electric field and b_L is the expansion coefficient. Ritchie showed for randomly orientated chiral molecules, that the first term of the odd Legendre-polynomials b_1 does not vanish, in contrast to non-chiral molecules. This remaining asymmetry (after averaging over all molecular orientation) is konwn as PECD [93].

Following Ritchie's analysis, the asymmetry in the photoelectrons of lactid acid and glyceraldehyd was numerically calculated by Powis. The latter is konwn as circular-dichroism in the angular distribution (CDAD) of photoelectrons. It was shown, that CD effects can also occur in aligned achiral molecules, if the molecular arrangement and the electric field define three non-coplanar vectors (propagation direction of the photon/electric field and the photoelectron and the molecular axis of the space-fixed molecule), where chirality is achieved through experimental configuration [102]. Examples of such systems include CO molecules adsorbed on a surface with fixed orientation [103] and aligned NO molecules [104–107].

Recently, it has been experimentally observed that PECD can also occur via few photon-ionization from strong UV-vis laser pulses: the organic molecules camphor and fenchone were ionized by a strong-field few-cycle circularly polarized laser pulses width wavelengths of 398 nm and a pulse duration of 25 fs via a 2+1 resonance-enhanced multiphoton ionization (REMPI) process. Asymmetries of 10% could be recorded by means of the VMI method with table top setups [108]. In principle, the ionization occurs via a resonant two-photon absorption, followed by a single photon absorption to the continuum. Several theoretical studies aim to simulate the multiphoton (MP) PECD and its complex ionization mechanism [109–111]. Full numerical treatment without approximations is only possible

for prototype molecules such as H_3^{2+}, the smallest non-colinear molecule [112, 113]. However, such single-electron molecules do not provide any information on multi-electron effects. Yet they provide important insights into fundamentals of strong-field effects.
The replacement of real molecules with numerical model systems of reduced complexity represents a computationally affordable way to model complex physical phenomena such as PECD. A the minimal model system consists of a single active electron interacting with an intense, circularly polarized laser field and an asymmetric charge environment, mimicking the chiral molecule. The asymmetric charge environment can be achieved through four nuclei with different charges. The three dimensional ionization dynamics [$\mathbf{r} = (x, y, z)^\intercal$] of a single active electron can thus be simulated via the time-dependent wavefunction $\psi(\mathbf{r}, t)$, which can be obtained by solving the time-dependent Schrödinger equation (TDSE) numerically. However, solving the TDSE in 3D is computationally very demanding and the corresponding 3D-PEMD are very complex and difficult to analyze. Within the project presented in this thesis, complexity was further reduced by restricting the time-dependent simulation to a 2D plane perpendicular to the propagation direction of the electric field (z). To this end an effective 2D charge distribution (see Fig. 1.3) of three nuclei was applied to an single active electron. The primary object of the research project presented in this thesis is to examine the ionization dynamics of such tri-atomic model systems. Therefore, the SFA and the corresponding SMM (Keldysh theory) were applied to study the influence of bound electronic states and the Coulomb interaction during the ionization process. However, a comprehensive simulation of PECD would requires 3D-models since the forward/backward asymmetry occurs in the propagation direction of the electric field (z component). Such an extension of the 2D-model would be straight-forward (preliminary results of the 3D simulations can be found in the Appendix), but exceed the scope of this research project. However, the results presented in this thesis provide an important precursor to reveal the exact ionization mechanism behind the PECD effect.
The thesis is structured as follows: In Section 2 the theoretical background of the applied methods will be presented. The results will be shown in Section 3 in form of the article reprints that were published in international peer-reviewed scientific journals. A short summary will be given preceding each article. Finally, a comprehensive summary in Section 4 will discuss and combine all findings of the individual articles.

Chapter 2

Theory

This chapter gives an overview of the approximations (Sec. 2.1), numerical methods (Sec. 2.2) and Keyldish models (Sec. 2.3), which were employed to simulate and analyze the strong-field driven dynamics of triatmomic model moelcules (Sec. 3).

2.1 Light-matter interaction

2.1.1 Classical theory

An accurate description of the laser-matter interaction requires the correct treatment of both the quantum nature of the electron and the electric field. If the number of photons is sufficiently large (such as in an macroscopic laser field), the electromagnetic field can be treated classically and is described via Maxwell's equation, neglecting effects like quantum fluctuations and spontaneous emission [114]. Within Maxwell's equations, the electric field $\mathbf{E}$ and the magnetic field $\mathbf{B}$ can be expressed through the vector potential $\mathbf{A}$ and the scalar electric potential U:

$$\begin{aligned} \mathbf{B} =& \nabla \times \mathbf{A} \\ \mathbf{E} =& -\frac{\partial}{\partial t}\mathbf{A} - \nabla U, \end{aligned} \tag{2.1}$$

Expressed in terms of $\mathbf{A}$ and U, Maxwell's equations in vacuum can be written as second order (in space and time) wave equations:

$$\begin{aligned} \Delta U + \frac{\partial}{\partial t}\left(\nabla \cdot \mathbf{A}\right) =& -\frac{1}{\varepsilon_0}\rho(\mathbf{r}) \\ \left(\frac{1}{c^2}\frac{\partial^2}{\partial t^2} - \Delta\right)\mathbf{A} + \nabla\left(\nabla \cdot \mathbf{A} + \frac{1}{c^2}\frac{\partial}{\partial t}U\right) =& \frac{1}{c^2\varepsilon_0}\mathbf{j}(\mathbf{r}), \end{aligned} \tag{2.2}$$

where $\rho(\mathbf{r})$ and $\mathbf{j}(\mathbf{r})$ are the stationary charge and current density respectively, c is the speed of light, ε_0 is the vacuum permittivity and $\Delta = \left(\frac{\partial^2}{\partial x^2} + \frac{\partial^2}{\partial y^2} + \frac{\partial^2}{\partial z^2}\right)$ is the Laplace

operator. The electric potentials U and $\mathbf{A}$ are not uniquely defined; there exists an infinite number of potentials U and A that yield the same electromagnetic field. These electric potentials are related via gauge transformation:

$$\begin{aligned} \mathbf{A}(\mathbf{r},t) &= \mathbf{A}(\mathbf{r},t) + \nabla F(\mathbf{r},t) \\ U(\mathbf{r},t) &= U(\mathbf{r},t) - \frac{\partial}{\partial t} F(\mathbf{r},t), \end{aligned} \tag{2.3}$$

Here, $F(\mathbf{r},t)$ represents a regular scalar (arbitrary) function. This "degree of freedom" allows to choose F via a gauge condition to simplify the second-order wave equation 2.2. For electrodynamics of non-relativistic classical particles, one common choice is the Coulomb gauge: $\nabla \cdot \mathbf{A} = 0$ [115]. Thus, Maxwell's equation can be rewritten:

$$\begin{aligned} \Delta U(\mathbf{r},t) &= -\frac{1}{\varepsilon_0}\rho(\mathbf{r},t) \\ \frac{\partial^2}{\partial t^2}\mathbf{A}(\mathbf{r},t) - c^2\Delta\mathbf{A}(\mathbf{r},t) &= \frac{1}{\varepsilon_0} j(\mathbf{r},t) - \nabla\frac{\partial}{\partial t}U(\mathbf{r},t) \end{aligned} \tag{2.4}$$

According to the Maxwell's equation, the electric field $\mathbf{E}$ is generated by a stationary charge-density $\rho(\mathbf{r})$ and depends on the position $\mathbf{r}_i(t)$ of the i-th point particle with charge q_i

$$\begin{aligned} \nabla \cdot \mathbf{E}(\mathbf{r},t) &= \frac{1}{\varepsilon}\rho(\mathbf{r},t), \\ \rho(\mathbf{r},t) &= \sum_{i=1}^{n_p} q_i \delta(\mathbf{r} - \mathbf{r}_i(t)), \end{aligned} \tag{2.5}$$

where n_p is the total number of considered point-particles and ε is the absolute permittivity. In contrast, the magnetic field $\mathbf{B}$ is induced by charge in motion and thus, depending on the current density $\mathbf{j}(\mathbf{r})$, which is related to the velocity $\mathbf{v}_i(t)$ of the particles.

$$\begin{aligned} \nabla \times \mathbf{B}(\mathbf{r},t) &= \frac{1}{c^2}\frac{\partial}{\partial t}\mathbf{E}(\mathbf{r},t) + \frac{1}{\varepsilon_0 c^2} j(\mathbf{r},t). \\ \mathbf{j}(\mathbf{r},t) &= \sum_{i=1}^{n_p} q_i \mathbf{v}_i(t)\delta(\mathbf{r} - \mathbf{r}_i(t)), \end{aligned} \tag{2.6}$$

The non-relativistic dynamics of the point particles in an external electromagnetic field are governed by Newton-Lorentz equation [116, 117]:

$$m_i \frac{\mathrm{d}^2\mathbf{r}_i(t)}{\mathrm{d}t^2} = q_i(\mathbf{E}(\mathbf{r}_i(t),t) + \mathbf{v}_i(t) \times \mathbf{B}(\mathbf{r}_i(t),t)) \tag{2.7}$$

Thus, the classical particle's trajectories $\mathbf{r}_i(t)$ with their intitial position $\mathbf{R}_i = \mathbf{r}_i(t_0)$ and velocity $\mathbf{V}_i = \mathbf{v}_i(t_0)$ at time t_0 are solutions of Eq. (2.7). The evolution of the electromagnetic field [Eq. (2.4)] can also be described via the Lagrange formalism [118]

$$\frac{\mathrm{d}}{\mathrm{d}t}\frac{\partial \mathcal{L}}{\partial \dot{\mathbf{r}}_i} - \frac{\partial \mathcal{L}_i}{\partial \mathbf{r}_i} = 0, \tag{2.8}$$

where $\mathcal{L} = \mathcal{T} - \mathcal{V}$ is the Lagrangian, with $\mathcal{T}$ and $\mathcal{V}$ being the kinetic and potential energy. The Lagrangian for an electromagnetic field can be defined [117] via integration over its density $\mathcal{L}_\epsilon$:

$$\int \mathrm{d}\mathbf{r}\mathcal{L}_\epsilon = \underbrace{\frac{\epsilon_0}{2}\int \mathrm{d}\mathbf{r}[\mathbf{E}^2(\mathbf{r}) - c^2\mathbf{B}^2(\mathbf{r})]}_{=f_{ext}} + \int \mathrm{d}\mathbf{r}[\mathbf{j}(\mathbf{r})\cdot\mathbf{A}(\mathbf{r}) - \rho(\mathbf{r})U(\mathbf{r})] \tag{2.9}$$

The coupling between the n_p non-relativistic free particles and the electromagnetic field can be described via the full Lagrangian $\mathcal{L}_{ip+\epsilon}$:

$$\mathcal{L}_{ip+\epsilon} = \frac{1}{2}\sum_{i=1}^{n_p} m_i\mathbf{v}_i^2 + \int \mathrm{d}\mathbf{r}\mathcal{L}_\epsilon \tag{2.10}$$

The Euler-Lagrangian equation of motion [Eq.(2.8)] are hence given by Newton-Lorentz [Eq.(2.7)] with dynamical variables of $\mathbf{r}, \dot{\mathbf{r}}$) and Maxwell's equations [Eq.(2.3)] with dynamical variables of $\mathbf{A}, U$). Within the external field approximation, the electromagnetic interaction is not mutual anymore: only the electromagnetic field affects the particle, the backreaction of the particle on the field is neglected ($f_{ext} = 0$) [117].

$$\mathcal{L}_{ip+\epsilon} = \frac{1}{2}\sum_{i=1}^{n_p} m_i\mathbf{v}_i^2 + \int \mathrm{d}\mathbf{r}[\mathbf{j}(\mathbf{r})\cdot\mathbf{A}_{ext}(\mathbf{r}) - \rho(\mathbf{r})U_{ext}(\mathbf{r})] \tag{2.11}$$

Here, U_{ext} and $\mathbf{A}_{ext}$ are the scalar and vector potential of the external electromagnetic field. By applying the Legendre transformation [117]

$$\mathcal{H}(\mathbf{r}_1, \cdots, \mathbf{r}_l, \mathbf{p}_1, \cdots, \mathbf{p}_l) = \sum_{i=1}^{l}\dot{\mathbf{r}}_i - \mathcal{L} = \mathcal{T} + \mathcal{V}, \tag{2.12}$$

the Hamiltonian $\mathcal{H}$ for a single particle interacting with an external electromagnetic field can be obtained from the associated Lagrangian $\mathcal{L}_{ip+\epsilon}$ within the external field approximation:

$$\mathcal{H} = \frac{1}{2}[\mathbf{p} - q\mathbf{A}_{ext}]^2 + qU_{ext}, \tag{2.13}$$

where $\mathbf{p}$ is defined as the conjugate momenta $\mathbf{p} = m\mathbf{v} + q\mathbf{A}_{ext}$.

2.1.2 Quantum theory

The equations of motion in Sec. 2.1.1 can be quantized in the usual canonical quantization. Since the classical treatment of the electromagnetic field via Maxwell equation [see Eq. (2.2)] is accurate enough (as state above), only the single particle described by Newton-Lorentz equation, Eq. (2.7) has to be treated quantum mechanically. Here, the dynamical variables $\mathbf{r}$ and $\mathbf{p}$ become operators with commutator relations according to: $[\hat{r}_i, \hat{r}_j] = 0, [\hat{p}_i, \hat{p}_j] = 0$ and $[\hat{r}_i, \hat{p}_j] = \mathrm{i}\delta_{ij}$. $|\mathbf{r}\rangle$ represents a vector in Hilbert space, describing the quantum state of the system in coordinate space. The momentum $\hat{\mathbf{p}} = -\mathrm{i}\nabla$ for the quantum Hamiltonian can be obtained from the commutation relations and the eigenvalue equation of the position operator $\hat{\mathbf{r}}$: $\hat{\mathbf{r}}|\mathbf{r}\rangle = \mathbf{r}|\mathbf{r}\rangle$. The dynamics of the wavefunction in coordinate space is given by the TDSE (projected to coordinate space: $|\psi\rangle = \int \mathrm{d}\mathbf{r}\psi(\mathbf{r})|\mathbf{r}\rangle$):

$$\mathrm{i}\frac{\partial}{\partial t}\psi(t,\mathbf{r}) = \hat{H}(t)\psi(t,\mathbf{r}) = (\hat{H}_0 + \hat{V}_{int}(t))\psi(t,\mathbf{r}) \tag{2.14}$$

The Hamiltonian operator $\hat{H}$ can be obtained from the classical Hamiltonian $\mathcal{H}$ (see Eq. 2.13) with coordinate $\hat{\mathbf{r}} \to \mathbf{r}$ and momentum $\mathbf{p} \to -\mathrm{i}\nabla$. The wave equation describes the quantum dynamics of a single free particle with field-free time-independent Hamiltonian $\hat{H}_0$, interacting with an time-dependent electromagnetic field $\hat{V}_{int}(t)$. A general solution of the TDSE can be written as

$$\begin{aligned} |\psi(t)\rangle =& \hat{U}(t,t_0)|\psi(t_0)\rangle \\ =& \hat{T}_o \mathrm{e}^{-\mathrm{i}\int_{t_0}^{t}\hat{H}(t')\mathrm{d}t'}|\psi(t_0)\rangle. \end{aligned} \tag{2.15}$$

Here, t_0 and t are the initial and final times, $\hat{T}_o$ is the time-ordering operator (only required when the Hamiltonians $\hat{H}(t)$ at different times t do not commute) and $\hat{U}(t,t_0)$ is the time evolution operator [117]. For a time-independent Hamiltonian $\hat{H}$, the evolution operator takes the following form [119] (in the basis of its eigenfunctions $\{\psi_n\}$):

$$U(t,t_0)|\psi(t_0)\rangle = \sum_n \mathrm{e}^{-\mathrm{i}E_n(t-t_0)} \underbrace{\langle\psi_n|\psi(t_0)\rangle}_{c_n(t_0)} |\psi_n\rangle \tag{2.16}$$

Here, the evolution depends only on the eigenenergies E_n and eigenstates ψ_n of the considered system with coefficients $c_n(t_0)$ at time t_0.

2.1.3 Dipole approximation

If the wavelength of the electromagnetic field λ is much larger than the dimension of the system D ($\lambda \gg D$), the spatial variation of the electromagnetic field over the size

of the quantum system is very small and can thus be neglected. The long-wavelength approximation is only valid if the change of the electric field $\Delta\mathbf{E}(z,t)$ as function of the coordinate z [120] (propagation direction of the field along the k_z-vector)

$$\Delta\mathbf{E}(z,t) \approx D\frac{\partial}{\partial_z}\mathbf{E}(\omega t - k_z z)|_{z=0} \approx Dk_z \left\|\mathbf{E}\right\| = D\frac{\omega}{c}\left\|\mathbf{E}\right\| \tag{2.17}$$

is relatively small and the following condition is satisfied:

$$\omega D \ll c \longleftrightarrow \Delta E \ll \left\|\mathbf{E}\right\|, \tag{2.18}$$

i.e., if the frequency of the laserfield ω is sufficiently small. Within the long-wavelength approximation, the vector potential can be defined as follows:

$$\mathbf{A}(\omega t - kz) \approx \mathbf{A}(\omega t) + \frac{z}{c}\mathbf{E}(\omega t) \tag{2.19}$$

Only if the magnetic field $\mathbf{B}$ is negligible, the dipole approximation is valid and the spatial dependence in the vector potential can be dropped: $\mathbf{A}(\mathbf{r},t) \approx \mathbf{A}(t)$. However, the magnetic field can only be neglected if the displacement vector of an electron δ is smaller than the size of the system: $\delta \ll D$. The displacement vector δ is connected to Lorentz-equation $\left\|\mathbf{F}_{mag}\right\| = \left\|\mathbf{v}\right\| \left\|\mathbf{B}\right\| = \left\|\mathbf{a}_{mag}\right\|$ the force of the magnetic field $\mathbf{F}_{mag}$ acts on the electron, leading to an acceleration $\mathbf{a}_{mag}$ and thus a change in the trajectory of the electron. Consequently, the magnetic field can only be neglected if the electric field satisfies the following equation:

$$\left\|\mathbf{E}\right\| \ll c\omega\sqrt{\frac{d}{\lambda}}, \tag{2.20}$$

Since the electric fields (E_0=0.02 a.u.$\rightarrow I = 1.4 \cdot 10^{15}$ W / cm^2, $\lambda = 800$ nm) used for the calculation presented in Sec. 3 do no reach the limit $I \approx 8c\omega^3 = 7 \cdot 10^{15}$ W / cm^2 where magnet fields become relevant [121], the dipole approximation is valid.
By setting $U = 0$ (for details see ref [122]), the velocity-gauge Hamiltonian [see Eq. (2.13)] for one single electron ($q = -1$) in the dipole approximation is given by

$$\hat{H}^v = \frac{1}{2m}[\mathbf{p} + \mathbf{A}_{ext}(t)]^2 + V_c(\mathbf{r}). \tag{2.21}$$

Here, the Coulomb potential $V_c(\mathbf{r})$ describes the interaction between the electron and the parent ion via Coulomb's law. In this work, the used model system consists of one electron with coordinate $\mathbf{r}$ and three frozen nuclei (no nuclear dynamics) with charge Z_i and position $\mathbf{R}_i$. The corresponding potential $V_c(\mathbf{r})$ of the system is defined as:

$$V_c(\mathbf{r}) = \underbrace{\sum_{i=1}^{3}\sum_{j>i}^{3}\frac{Z_i Z_j}{|\mathbf{R}_i - \mathbf{R}_j|}}_{=V_{nn}} \underbrace{-\sum_{i}^{3}\frac{Z_i}{\sqrt{(\mathbf{r}-\mathbf{R}_i)^2+\alpha}}}_{=V_{en}}, \tag{2.22}$$

where α is the softening parameter, which was introduced to avoid singularity [117].

2.1.4 Gauge invariance

The gauge principle states that all physically meaningful (measurable) observables (Hermitian operator, which act on the Hilbert space) are gauge invariant. Two wavefunctions, $\psi^{(1)}$ and $\psi^{(2)}$ in gauge 1 and 2 are connected via local unitary transformation G [117] (F_g is a real-valued arbitary function):

$$\psi^{(1)}(\mathbf{r}) = G\psi^{(2)}(\mathbf{r}) = \mathrm{e}^{-\mathrm{i}F_g}\psi^{(2)}(\mathbf{r}) \tag{2.23}$$

The corresponding two observables $\hat{O}^{(1)}$ and $\hat{O}^{(2)}$ are only gauge invariant if they satisfy the equation (unitary transformation):

$$\hat{O}^{(1)} = G\hat{O}^{(2)}G^{-1} \tag{2.24}$$

As a result, the expectation values become independent of the chosen gauge.

$$\langle\hat{O}^{(1)}\rangle = \langle\psi^{(1)}|\hat{O}^{(1)}|\psi^{(1)}\rangle = \langle\psi^{(1)}|G\hat{O}^{(2)}G^{-1}|\psi^{(1)}\rangle = \langle\psi^{(2)}|\hat{O}^{(2)}|\psi^{(2)}\rangle = \langle\hat{O}^{(2)}\rangle \tag{2.25}$$

For the two Hamiltonians $\hat{H}^{(1)}$ and $\hat{H}^{(2)}$ in gauge 1 and 2, respectively, two separate TDSE equations can be formulated:

$$\begin{aligned}\mathrm{i}\frac{\partial}{\partial t}|\psi^{(1)}(t)\rangle &= \hat{H}^{(1)}(t)|\psi^{(1)}(t)\rangle \\ \mathrm{i}\frac{\partial}{\partial t}|\psi^{(2)}(t)\rangle &= \hat{H}^{(2)}(t)|\psi^{(2)}(t)\rangle\end{aligned} \tag{2.26}$$

By using these TDSEs, along with the definion of the unitary transformation, Eq. (2.23), a relation between the two Hamiltonians $H^{(1)}$ and $H^{(2)}$ can be derived:

$$\hat{H}^{(2)} = G\hat{H}^{(1)}G^{\dagger} + \mathrm{i}\hbar\frac{\partial G}{\partial t}G^{\dagger} \tag{2.27}$$

Only if the second term of Eq. (2.27) vanishes and Eq. (2.24) is satisfied, gauge invariance is achieved and the energy expectation value becomes independent of the chosen gauge:

$$\langle\psi^{(2)}|\hat{H}^{(2)}(t,t_0)|\psi^{(2)}\rangle = \langle\psi^{(1)}|H(t,t_0)^{(1)}|\psi^{(1)}\rangle + \mathrm{i}\langle\psi^{(2)}|\frac{\partial G}{\partial t}|\psi^{(1)}\rangle. \tag{2.28}$$

Physical observables, which are given in terms of transition amplitudes, are invariant under unitary transformation and satisfy the gauge principle:

$$\langle\psi^{(1)}(t)|\hat{U}^{(1)}(t,t_0)|\psi^{(1)}(t_0)\rangle = \langle\psi^{(2)}(t)|\hat{U}^{(2)}(t,t_0)|\psi^{(2)}(t_0)\rangle, \tag{2.29}$$

where $\hat{U}^{(1)}(t,t_0)$ and $\hat{U}^{(2)}(t,t_0)$ are the time-evolution operator in gauge 1 and 2, see Eq. (2.15). Many physical observables are related to transition amplitudes. High Harmonic Generation (HHG) experiments, for example, are related to photon emission transition moments, and PEMDs are a consequence of ionization, i.e. a transition from bound to continuum states [123, 124].
By applying a unitary transformation $G^{vl}(t) = \mathrm{e}^{-\mathrm{i}\mathbf{A}_{ext}(t)\mathbf{r}}$ to $\hat{H}^v$ [Eq. (2.21)] with the corresponding transformation of the vector potential $F_g = \mathbf{A}_{ext}(t)\mathbf{r}$ [Eq. (2.23)] and $\mathbf{E} = \partial_t\mathbf{A}$ (Eq. (2.1) with $U = 0$), the length gauge Hamiltonian $\hat{H}^l$ for one single electron ($q = -1$) can be obtained:

$$H^l = \frac{\mathbf{p}^2}{2} + \mathbf{r}\mathbf{E}_{ext}(t) + V_c(\mathbf{r}) \tag{2.30}$$

Physical observables, which are related to transition amplitudes, can be calculated via the velocity (Hamiltonians $\hat{H}^v$) and the length gauge (Hamiltonians $\hat{H}^l$) version of the TDSE. Both representations describe the same physics, and physical observables such as dipole moments, velocities, and accelerations are equal to both gauges. However, when approximations (e.g. the strong-field-approximation (SFA)) of gauge-dependent quantities are involved, the gauge invariance of physical observables may get lost, if the error induced by the approximation scheme does not transform in the same way as the full solution [117].

2.2 Numerical methods

The solution of the TDSE, Eq. (2.15), the time-dependent wavefunction $\psi(\mathbf{r}, t)$, can be calculated numerically on a discrete grid. The implementation of such methods can be divided in four steps: representation, initiation, Hamiltonian operation, and time propagation [125]. Each of these steps will be described in detail in the subsequent sections.

2.2.1 Representation

Quantum mechanical wavefunctions $|\psi\rangle$ are complex vectors defined on the Hilbert space subjected to non-local operators. Representating $|\psi\rangle$ in a spatial and momentum representation, connected via Fourier transform, allows for a localization of such operators. An efficient discretization of phase-space for numerical applications can then be achieved

by using the Fourier method. In the Fourier method, the continuous wavefunction $\psi(\mathbf{r})$ is discretized by a finite set of orthogonal plane-wave functions $g_{\mathbf{k}}(\mathbf{r})$ [125]:

$$\psi(\mathbf{r}) \approx \sum_{n=0}^{N_g-1} a_{\mathbf{k}} \underbrace{\mathrm{e}^{\mathrm{i}2\pi\mathbf{k}_n\mathbf{r}/\mathbf{L}}}_{g_{\mathbf{k}}(\mathbf{r})}, \tag{2.31}$$

where $\mathbf{k}_n$ is the wave-vector grid with N_g grid points and $\mathbf{L}$ is the box-size of the grid. One can use the orthogonality of the Fourier functions with equidistant sampling points to invert the relation and to calculate the coefficients $a_{\mathbf{k}}$

$$a_{\mathbf{k}} = \frac{1}{N_g} \sum_{n=0}^{N_g-1} \psi(\mathbf{r}_n)\mathrm{e}^{-2\mathrm{i}\pi\mathbf{k}\mathbf{r}_n/\mathbf{L}} \equiv \tilde{\psi}(\mathbf{k}_n), \tag{2.32}$$

where $\psi(\mathbf{r}_n)$ is now discretized on a grid $\mathbf{r}_n, n \in [1, N_g]$. The cofficients $a_{\mathbf{k}}$ can be interpreted as the amplitudes of the wavefunction in momentum space $\tilde{\psi}(\mathbf{k}_n)$. In quantum mechanics, the minimum phase space volume, in which a system can be localized, is h^D, where D is the number of degrees of freedom and h is Planck's constant. A discrete representation of the Hamiltonian and the wavefunction is only possible if at least one grid point is located in each phase-space volume h^D. The minimum volume in phase space covered by the Fourier representation should be: $V_{vol} = 2\mathbf{L} \cdot \mathbf{k}_{max}$. Here, the grid points $\mathbf{r}_n = \mathbf{r}_0 + n\Delta\mathbf{r}$ are equidistantly spaced with $\Delta\mathbf{r} = \frac{\mathbf{L}}{N_g-1}$ and the range from $\mathbf{r}_0$ to $\mathbf{r}_0 + \mathbf{L}$, whereas the momentum grid ranges from $-\mathbf{p}_{max}$ to $\mathbf{p}_{max}$. Thus, a condition for the relation between $\Delta\mathbf{r}$ and the maximum wave vector $\mathbf{k}_{max}$ is obtained [125]:

$$\Delta\mathbf{r} = \frac{\pi}{|\mathbf{k}_{max}|} \tag{2.33}$$

Only if the absolutes of the occurring momenta $\mathbf{k}_n$ are smaller than $\mathbf{k}_{max}$, the Hilbert-space is described accurately by a discrete grid. Within Eq. (2.33), the rectangular-shaped momentum grid ($\mathbf{k} \in [-\frac{\pi}{\Delta\mathbf{r}} + \Delta\mathbf{k}, \frac{\pi}{\Delta\mathbf{r}}]$) can be defined

$$\mathbf{k}_n = \begin{cases} n\Delta\mathbf{k} & \text{for } n = 0, \cdots, N_g/2 \\ -(N_g - n)\Delta\mathbf{k} & \text{for } n = N_g/2 + 1, \cdots, N_g - 1 \end{cases}$$

with the stepsize

$$\Delta\mathbf{k} = \frac{2\pi}{N_g\Delta\mathbf{r}} \tag{2.34}$$

If the range of the $\mathbf{k}$-grid is not sufficiently large, the periodic condition of the wavefunction ψ erroneously leads to wavefunctions with opposite momentum:

$$\tilde{\psi}(\mathbf{k}_0 - \mathbf{k}) \equiv \psi(\mathbf{k}_{max} - \mathbf{k}) \tag{2.35}$$

These wavefunctions can interfere with each other causing numerical errors. The advantage of the Fourier method is the efficient computing of discrete Fourier transforms (DFTs), which is implemented via the Fastest Fourier Transform in the West library (FFTW3) [126–128]. This algorithm scales with an order of $N_g \log N_g$ [126], which reduces the computational time significantly.

2.2.2 Hamiltonian operation and time propagation

Many physical situations, including the motion of electrons in strong laserfields, are described using time-dependent Hamiltonians $\hat{H}(t)$. For this particular case, the total evolution operator is divided into short segments Δt, in which the Hamiltonian does not change significantly. The total time evolution operator $\hat{U}(t_N, t_0)$ can be approximated by short-time propagators $\hat{U}(t + \Delta t, t) \approx \mathrm{e}^{-\mathrm{i}\hat{H}(t)\Delta t}$ [125]:

$$\psi(t_N) = \hat{U}(t_N, t_0)\psi(t_0) \tag{2.36}$$

$$\approx \hat{U}(t_N, t_N - \Delta t)\hat{U}(t_N - \Delta t, t_N - 2\Delta t)\ldots\hat{U}(t_0 + \Delta t, t_0)|\psi(t_0)\rangle \tag{2.37}$$

$$\approx \prod_{i=1}^{N} \hat{U}(t_i, t_{i-1})\psi(t_0), \tag{2.38}$$

$$\tag{2.39}$$

The wavefunction $\psi(t_N)$ of the system can then be obtained numerically via Eq. (2.39) in the time interval $[t_0, t_N]$, with N corresponding to the number of time steps. The lower bound for the time-step Δt can obtained from the maximum energy E_{max} occurring in the system. E_{max} corresponds to the fastest oscillating wavepacket and determines the smallest time step $\Delta t < \frac{1}{E_{max}}$ required to resolve its evolution correctly. For the efficient calculation of Eq. (2.39) ($\hat{H} = \hat{V} + \hat{T}$), the propagators of $\hat{V}$ and $\hat{T}$ are evaluated in coordinate and momentum space respectively [125]:

$$\mathrm{e}^{-\mathrm{i}\hat{V}\Delta t}|\psi\rangle = \sum_n \mathrm{e}^{-\mathrm{i}\hat{V}(\mathbf{r}_n)\Delta t}\psi(\mathbf{r}_n)|\mathbf{r}_n\rangle = \begin{bmatrix} \mathrm{e}^{-\mathrm{i}\hat{V}(\mathbf{r}_1)\Delta t}\cdot\psi(\mathbf{r}_0) \\ \mathrm{e}^{-\mathrm{i}\hat{V}(\mathbf{r}_2)\Delta t}\cdot\psi(\mathbf{r}_1) \\ \vdots \\ \mathrm{e}^{-\mathrm{i}\hat{V}(\mathbf{r}_{N_g})\Delta t}\cdot\psi(\mathbf{r}_{N_g-1}) \end{bmatrix}$$

$$\mathrm{e}^{-\mathrm{i}\sum_i |\mathbf{k}_i\rangle\hat{T}(\mathbf{k}_i)\langle\mathbf{k}_i|\Delta t}|\psi\rangle = \begin{pmatrix} \mathrm{e}^{-\mathrm{i}\frac{\mathbf{k}_0^2}{2}\Delta t} & 0 & \cdots & 0 \\ 0 & \mathrm{e}^{-\mathrm{i}\frac{\mathbf{k}_1^2}{2}\Delta t} & 0 & \vdots \\ \vdots & 0 & \ddots & 0 \\ 0 & \cdots & 0 & \mathrm{e}^{-\mathrm{i}\frac{\mathbf{k}_{N_g-1}^2}{2}\Delta t} \end{pmatrix} \begin{pmatrix} \tilde{\psi}(\mathbf{k}_0) \\ \tilde{\psi}(\mathbf{k}_1) \\ \vdots \\ \tilde{\psi}(\mathbf{k}_{N_g-1}) \end{pmatrix} \tag{2.40}$$

The spectral and pseudo-spectral basis sets are connected via discrete Fourier transform $\tilde{\psi}(\mathbf{k}_i) = \mathcal{FT}\{\psi(\mathbf{r}_j)\} = \frac{1}{(2\pi)^{3/2}} \sum_j \mathrm{e}^{-\mathrm{i}\mathbf{k}_i\mathbf{r}_j}\psi(\mathbf{r}_j)$ (as discussed above). Since the potential energy operator $\hat{V}$ is diagonal in real space and the kinetic operator $\hat{T}$ is diagonal in $\mathbf{k}$-space, a further diagonalization procedure is not necessary. To save computation time, one has to separate the propagator $\mathrm{e}^{-\mathrm{i}[\hat{V}+\hat{T}]\Delta t}$ into parts that only depend on the kinetic or the potential operators, respectively [119]. One way to split the propagator is to use Trotter's formula [129]. If the operators are time-independent (as assumed within the short time-step Δt), the time-propagator can be written as $\hat{U}(\mathbf{r}, \Delta t) = \mathrm{e}^{\sum_j \Delta t \hat{A}_j}\hat{U}(\mathbf{r}, 0)$, where $\hat{A}_j$ is a finite sequence of operators. The exponential part can be defined by Trotter-Kato formula [117, 130]

$$\mathrm{e}^{\sum_{j=1}^{M} \Delta t \hat{A}_j} = \lim_{N\to\infty} \left(\prod_{j=1}^{M} \mathrm{e}^{\Delta t \hat{A}_j/N} \right)^N . \tag{2.41}$$

If the operators commute, the splitting is exact since the errors originate from the non-commutativity ($[\hat{T}, \hat{V}] \neq 0$) of operators. For a second order splitting with $N = 2$, an error of $\mathcal{O}(\Delta t^2)$ is obtained [131]. A common application of Trotters-Kato's formula is the symmetric split-operator method of third order [132, 133]:

$$\hat{U}(t, t+\Delta t) = \mathrm{e}^{-\mathrm{i}(\hat{T}+\hat{V})\Delta t}\psi(t) = \mathrm{e}^{-\mathrm{i}\hat{V}\frac{\Delta t}{2}}\mathrm{e}^{-\mathrm{i}\hat{T}\Delta t}\mathrm{e}^{-\mathrm{i}\hat{V}\frac{\Delta t}{2}} + \mathcal{O}(\Delta t)^3 \tag{2.42}$$

Here, the third order splitting of the kinetic and potential operator only yields an error of $\mathcal{O}(\Delta t^3)$. Within the time-splitting scheme, one can separately apply the kinetic and potential operator in different bases, i.e, in real and momentum space, respectively. The wavefunction is propagated by one time-step Δt via the following procedure [125]:

$$\psi(\mathbf{r}, t+\Delta t) = \mathrm{e}^{-\mathrm{i}\hat{V}(\mathbf{r})\frac{\Delta t}{2}}\mathcal{FT}^{-1}\{\mathrm{e}^{-\mathrm{i}\hat{T}(\mathbf{k})\Delta t}\mathcal{FT}\{\mathrm{e}^{-\mathrm{i}\hat{V}(\mathbf{r})\frac{\Delta t}{2}}\psi(\mathbf{r}, t)\}\} \tag{2.43}$$

This procedure is repeated N times to evaluate the full time-dependent wavefunction [see Eq. (2.39)]. The split-operator is unitary; the norm is therefore conserved. The error induced by the noncommutability of the kinetic and potential operators affects both, the phase and the norm of the wavefunction. For multichannel problems, in which the wavefunction changes its character during the propagation, off-diagonal elements in the kinetic or potential operator can occur. In these cases, a diagonalization of the non-diagonal matrix is required [125].

2.2.3 Initiation: imaginary time propagation (ITP)

The conventional method for obtaining all eigenfunctions and eigenvalues of a system is to diagonalize a large basis set expansion. However, if only a limited set of eigenfunctions

is required, e.g. the eigenfunctions of the lowest energies, numerical diagonalization is computationally too expensive. In many cases, only the ground-state ψ_0 is needed as initial condition. To this end, the imaginary time-propagation is performed. Within this method, the TDSE is solved in imaginary time ($t = -i\tau$) to obtain the eigenfunction ψ_n with their eigenvalues E_n [134]:

$$|\tilde{\psi}_i(\Delta\tau)\rangle = U_{\mathrm{ITP}}(\Delta\tau)|\psi_i(0)\rangle = \sum_n \mathrm{e}^{-E_n\Delta\tau} \underbrace{\langle\psi_n|\psi_i(0)\rangle}_{c_n} |\psi_n\rangle, \tag{2.44}$$

where $|\psi_i(0)\rangle$ is a trial function (e.g. Gaussian-function) and c_n its projection onto the set of unknown eigenfunctions $\{\psi_n\}$ of the Hamiltonian. For the imaginary time propagation, each eigenfunction ψ_n relaxes at a rate which is proportional to its eigenvalue E_n. Obviously, the eigenstate with the lowest energy (i.e. the ground state ψ_0) relaxes most slowly and persists longer. Since the wavefunction $|\tilde{\psi}_i(\Delta\tau)\rangle$ changes its norm during the imaginary time propagation, renormalization of the wavefunction at each time step $\Delta\tau$ is crucial

$$|\psi_i(\Delta\tau)\rangle = \frac{|\tilde{\psi}_i(\Delta\tau)\rangle}{\sqrt{\langle\tilde{\psi}_i(\Delta\tau)|\tilde{\psi}_i(\Delta\tau)\rangle}}, \tag{2.45}$$

After a time τ, the component of the eigenfunctions ψ_n is reduced relative to the groundstate ψ_0 by a ratio given by: $\mathrm{e}^{-(E_n-E_0)\tau}$. In order to obtain the groundstate, without any disturbing contributions from excited states, the propagation in imaginary time τ has to be sufficiently long so that $c_0 \to 1$. To ensure a certain numerical accuracy of the calculated ψ_0, a convergence criterion is employed, based on the energy of the trial wavefunction $|\psi_i(\Delta\tau)\rangle$. The energy E_0 of the groundstate ψ_0 can be calculated approximately:

$$\begin{aligned} \lim_{\tau\to\infty} \langle\tilde{\psi}_i(\tau+\Delta\tau)|\tilde{\psi}_i(\tau+\Delta\tau)\rangle =& \langle\psi_0|\psi_0\rangle \mathrm{e}^{-2E_0\Delta\tau} \\ \Rightarrow E_0 =& \frac{-1}{2\Delta\tau} \ln\langle\tilde{\psi}_i(\tau+\Delta\tau)|\tilde{\psi}_i(\tau+\Delta\tau)\rangle \end{aligned} \tag{2.46}$$

If the energy difference $\Delta E = |E(\tau) - E(\tau+\Delta\tau)|$ is smaller than a chosen threshold value, here $1 \cdot 10^{-16}$, the converged groundstate is found to be numerically stable during real-time propagation, see Eq. (2.39). In principle, any method propagating a wavepacket can be employed in the ITP (e.g. split operator or Chebyshev method [135]), but it should be compatible with the method used subsequently for real-time propagation.
The first excited state can be obtained by projecting out the ground-state ψ_0 and repeating the ITP scheme for $\psi_1(x, 0)$ (until the iterative alghorithm converges). To obtain the

higher excited state ψ_n, all lower states have to be calculated consecutively and projected out [134]:

$$|\psi_n(0)\rangle = |\psi(0)\rangle - \sum_{m=1}^{n-1} \langle\psi_m|\psi(0)\rangle|\psi_m\rangle. \tag{2.47}$$

2.2.4 Wavefunction splitting method

In strong-field physics, typically electrons will be emitted and acquire high momenta in the continuum. The electronic wavefunction propagates away from the ion, eventually reaching the edge of the numerical spatial grid. Due to the numerical restrictions of the FFTW, the wavefunction gets wrapped around and appears on the other site of the grid, causing unphysical interferences [136]. Thus, the box size $\mathbf{L}$ of the spatial grid has to be large enough to represent the entire wavepacket at all times [125]. However, large box size $\mathbf{L}$ with a good spatial resolution $\Delta\mathbf{x}$ (see Sec. 2.2.1) is computationally expensive, since many grid points are required. In order to minimize the computational costs (box size), the wavefunction splitting method can be applied. Here the wavefunction ψ is divided into two spatially separated parts [137]:

$$\psi(\mathbf{r},t) = \underbrace{c(\mathbf{r})\psi(\mathbf{r},t)}_{\psi_{in}(\mathbf{r},t)} + \underbrace{[1-c(\mathbf{r})]\psi(\mathbf{r},t)}_{\psi_{out}(\mathbf{r},t)} \tag{2.48}$$

The splitting of the wavefunction ψ into an inner ψ_{in} and an outer ψ_{out} part is achieved by the absorber-function $c(\mathbf{r})$

$$c(\mathbf{r}) = c(x,y,z) = [1+\mathrm{e}^{(|x|-x_{max}/1.3)/\beta}]^{-1}[\mathrm{e}^{(|y|-y_{max}/1.3)/\beta}]^{-1}[\mathrm{e}^{(|z|-z_{max}/1.3)/\beta}]^{-1}, \tag{2.49}$$

where $x_{max} = y_{max} = z_{max}$ is the largest absolute value of the spatial grid along each dimension. The smoothing parameter β is chosen in a way that the wavefunction is efficiently absorbed and unphysical interferences are suppressed. Only if the norm $|(\psi_{in}+\psi_{out})|^2 = 1$ stays constant over time, the wavefunction is efficiently absorbed. The advantage of the wavefunction-splitting method is, that in the outer asymptotic region a representation of the wavefunction in coordinate space is not required, since the interaction of the electron with the nuclei can be neglected for large distances. Thus, the Hamiltonian within the velocity gauge $\hat{H} = [\mathbf{p}+\mathbf{A}_{ext}(t)]^2 + V_{nn}$ does not depend on $\mathbf{r}$ anymore [Eq. (2.22)]. The wavefunction $\tilde{\psi}_{out}(\mathbf{p},t)$ in momentum-space representation can be propagated without employing the $\mathcal{FT}$ in each propagation step. In contrast, ψ_{in} has to be propagated with the full Hamiltonian $\hat{H} = [\mathbf{p}+\mathbf{A}_{ext}(t)]^2 + V_{nn} + V_{en}$ since the electron-nuclei interaction V_{en} can not be neglected.

The wavefunction splitting method works well, as long as the momentum of the wavepacket does not exceed $\mathbf{p}_{max} = \mathbf{k}_{max}$, see Eq. (2.33), which is accounted for by the choice of $\Delta\mathbf{x}$. The PEMD $\sigma(\mathbf{p})$ is then calculated via ψ_{out} at time $t \to \infty$ when the electric field is turned off and the interaction with the electric field is over [137, 138]:

$$\sigma(\mathbf{p}) = |\psi_{out}(\mathbf{p}, t \to \infty)|^2. \tag{2.50}$$

2.3 The Keldysh model

2.3.1 Strong-Field Approximation (SFA)

Simple analytical solutions of the TDSE, Eq. (2.14), can only be found by using approximations. The final goal is to substitute the time evolution operator $\mathrm{e}^{-\mathrm{i}\int^t \hat{H}(t')\mathrm{d}t'}$ [Eq. (2.15)] with a number, $\mathrm{e}^{-\mathrm{i}\int^t E(t')\mathrm{d}t'}$, where $E(t)$ is the total instantaneous energy at time t. The exact solution of the TDSE can be rewritten by partitioning the Hamiltonian $\hat{H}(t)$ into a static, field-free part $\hat{H}_0$ and a time-dependent part $\hat{V}_{int}(t)$, describing the interaction with the external electric field [139].

$$|\psi(t)\rangle = -\mathrm{i}\int_0^t \mathrm{d}t'[\mathrm{e}^{-\mathrm{i}\int_{t'}^t \hat{H}\mathrm{d}t''}]\hat{V}_{int}(t')[\mathrm{e}^{-\mathrm{i}\int_0^{t'} \hat{H}_0\mathrm{d}t''}] \times |\psi_i\rangle + \mathrm{e}^{-\mathrm{i}\int_0^t \hat{H}_0\mathrm{d}t''}|\psi_i\rangle. \tag{2.51}$$

Before the laser-field interaction takes place ($t < t'$), the initial bound state $\psi_i = \psi(t = 0)$ evolves in time t with the field free-Hamiltonian $\hat{H}_0$. This evolution is described by the second term of Eq. (2.51). The interaction of the quantum system with the electric field ($t \geq t'$) starts at time t' and is described by the first term of Eq. (2.51) with $\hat{V}_{int}(t) = \mathbf{r}\mathbf{E}_{ext}(t)$ (length gauge). Transition amplitudes $a_{\mathbf{v}}(t)$ at time t can be evaluated by projecting $|\psi(t)\rangle$ onto the exact outgoing continuum state $|\mathbf{v}_e\rangle$ with velocity $\mathbf{v}$:

$$a_{\mathbf{v}}(t) = -\mathrm{i}\int_0^t \mathrm{d}t'\langle\mathbf{v}_e|[\mathrm{e}^{-\mathrm{i}\int_{t'}^t \hat{H}(t'')\mathrm{d}t''}]\hat{V}_{int}(t')[\mathrm{e}^{-\mathrm{i}\int_0^{t'} \hat{H}_0\mathrm{d}t''}]|\psi_i\rangle \tag{2.52}$$

The exact continuum state $|\mathbf{v}_e\rangle$ is typically unknown and becomes a plane wave in the limit $|\mathbf{r}| \to \infty$. The transition amplitude $a_{\mathbf{v}}(t)$, Eq. (2.52), was derived under the assumption that the continuum state is initially unpopulated, i.e. the second term in Eq. (2.51) does not contribute to Eq. (2.52). Within the SFA, the ionization amplitude can be obtained employing the following two main approximations to simplify Eq. (2.52) [139]:

1. The initial state ψ_i of the wavefunction is given by the groundstate ψ_0. From time $t = 0$ to t' the system only accumulates a phase according to the ground-state energy

$\mathrm{e}^{-\mathrm{i}E_i t'} = \mathrm{e}^{\mathrm{i}I_p t'}$, where I_p is the ionization potential. Within this time, excited states are not populated. This approximation is typically valid in the tunnel-regime, where electric fields are strong, and the frequency is low in comparison to the characteristic response frequency of the quantum system. In this regime, the population of excited states is almost negligible.

2. At time t', the system interacts instantaneously with the laser field $\hat{V}_{int}(t')$ and a transition to a final state takes place. In principle, the final state can be any state accessible according to its transition amplitude if total energy conservation is maintained. If only unbound final states are considered, the exact propagator is approximated as:

$$\mathrm{e}^{-\mathrm{i}\int_{t'}^{t}\hat{H}(t'')\mathrm{d}t''} \approx \mathrm{e}^{-\mathrm{i}\int_{t'}^{t}\hat{H}_F(t'')\mathrm{d}t''}. \tag{2.53}$$

Here, the exact Hamiltonian is replaced by $\hat{H}_F \equiv \hat{H} - \hat{V}_c$, in which only the interaction of the electron with the laser field is taken into account, neglecting the Coulomb interaction V_c of the electron with the parent ion. This approximation is only justified if the field interaction energy is much larger than V_c and is therefore known as strong-field approximation (SFA).

The main idea of this approximation is that the propagator of the Coulomb-interaction-free electron is known analytically in form of the Volkov propagator:

$$\langle\mathbf{v}|\mathrm{e}^{-\mathrm{i}\int_{t'}^{t}\hat{H}_F(t'')\mathrm{d}t''} = \mathrm{e}^{-\mathrm{i}\int_{t'}^{t}E(t'')\mathrm{d}t''}\langle\mathbf{v}'| = \mathrm{e}^{-\mathrm{i}\int_{t'}^{t}\frac{1}{2}[\mathbf{v}(t)+\mathbf{A}(t'')-\mathbf{A}(t)]^2\mathrm{d}t''}\langle\mathbf{v}'|. \tag{2.54}$$

In above equation, $|\mathbf{v}'\rangle$ and $|\mathbf{v}\rangle$ correspond to plane waves with kinetic momentum $\mathbf{v}'$ (at time t': moment of ionization: $\mathbf{v}(t') = \mathbf{v}'(t')$) and $\mathbf{v}$ (at time t: moment of observation).

$$|\mathbf{v}'(t')\rangle = |\mathbf{v}(t) - \mathbf{A}(t) + \mathbf{A}(t')\rangle \tag{2.55}$$

After the electron is emitted by the laser-field at time t', it changes velocity according to Eq. (2.55) and propagates in the continuum until a certain time t. The propagation changes the coordinate part of the wavefunction between $|\mathbf{v}'\rangle$ and $|\mathbf{v}\rangle$ in the exact same manner for all coordinates, i.e., temporal phases given by the integral of its instantaneous energy $E(t'')$, Eq. (2.54), were added to the wavefunction in the same way for all coordinates. This is a result of both, the SFA and the dipole approximations, where the Hamiltonian $\hat{H}_F$ and the vector-potential $\mathbf{A}(t)$ are assumed to be coordinate independent. Using both approximation, the SFA allows for an efficient calculation of transition amplitudes:

$$a_v^{SFA}(t) = -\mathrm{i}\int_0^t \mathrm{d}t' \mathrm{e}^{-\mathrm{i}\int_{t'}^{t}\frac{1}{2}[\mathbf{v}(t)+\mathbf{A}(t'')-\mathbf{A}(t)]^2\mathrm{d}t''}\langle \mathbf{v}(t)+\mathbf{A}(t')-\mathbf{A}(t)|\hat{V}_{int}(t')|\psi_0\rangle \mathrm{e}^{\mathrm{i}I_p t'} \quad (2.56)$$

The SFA provides an intuitive picture of ionization as a two step process. The first step at t' is related to ionization (or tunneling), where transition from the ground state to a continuum state (treated as plane wave) takes place. The second step describes the propagation of the electron in the continuum, in which the electron will acquire the final velocity $\mathbf{v}$ at the time of observation t. However, some drawbacks of the SFA originate in the employed approximations [139]:

- The SFA is not gauge invariant. The coordinate part of the plane wave between t and t' transforms differently for velocity ($|\mathbf{p}'\rangle \rightarrow |\mathbf{p}\rangle$, in which $\mathbf{p} = \mathbf{v}(t) - \mathbf{A}(t)$ is defined as the canonical momentum, a conserved quantity, which does not change during propagation) and length gauge ($|\mathbf{v}'\rangle \rightarrow |\mathbf{v}\rangle$, in which $\mathbf{v}$ is related to the kinetic momentum change during propagation). The problem is that the initial state is a bound state ($\mathrm{e}^{\mathrm{i}I_p t'}$), and no gauge-consistent phase of the wavefunction at time t' enters it. As a consequence, the approximate propagation will lead to different results for the two gauges.

- The SFA is not able to describe scattering. During the propagation in the continuum, inelastic scattering of the electron with the parent ion would cause transitions to new excited states $\mathbf{v}''$. Those states are not included in Eq. (2.56).

- The ionization amplitudes are still of approximate nature, since the transition to the continuum at t' is affected by the interaction with the binding potential.

- The SFA neglects the interaction of the unbound photoelectron with the parent ion.

- The SFA only considers transition from the ground state, excited states, which can be populated transiently are not included. One way to include these states is presented in this thesis (see Sec. 3.3).

When it comes to ionization rates, all these shortcomings are only affecting the pre-exponential term in the ionization rate, Eq. (2.56), whereas the fast oscillating exponent remains unaltered. Strong-field phenomena such as ATI-rings can be described well by the SFA. Within the SFA theory, the final momentum $\mathbf{p}_f$ of the photoelectron with zero initial momentum $\mathbf{v}' = 0$ to time t' can be estimated:

$$p_f = |\mathbf{v}(t)\rangle = -\mathbf{A}(t'). \quad (2.57)$$

In order to improve the description of the ionization amplitude a_v^{SFA} of the SFA, one has to replace the Volkov function $\psi_{\mathbf{p}}^{\mathbf{p+A(t)}}(\mathbf{r},t)$ (length gauge) by a more accurate continuum wave function $\psi_{\mathbf{p}}^{(-)}$, which is able to approximately describe both, the laser-field and the Coulomb-field V_c:

$$a_v^{SFA(-)} = -\mathrm{i}\int_{-\infty}^{\infty} \mathrm{d}t \langle \psi_{\mathbf{p}}^{(-)}(t)|\hat{V}_{int}|\psi_i(t)\rangle. \tag{2.58}$$

In the Coulomb-Volkov approximation (CVA), the final distorted (the laser-field distorts the Coulomb-continuum adiabatically) wavefunction $\psi_{\mathbf{p}}^{(-)}$ is approximated by

$$\begin{aligned}\psi_{\mathbf{p}}^{CV(-)}(\mathbf{r},\mathbf{t}) =& D_c(Z_T,\mathbf{k},t)\psi_{\mathbf{p}}^{\mathbf{p+A(t)}}(\mathbf{r},t)\\ =& \underbrace{D_c(Z_T,\mathbf{k},t)\frac{\mathrm{e}^{\mathrm{i}\mathbf{kr}}\mathrm{e}^{-\mathrm{i}\mathbf{p}^2 t}}{(2\pi)^{3/2}}}_{\psi_{\mathbf{p}}^{(-)}} \mathrm{e}^{\mathbf{A}(t)\mathbf{r}-\int_{-\infty}^{t}\mathrm{d}t'\mathbf{p}\mathbf{A}(t')-\frac{1}{2}\int_{-\infty}^{t}\mathrm{d}t'[\mathbf{A}(t')]^2}\\ =& \psi_{\mathbf{p}}^{(-)}\mathrm{e}^{F_D(\mathbf{p},\mathbf{r},t)},\end{aligned} \tag{2.59}$$

where $D_c(Z_T,\mathbf{k},t)$ depends on the charge of the parent ion Z_T, describing the interaction between the photoelectron and the residual ion

$$D_c(Z_T,\mathbf{p},t) = \Gamma\left(1+\frac{\mathrm{i}}{\|\mathbf{p}\|}\right) {}_1F_1\left(-\frac{1}{\|\mathbf{p}\|}, 1-\mathrm{i}\left(\|\mathbf{k}\|\,\|\mathbf{r}\| + \mathbf{kr}\right)\right)\mathrm{e}^{\frac{\pi}{2}}, \tag{2.60}$$

and ${}_1F_1$ denotes the confluent hypergeometric function. The SFA corresponds to the limit $Z_T \to 0$, where the continuum state is described by the Volkov-function. In the other limit, $F_D \to 0$, Eq. (2.59) transforms into the first Born-approximation, which is not an appropriate approximation for molecules, since the scattering (with the scattering wavefunction $\psi_{\mathbf{p}}^{(-)}$) is assumed to occur at one specific center. However, for the H atom, the CVA provides a significant improvement in the description of the photoelectron momentum distributions compared to the SFA, particularly for low energies and $\gamma \geq 1$. Despite its success, the CVA is numerically very challenging and the SFA presents an easier way to analyze the complex pattern of the PEMDs in particular for higher momenta.

2.3.2 The simple man's model (SMM)

Another way to analyze the strong-field dynamics of electrons is to use the SMM (Sec. 1). Here, the ionization dynamics is modeled by means of selected classical trajectories. The ionization process is separated into two steps [10]:

1. First, the electron tunnels through the quasi-static barrier, which is created by the electric field and the potential. Tunneling itself is related to the sub-barrier part of the motion and is reduced to an instantaneous emergence of the electron at the tunnel exit $\mathbf{r}_{out}$ (see Sec. 1).

2. After the electron emerges in the continuum at the position $\mathbf{r}_{out}$, the second step takes place: the classical motion of the electron in the continuum, driven by the laser-field.

The tunnel barrier widths $b_0^M(t)$ can be obtained numerically at every time step t by solving the equation

$$V_c(\mathbf{r}) + \mathbf{r}\mathbf{E}(t) + I_p = 0, \tag{2.61}$$

which is numerically solvable via the Newton-Raphson root-finding algorithm. The width of the tunnel barrier $b_0^M(t)$ can then be defined via the difference between the two roots: $b_0^M(t) = \|\mathbf{r}_{out}(t) - \mathbf{r}_{in}(t)\|$ (see. Fig. 1.2). The numerically obtained width of the tunnel barriers $b_0^M(t)$ can be used to calculate a time-dependent Keldysh parameter $\gamma_t(t)$

$$\gamma_t(t) = \frac{b_0^M(t)\omega}{v_{at}} = \frac{b_0^M(t)}{\sqrt{2I_p}}, \tag{2.62}$$

and eventually the time-dependent ionization rates $w_k(t)$ by using Eq. (1.7) and (1.8). $w_k(t)$ depends on $b_0^M(t)$ and thus, on the molecular structure through the potential $V(\mathbf{r})$, Eq. (2.61).
The second step, the motion of the electron in the continuum is modeled by classical trajectories. Within the SMM, the Coulomb-corrected trajectories can then be found by solving Newton's equation of motion, Eq. (2.7) and Eq. (2.63). Numerically, this is achieved with a Runge-Kutta algorithm of fourth order with adaptive step-size control (Cash–Karp method [140]) and initial conditions according to: $\mathbf{r}_i(t_0) = \mathbf{r}_{out}$ and $\mathbf{v}_i(t_0) = (\mathbf{v}_\perp, \mathbf{v}_\parallel) = (\mathbf{v}_\perp, 0)$, where $\mathbf{v}_\parallel$ and $\mathbf{v}_\perp$ point parallel and perpendicular to the direction of the electric field vector, respectively. Thus the equations of motion are:

$$\begin{aligned} \frac{\partial \mathbf{p}}{\partial t} &= -\nabla(V_c(\mathbf{r}) + \mathbf{r}\mathbf{E}) = [\mathbf{E}(\mathbf{r}_i(t), t) - \nabla V_c(\mathbf{r})] \\ \frac{\partial \mathbf{r}}{\partial t} &= \mathbf{p} \end{aligned} \tag{2.63}$$

Instead of utilizing a single trajectory with a strict localization in phase-space, an ensemble of trajectories with one specific initial coordinate $\mathbf{r}_i(t_0) = r_{out}$ but different velocities $\mathbf{v}_i(t_0) = (\mathbf{v}_\perp, 0)$ is used in order to mimic the distribution of the quantum

mechanical wavefunction. The perpendicular component $\mathbf{v}_\perp$ [69] is not limited to one specific value, since it follows a Gaussian distribution with the maximum located at zero and a standard deviation of $\sigma_\perp = \sqrt{\frac{\omega}{2\gamma}}$. This type of phase-space sampling can be simulated by Gaussian distributed random numbers. The conversion of uniformly distributed random numbers u_1 and u_2 (can be generated by intrinsic subroutines in Fortran) to Gaussian distributed random numbers z_1 with a standard deviation of 1 and an expectation value of zero can be performed by a Box-Muller transformation [141]:

$$z_1 = \sqrt{-2 \ln u_1} \cos 2\pi u_2. \tag{2.64}$$

The advantage of the SMM is the intuitive interpretation of the quantum-mechanically results (i.e. solution of the TDSE) in terms of classical trajectories. The Coulomb force $\nabla V_c(\mathbf{r})$ in Eq. (2.63) can be neglected by assuming $\nabla V_c(\mathbf{r}) = 0$. This allows a comparison between the Coulomb-free and Coulomb-corrected trajectories to study the influence of the long-range interaction between the photoelectron and its parent ion. As already stated in Sec. 1, the SMM represents another powerful method to study strong-field effects if Coulomb-interaction in the continuum and rescattering effects become relevant. Rescattering represents the third step in the ionization mechanism, but is not further pursued in this thesis, since only the interaction with circularly polarized light was investigated. However quantum effects, such as interferences (ATI-rings), cannot be simulated by means of classical trajectories.

Chapter 3

Results

This section presents the results of this thesis in form of the articles published in peer-reviewed international journals.
In the first paper, presented in Sec. 3.1, the interaction of triatmomic modelsystems with few-cycle, circularly polarized infrared laser pulses was investigated by means of fully ab initio quantum dynamical simulations. The complex ionization mechanism of these small model molecules were analyzed by means of electronic density snapshots and PEMDs. The primary focus was on the CDAD (the difference between the PEMDs induced by left- and right-circularly polarized light) and how it will be affected by the CEP of the electric field.
In the second paper (Sec. 3.2), the complex threefold structure observed in these PEMDs of the quantum dynamical simulations were analyzed by means of classical trajectories and the SFA. The origin of the threefold pattern was traced back to three ionization events, which were modeled via three characteristic trajectories. The found trajectories were used to study the long-range Coulomb interaction between the photoelectrons and the parent ion, whereas the contribution of the groundstate on the ionization process was studied via the SFA. In the third paper (Sec. 3.2), the trajectory model and the SFA were extended in order to describe ionization dynamics of triatomic systems with larger internuclear distance. For this kind of systems, the contribution of the excited states differ, and the standard methods described in Sec. 3.2 are no longer suitable. Also the influence of the molecular orientation of the triatomic system on the PEMDs was examined. The focus here was on the CDAD spectra calculated with the molecular averaged PEMDs and how they change for different CEPs of the electric field.
Each section will give a short summary of the results given in their respective articles. The published articles themselves will be presented as facsimiles one after each summary.

3.1 Paper 1: Strong-field ionization of asymmetric triatomic model molecules by few-cycle circularly polarized laser pulses

The paper "Strong-field ionization of asymmetric triatomic model molecules by few-cycle circularly polarized laser pulses" investigates the circular-cichroism in the angular distribution of photoelectron (CDAD) of triatomic model systems and how it is affected by the CEP (carrier envelope phase) of the electric field. The focus is on the interaction of symmetric (all nuclear charges are equal) and asymmetric (all nuclear charges are different) triatomic modelsystems with few-cycle, circularly polarized infrared laser pulses with different CEPs of the electric field. The ionization dynamics and the corresponding CDAD spectra are investigated by fully ab-initio quantum dynamical methods.
While CDAD was observed experimentally for space-fixed NO [104] and CO molecules [103] (see Sec. 1), a detailed theoretical analysis of the ionization dynamics and its effect on the CDAD spectrum is still missing. However, fully numerical treatment is only possible for prototype molecules, such as the molecules, H_2^+ [75] (linear) and H_3^{2+} [112,113] (non-linear). These small molecules build the foundation for the understanding of the more complex physics occurring in multi-electron systems and in polyatomic molecules, respectively.
The investigated triatomic model molecule consists of three space-fixed nuclei with variable charges and one single active electron with two spatial degrees of freedom $\mathbf{r} = (x, y)$ within the plane of the molecule. At time $t = 0$ fs, the electronic density is distributed around the center of charge. Electronic eigenstates were obtained via imaginary time propagation [134]. The electronic wavefunction was obtained by numerically integrating the time-dependent Schrödinger equation (TDSE) on a 2D-grid (x, y) by using the split-operator technique [132] and the FFTW 3 library [142] as outlined in Sec. 2.2. The computed wavefunction was then used to calculate snapshots of the electronic density at specific times and the corresponding photoelectron momentum distribution (PEMDs), which were obtained via the wavefunction-splitting method [137, 138] (see Sec. 2.2.4). The CDAD spectra were defined as the difference of the PEMDs induced by left- and right-circulary (LCP and RCP) polarized electric fields, respectively.
The focus of this work is on the interaction between triatomic model molecules and single-cycle infrared laser pulses. Although such single-cycle laser pulses are still challenging to achieve under lab conditions, the electronic dynamics induced by these pulses can serve as foundation for the analysis of the more complex dynamics induced by longer pulses. Since the symmetric model exhibits a mirror plane along the y-axis, and the LCP and RCP electric field vectors are defined in a way that they have the same symmetry relation

as the model potential, the corresponding time-dependent electronic densities are mirror images of each other, as well, see. Fig. 1 in Paper 1. Depending on the polarization of the electric field, the ionization at a certain time t_n may occur from different nuclei: For example, at a time t_1, ionization can occur from the nucleus $Z_3(Z_1)$ induced by the LCP(RCP) field, whereas at a later time t_2, ionization occurs from the nucleus $Z_1(Z_3)$. After ionization, the electronic density is driven by the electric field either clockwise (LCP) or counterclockwise (RCP) [see Fig. 2 in Paper 1].

The ionization process occurs within two half cycles around the maximum of the laser-pulse at t_0 fs. The simulated PEMDs (see. Fig. 3 in Paper 1) were interpreted employing the standard SFA model to predict final momenta according to Eq. (2.57). For a LCP electric field with a $\phi_{CEP} = 0$, two peaks with different intensities were observed in the PEMDs. The first peak is centered around $(p_x, p_y) \approx (-0.25, 0.25)$ a.u., corresponding to an electronic wavepacket, which is released during the first half-cycle at $t < t_0$, where the vector potential has a positive x ($A_x(t) > 0$) and a negative y ($A_y(t) < 0$) component. The second peak around $(p_x, p_y) \approx (0.25, 0.25)$ a.u. corresponds to an electron-wavepacket, which is released during the second half-cycle at $t > t_0$ (with $A_x(t) < 0$ and $A_y(t) < 0$). The second peak shows a larger intensity due to a increasing population of excited states during the first half-cycle ($t < t_0$), thus leading to more efficient ionization during the second half-cycle ($t > t_0$). For RCP fields, the most intense peak is now centered around $(p_x, p_y) \approx (-0.25, 0.25)$ a.u., since the PEMDs induced by LCP and RCP are mirror images of each other.

By increasing the pulse duration to 10 fs, an ATI ring structure appears in the PEMD. However, the general asymmetry does not change significantly for fields with longer pulse durations.

For a 2 fs pulse, the influence of the CEP on the PEMDs is investigated by varying the CEP of the vector potential, $\phi_{CEP} \in \{ 0, \pi/2, \pi/4, 3\pi/4 \}$. The change in the CEP leads to a counter-clockwise (clockwise) rotation in the PEMDs for the LCP (RCP) field, which, in turn, strongly affects the corresponding asymmetries. The overall structures of the PEMDs induced by electric field with different CEPs resemble each other, when being rotated around the origin of the coordinate system by an angle defined by the CEP. However small changes in the electronic peak-structure due the non-spherical potential cannot be captured by a rotation.

To simulate potentials with different degrees of asymmetry, the nuclear charge Z_3 was increased. To keep the I_p constant, the nuclear charge Z_1 was decreased accordingly. The snapshots of the electronic density at certain times t revealed (see Fig. 2 in Paper 1) that the ionization dynamics for this asymmetric potential changes significantly. The electronic density after photoionization was found to be strongly localized at the deepest well, Z_3.

In general, the evolving electronic wavepacket experiences an overall stronger Coulomb attraction at Z_3, thus leading to a very different ionization dynamics and consequently to a different electron dynamics in the continuum.
Since the asymmetric potential exhibits no mirror symmetry, the symmetry of the evolution of the RCP- and LCP-driven electronic density is also broken. The electron wave-packet experiences a different nuclear-electron interaction during the course of ionization for the differently polarized fields. This leads to pronounced CDAD effects, which are particularly strong for systems with a large degree of asymmetry.
The exact role of excited states and of the long-range Coulomb interactions on the ionization dynamics remains unclear and will be described in detail in the next paper.

Contribution to the appended publication

- Paul, M., Yue, L. and Gräfe, S.
  Strong-field ionization of asymmetric triatomic model molecules by few-cycle circularly polarized laser pulses.
  J. Mod. Opt. **64**, 1104–1111 (2017)

authors:	**Paul, M.**	**Yue, L.**	**Gräfe, S.**
creating the program code	X		
running the simulations	X		
analyzing the results	X	X	X
generating images	X		
writing the manuscript	X	X	X
revision of the manuscript	X	X	X
publication equivalents	**1.0**	-	-

Next, the article 'Strong-field ionization of asymmetric triatomic model molecules by few-cycle circularly polarized laser pulses' will be reprinted [Reprinted from Paul et al. J. Mod. Opt. **64**, 1104–1111 (2017) with permission from Yue, L. and Gräfe, S.].

Journal of Modern Optics

ISSN: 0950-0340 (Print) 1362-3044 (Online) Journal homepage: http://www.tandfonline.com/loi/tmop20

Strong-field ionization of asymmetric triatomic model molecules by few-cycle circularly polarized laser pulses

Matthias Paul, Lun Yue & Stefanie Gräfe

To cite this article: Matthias Paul, Lun Yue & Stefanie Gräfe (2017) Strong-field ionization of asymmetric triatomic model molecules by few-cycle circularly polarized laser pulses, Journal of Modern Optics, 64:10-11, 1104-1111, DOI: 10.1080/09500340.2017.1299883

To link to this article: https://doi.org/10.1080/09500340.2017.1299883

JOURNAL OF MODERN OPTICS, 2017
VOL. 64, NOS. 10–11, 1104–1111
https://doi.org/10.1080/09500340.2017.1299883

Taylor & Francis
Taylor & Francis Group

Strong-field ionization of asymmetric triatomic model molecules by few-cycle circularly polarized laser pulses

Matthias Paul, Lun Yue and Stefanie Gräfe

Institute for Physical Chemistry and Abbe Center of Photonics, Friedrich-Schiller University, Jena, Germany

ABSTRACT

We have developed a numerical model system for a single active electron in an environment of three nuclei with tunable charges arranged as an equilateral triangle. This enables mimicking of both symmetric and asymmetric nuclear charge configurations, while keeping the ionization potential fixed. We investigate the interaction of these model systems with intense, few-cycle, circularly polarized infrared laser pulses and examine the asymmetries between the photoelectron spectra induced by the left- and right-circularly polarized fields. We show that these asymmetries are influenced by the initial symmetry of nuclear charge configurations. We demonstrate that few-cycle laser pulses can induce an additional asymmetry in the photoelectron spectra, which can weaken or enhance the asymmetry imprinted by the initial symmetry properties of the model system.

ARTICLE HISTORY
Received 15 October 2016
Accepted 20 February 2017

KEYWORDS
Ab-initio calculations; strong-field physics; achiral model systems; photoelectron spectra; circular dichroism; few-cycle pulses

1. Introduction

The interaction between light and matter is often dependent on the helicity of the photons. A prominent example is the interaction of light with chiral media, defined as systems that cannot be superimposed on their mirror image. Chirality plays a key role in the functionality of biological, chemical, pharmaceutical and physical systems. The mirror images of chiral molecules, named enantiomers, have identical physical and chemical properties, including melting and boiling points, viscosity and absorption maxima, thus impeding their distinction. However, chiral molecules feature a small difference in the absorption of left- and right-circularly polarized light (circular dichroism, CD) (*1*), enabling their spectroscopic characterization. The difference in absorption, however, is very small, on the order of 10^{-5}, as it is based on the different symmetry properties of the electric and magnetic transition dipole matrix elements.

Another method to spectroscopically characterize chiral systems is photoelectron circular dichroism (PECD), a relatively new method with high sensitivity (*2*, *3*). Typically, the enantiomeric sensitivity is two to three orders of magnitudes higher than that of CD. In PECD, a chiral molecule is ionized by a circularly polarized ultraviolet light field, featuring an asymmetric angular distribution of the photoelectrons. The reason for this enhanced sensitivity is that for the description of PECD only electric dipole transitions are necessary, with the very weak magnetic dipoles being negligible (*4*). Recently, it was demonstrated (*5*) that resonance-enhanced multiphoton ionization may lead to a pronounced asymmetry in the angular distribution of the photoelectrons of chiral molecules. The first experiments on this phenomenon have revealed high enantiomeric sensitivity and asymmetries ranging up to 10%. These pioneering results have triggered broad scientific interest on MP-PECD (*6*–*11*). Theoretical investigations of PECD can for example be found in Refs. (*4*, *6*–*8*, *12*).

Achiral molecules can also exhibit CD, with the sufficient condition being that the experimental system defines three non-coplanar vectors (*13*). Examples include the photoionization of CO molecules adsorbed on a surface with known orientation (*14*–*16*), and molecular-frame photoelectron angular distributions of randomly oriented achiral molecules (*17*–*22*), dubbed circular dichroism in the angular distributions (CDAD). For the latter case, molecular orientations at the time of ionization were determined by coincidence measurement techniques such as cold target recoil ion momentum spectroscopy (*23*). For diatomic molecules, experiments were performed with the propagation direction of the left- and right-circularly polarized (LCP and RCP) light fields perpendicular to the molecular axis (the z-axis), showing strong variations in the CDAD with respect to the photoelectron polar emission angle.

In this work, we present the first results of our *ab initio* simulations of asymmetric model systems irradiated by short, intense LCP and RCP laser pulses. Our

CONTACT Lun Yue lun.yue@uni-jena.de; Stefanie Gräfe s.graefe@uni-jena.de

two-dimensional (2D) model molecule consists of three nuclei with tunable charges and a single electron. We numerically solve the time-dependent Schrödinger equation (TDSE) and calculate the photoelectron momentum distributions (PEMDs). Note that while strong-field ionization by circularly polarized laser fields has been studied extensively, see e.g. (*24*–*30*), the focus of this work is to elucidate the imprint of an asymmetric nuclear environment on the photoelectron momentum distribution. Indeed, for our system, the aforementioned conditions for the detection of CD are fulfilled for the PEMD asymmetries, defined as the normalized difference between the LCP and RCP PEMDs. In particular, the asymmetries in the photoelectron angular distributions are observed. We will show how the asymmetries in the PEMDs depend on the 'degree of asymmetry' of the nuclear charges and the carrier-envelope phase (CEP) of few-cycle laser pulses.

2. Theoretical background

2.1. Model potentials

Our numerical model system constitutes a single-active electron molecule with two spatial degrees of freedom $\vec{r} = (x, y)$ subject to interaction with an intense, circularly polarized, infrared electric field $\vec{E}(t)$. The dynamics of the system follows the TDSE, which reads (atomic units are used unless stated otherwise):

$$\mathrm{i}\frac{\partial}{\partial t}\psi(\vec{r},t) = \left[T + V(\vec{r}) + W(t)\right]\psi(\vec{r},t). \tag{1}$$

In the above equation, $T = -(1/2)(\partial^2/\partial x^2 + \partial^2/\partial y^2)$ is the kinetic energy operator and $W(t)$ is the interaction with the external field in velocity gauge:

$$W(t) = \vec{p}\cdot\vec{A}(t), \tag{2}$$

with $\vec{p} = (p_x, p_y)$ the momentum operator and $\vec{A}(t) = (A_x, A_y)$ the vector potential. In our setup, the vector potential is chosen

$$\begin{aligned} A_x(t) &= \pm\frac{E_0}{\omega}f(t)\sin\left[\omega(t-t_0) - \phi_{CEP}\right] \\ A_y(t) &= -\frac{E_0}{\omega}f(t)\cos\left[\omega(t-t_0) - \phi_{CEP}\right], \end{aligned} \tag{3}$$

with the positive (negative) sign describing RCP (LCP) fields, E_0 the field strength, ω the frequency, ϕ_{CEP} the CEP, and t_0 the maximum of the Gaussian envelope $f(t)$. The model potential $V(\vec{r})$ is described by a screened Coulomb interaction of the electron with three nuclei with charges Z_i fixed at nuclear positions $\vec{R}_i$:

$$\begin{aligned} V(\vec{r}) &= V_n + V_{en}(\vec{r}) \\ V_n &= \sum_{j<i}^{3}\frac{Z_i Z_j}{\left|\vec{R}_i - \vec{R}_j\right|},\ V_{en}(\vec{r}) = -\sum_{i=1}^{3}\frac{Z_i}{\sqrt{\left|\vec{r} - \vec{R}_i\right|^2 + \alpha}} \end{aligned} \tag{4}$$

with the softening parameter $\alpha = 3$. In this work, $\vec{R}_1 = (3, 1.73), \vec{R}_2 = (0, -3.46), \vec{R}_3 = (-3, 1.73)$, such that internuclear distance between two adjacent nuclei is 6 a.u., see middle panel of Figure 1. For all cases considered in this work, the nuclear charges Z_i are chosen such that the ionization potential is $I_P = 6.73$ eV. Note that for the symmetric configuration $Z_1 = Z_2 = Z_3$, the center of mass and charge lies at the origin of the coordinate system, and the system exhibits a mirror plane along the y axis.

The TDSE in Equation (1) is numerically integrated on a grid ranging $[x_{\min}, x_{\max}] \times [y_{\min}, y_{\max}]$, $x_{\max} = y_{\max} = -x_{\min} = -y_{\max} = 220$ with 512 points in each direction using the split-operator technique (*31*) and the FFTW 3 library (*32*). The time step is set to be 0.001 fs. Electronic eigenstates $\varphi_n(\vec{r})$ are obtained via imaginary time propagation (*33*). In all results presented in this work, the initial state is the electronic ground state $\varphi_1(\vec{r})$.

2.2. Photoelectron momentum distributions

In order to obtain the PEMDs, the grid is divided into an inner and outer region. In the inner region, the propagation is performed with the full Hamiltonian, while in the outer, asymptotic region, the interaction of the electron with the nuclei is neglected and the electron dynamics evolve in momentum space, subject to the Hamiltonian $T + W(t) + V_n$. In this way, the wave function is split into an inner part, $\psi_{in}(\vec{r},t) = c(\vec{r})\psi(\vec{r},t)$, and an outer part, $\psi_{out}(\vec{r},t) = [1 - c(\vec{r})]\psi(\vec{r})$, where the mask function is (*34*, *35*)

$$c(\vec{r}) = \left[1 + \mathrm{e}^{(|x| - x_{\max}/1.3)/\beta}\right]^{-1}\left[1 + \mathrm{e}^{(|y| - y_{\max}/1.3)/\beta}\right]^{-1}, \tag{5}$$

with $\beta = 6$ being the smoothing parameter. At each time step, the outer part of the wave function is Fourier-transformed into momentum space and coherently added, resulting at asymptotic times to the total momentum wave function $\psi_{out}(p_x, p_y, t \to \infty)$. The PEMD is then obtained as

$$\sigma(p_x, p_y) = \left|\psi_{out}(p_x, p_y, t \to \infty)\right|^2. \tag{6}$$

The time limit is defined as the time when the norm of the wave function in the inner (or outer) region becomes constant. The asymmetry in the PEMD after interaction with LCP or RCP light is defined by

$$a(p_x, p_y) = \frac{\sigma^{LCP}(p_x, p_y) - \sigma^{RCP}(p_x, p_y)}{\sigma^{LCP}(p_x, p_y) + \sigma^{RCP}(p_x, p_y) + \epsilon}, \quad (7)$$

where the small parameter $\epsilon = 0.5$ is introduced to prevent a zero-valued denominator. Note that we have chosen a relatively high value of ϵ in order to enhance the most prominent features of the asymmetry. The general picture, however, does not change for different values of ϵ.

3. Numerical results

3.1. Symmetric potential

We begin the discussion by presenting results of the time-resolved electron dynamics in a symmetric potential environment ($Z_1 = Z_2 = Z_3 = 0.4$) interacting with a circularly polarized laser field with Gaussian full width at half maximum (FWHM) 1 fs, $t_0 = 5$ fs, wavelength $\lambda = 800$ nm, and intensity 1.4×10^{13} W/cm^2. As the current pulse duration corresponds to a single-cycle pulse, it is still experimentally hard to achieve. The dynamics induced by these pulses are however easier to interpret, and understanding these dynamics can help the interpretation of more complicated processes. Figure 1 presents an overview over the system and the electron dynamics induced by LCP and RCP laser fields.

For the results displayed in Figure 1, the CEP is set to $\phi_{CEP} = 0$, corresponding for LCP (RCP) to a *cosine* ($-$*cosine*) carrier for the x-component of the electric field $E_x(t)$, and a $-$*sine* carrier for the y-component $E_y(t)$. As the Coulombic environment in the model system exhibits a mirror plane (the y-axis), the time-dependent electron densities along the x-axis induced by LCP and RCP, $\varrho(x,t) = \int |\psi(x,y,t)|^2 \mathrm{d}y$, are mirror images of each other, while the densities along the y-axis, $\varrho(y,t) = \int |\psi(x,y,t)|^2 \mathrm{d}x$, are identical. Due to the very short pulse duration, ionization can only occur a half-cycle around $t = 5$ fs where E_x is maximal, as shown in Figure 1. The E_y carrier has a *sine* shape, with two slightly less intense half-cycles of the electric field allowing for ionization. The second half-cycle induces more ionization, as during the previous half-cycle, part of the wave function is being excited to higher lying states, which due to their lower I_P will ionize easier. In the top panels of Figure 2 we show for the LCP pulse the electron density at different times after t_0. Around $t = 5.5$ fs, a electron wave packet leaves the potential between nuclei Z_2 and Z_3, in the third quadrant of the spatial grid. Subsequently, it is driven by the field clockwisely, and leaving the spatial grid with $p_x > 0$ and $p_y > 0$ at later times. For the RCP pulse, the dynamics is mirror-symmetric about the y-axis compared to the LCP case, i.e. the electron wave packet leaves the potential in the second quadrant and is driven counter-clockwisely by the field, leaving the spatial grid with $p_x < 0$ and $p_y > 0$. The mirror symmetry of the density between the LCP and RCP at $t = 5.5$ fs is seen by comparing the lower-left and lower-right panels of Figure 1.

Indeed, these considerations are also reflected in the calculated PEMDs ($\sigma(p_x, p_y)$ for LCP and RCP fields, shown in the upper panels of Figure 3, as well as the integrated spectra

$$\sigma_x(p_x) = \int \sigma(p_x, p_y)\mathrm{d}p_y, \quad \sigma_y(p_y) = \int \sigma(p_x, p_y)\mathrm{d}p_x. \quad (8)$$

The interpretation of these spectra is conveniently done by considering the vector potential. For $\phi_{CEP} = 0$, $A_y(t)$ has a $-$*cosine*-type carrier and is close to unidirectional, pointing into the negative direction, resulting in photoelectrons ending up with positive p_y values, as already seen. The $A_x(t)$ is of $-$*sine* (*sine*) shape for LCP (RCP), resulting in photoelectrons with both positive and negative p_x, seen in the 2D momentum spectra of Figure 3. For LCP, the smaller lobe in the 2D spectrum at $(p_x, p_y) \approx (-0.25, 0.25)$ corresponds to electron wave packets released during the first half-cycle of the $-$*sine* carrier with $A_x(t) > 0$, while the larger lobe at $(p_x, p_y) \approx (0.25, 0.25)$ corresponds to release during the second half-cycle with $A_x(t) < 0$. The difference in magnitude of the two lobes is due to the population of excited states during the first half-cycle which leads to more ionization during second half-cycle. The 2D PEMD for RCP is exactly the mirror symmetric of that for the LCP case with p_y-axis as the symmetry axis.

The mirror symmetry is also reflected in the asymmetry coefficients $a(p_x, p_y)$ of Equation (7), shown in the upper-right panel of Figure 3. As expected, $a_y(p_y)$, the integrated asymmetry over the p_x coordinate vanishes, while $a_x(p_x)$ can reach large values up to 0.3 due to the short pulse employed.

The lower panels of Figure 3 display the PEMDs and the corresponding asymmetries for a 5 fs pulse with $t_0 = 10$ fs. Pronounced above-threshold ionization rings can be seen in the 2D spectra and asymmetry plots while the general features remain very similar. As in the case of the 1 fs pulse, the integrated asymmetries for the longer pulse exhibit no asymmetry along p_y, with asymmetries only present along p_x, where it attains the maximal values of ± 0.3.

3.2. The role of the CEP

Next, we investigate the influence of the CEP on the PEMDs by varying ϕ_{CEP} in the expression of the vector potential in Equation (3), while keeping the pulse FWHM constant to 1 fs. In Figure 4 we present the results for

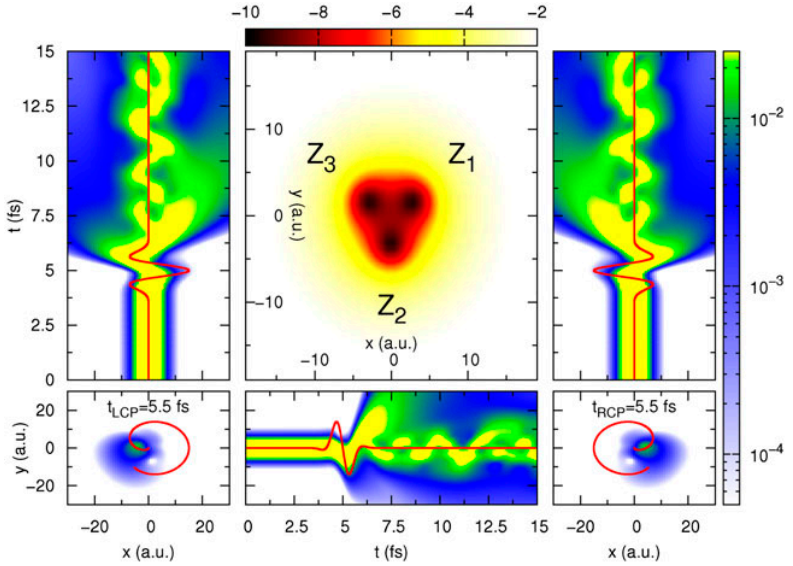

Figure 1. The symmetric model system and the induced dynamics by an intense single-cycle laser pulse with $\lambda = 800$ nm, FWHM $= 1$ fs, and $I = 1.4 \times 10^{13}$ W/cm^2. Shown are the ionic potential (top middle panel); the time-evolution of the integrated electron densities along the x-direction $\rho(x,t)$ (upper left for LCP and upper right for RCP) and the y-direction $\rho(y,t)$ (bottom middle panel for both LCP and RCP); the snapshots of the 2D electron density $|\psi(x,y,t)|^2$ at $t = 5.5$ fs (bottom left for LCP and bottom right for RCP). The red lines in the integrated density plots shows the electric fields E_x and E_y, and the red lines in the 2D density plots show the trace of the electric field for $0 \leq t \leq 5.5$ fs.

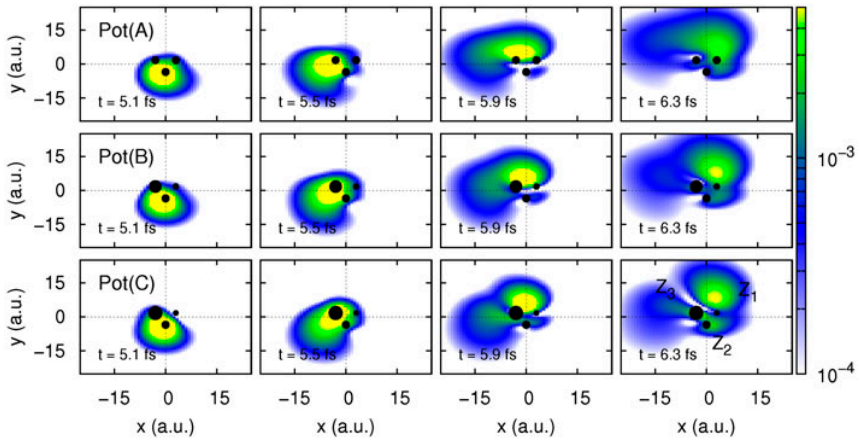

Figure 2. Time-evolution of the electron density induced by the single-cycle pulse (pulse same as in Figure 1) for different model potentials as labelled (see Table 1). The black dots specify the positions of the nuclei, with the magnitude of the dots (not to scale) representing the size of the nuclear charge Z_i.

Table 1. Parameters used for the different model systems (A)–(C).

Model potential	Z_1	Z_2	Z_3	I_P (eV)
A	0.40	0.40	0.40	6.73
B	0.30	0.40	0.49	6.73
C	0.15	0.40	0.59	6.73

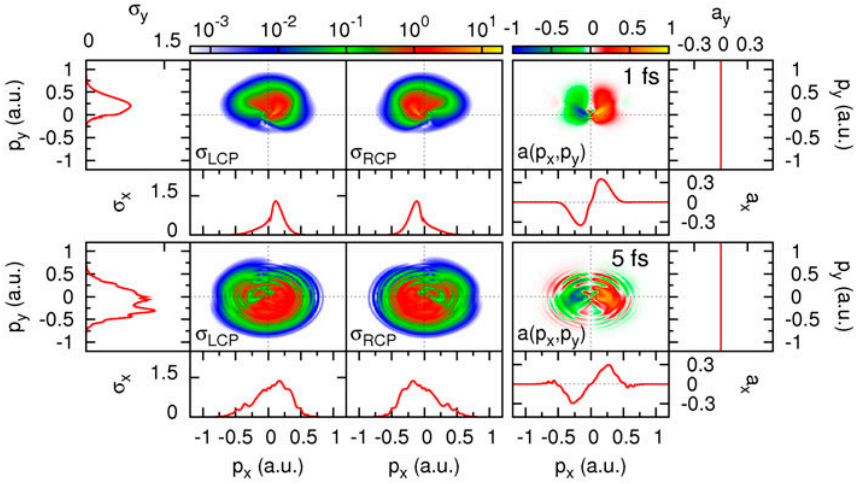

Figure 3. Photoelectron momentum distributions $\sigma(p_x, p_y)$ and the integrated spectra $\sigma(p_x)$ and $\sigma(p_y)$ induced by LCP and RCP fields with $\lambda = 800$ nm, $I = 1.4 \times 10^{13}$ W/cm^2, and two different pulse durations. The corresponding asymmetries of the photoelectron momentum distributions $a(p_x, p_y)$ with integrated asymmetries $a_x(p_x)$ and $a_y(p_y)$ are also shown.

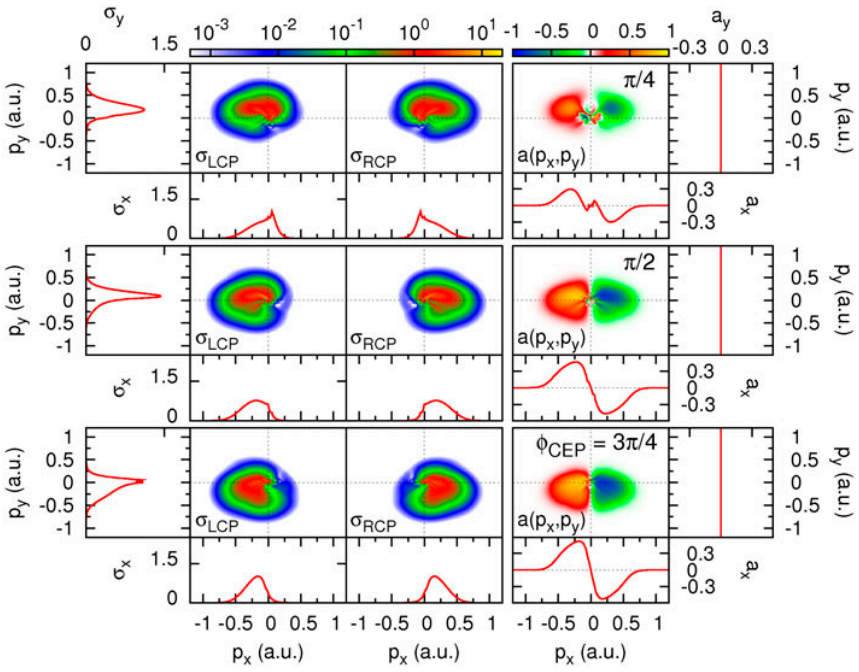

Figure 4. As in Figure 3, now for pulses with parameters $\lambda = 800$ nm, $I = 1.4 \times 10^{13}$ W/cm^2, FWHM = 1 fs, and three different CEPs.

four different CEPs, $\phi_{CEP} = 0, \pi/4, \pi/2, 3\pi/4$. We discuss exemplary the case of $\phi_{CEP} = \pi/2$ in the middle panels of Figure 4, and contrast to the already discussed case of $\phi_{CEP} = 0$ in the upper panel of Figure 3. For $\phi_{CEP} = \pi/2$, $A_x(t)$ has a *cosine* ($-$*cosine*) carrier and $E_x(t)$ a *sine* ($-$*sine*) carrier for LCP (RCP) fields. Since the vector potential is almost unidirectional, pointing into the positive x-direction for the LCP case, photoelectrons will end up with mostly negative p_x values. The situation is reversed for the RCP case, with photoelectrons attaining mostly positive p_x values. The y-component of the vector potential $A_y(t)$ has a $-$*sine* (*sine*) carrier for LCP (RCP), resulting in two lobes in the 2D PEMDs with the dominant one at $p_y > 0$ ($p_y < 0$). Although the dynamics differ strongly as a function of the CEP, the PEMDs are very similar in the sense that two 2D PEMDs can be

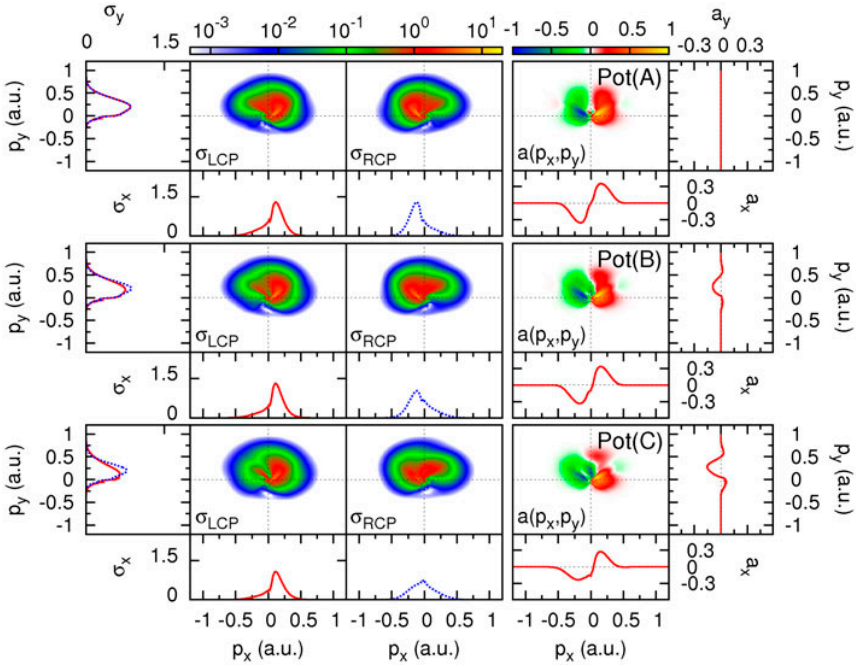

Figure 5. As in Figure 3, now for the three different model systems with parameters given in Table 1. In the integrated spectra, the solid (red) lines are for the LCP fields, while the dashed (blue) lines are for RCP. Pulse parameters are $\lambda = 800$ nm, $I = 1.4 \times 10^{13}$ W/cm^2, FWHM = 1 fs, and $\phi_{CEP} = 0$. Note that the upper panel is identical to the upper panel of Figure 3.

approximately transferred into each other by applying a rotation around the origin by an angle defined by the CEP difference between the two pulses $\Delta\phi_{CEP}$. For atoms this phenomenon is well-described in the literature, see e.g. (36), but in our case the rotated PEMDs are not exactly identical due to the non-spherical potential, a point that we will investigate in the future.

The right panels of Figure 4 display the asymmetries $a(p_x, p_y)$ for the three different CEPs. The overall shape of the asymmetries are clearly seen to change with the CEP: in the 2D asymmetry plots, the distribution is shifted towards negative p_y, as the previously discussed rotation of the PEMD with respect to increasing CEP leads to density at negative p_y values. While the shape and magnitude of the integrated asymmetries $a_x(p_x)$ changes as a function of the CEP, the integrated asymmetry $a_y(p_y)$ remains zero due to the symmetry properties of the pulse.

3.3. Asymmetric potentials

So far, we have considered the symmetric potential environment $Z_1 = Z_2 = Z_3$ containing the y-axis as a mirror plane. As the LCP pulse translates into the RCP pulse by reflection in this mirror plane, the integrated asymmetries a_y were seen to vanish identically. We now turn towards asymmetric potentials. For this purpose, we stepwise increase the degree of asymmetry imprinted by the nuclear environment, while keeping the I_P fixed. Potential (B) represents a model system in which the difference between the charges is relatively small. Model (C), in turn, constitutes a potential where the symmetry is completely broken, with all nuclei having very different charges, see Table 1 for details. For both asymmetric potential models, Z_3 results in the deepest potential well, while Z_1 results in the most shallow one. The deeper the potential well, the more localized is the electron density near it.

Similar to the case of model (A), in models (B) and (C), the LCP pulses liberates the electron at around $t = 5$ fs between nuclei Z_2 and Z_3 (see middle and bottom panels of Figure 2). Now, however, due to Z_3 having a higher charge, the asymmetric nuclear geometry leaves pronounced imprints on the dynamics of the electron wave packet: it is driven by the LCP pulse clockwisely towards Z_3 and experiences a stronger Coulomb attraction (compared to the symmetric model (A)). At the end of the pulse, the electronic density is more compact and more localized near the nuclei compared to model (A), leading to less ionization (see e.g. the integrated spectra in Figure 5).

For the RCP pulses, the photoelectron likewise experiences the asymmetric nuclear geometry. The electron wave packet is liberated and driven counter-clockwisely (not shown), experiencing a different nuclear-electronic

interaction compared to the LCP case. As the electron experiences different nuclear-electronic interaction for LCP and RCP fields, the symmetry properties imprinted by the laser fields on the system are thus broken.

In Figure 5 we show the PEMDs for LCP and RCP fields and their corresponding asymmetries for the three different potential models. As clearly seen, for the models (B) and (C), the integrated spectra σ_y for LCP and RCP are no longer identical, while the σ_x for LCP and RCP are no longer mirror symmetric about the p_y-axis. These observations are also reflected in the integrated asymmetries, with asymmetries in the p_y-direction becoming visible. Along with the increase of a_y from model (A) to model (C) there is also a decrease for a_x.

4. Summary and conclusions

We have presented results from our *ab initio* quantum dynamical calculations based on a 2D, one-electron model system, gaining insight into CDAD of the photoelectrons in asymmetric triatomic systems. To the best of our knowledge, this work represents the first approach towards addressing asymmetries in the photoelectron momentum distribution of asymmetric molecules by purely ab initio quantum dynamical methods. By changing the nuclear charges and thereby modifying the nuclear potential environment, we observe pronounced features in the photoelectron momentum distributions (PEMDs) and their corresponding asymmetries, defined as the normalized difference between the PEMDs induced by left- and right-circularly polarized (LCP and RCP) fields. For a symmetric charge configuration with all nuclei having the same charge, we investigated the carrier-envelope-phase dependence of the PEMDs and their corresponding asymmetries. The CEP leads to a counter-clockwise (clockwise) rotation in the PEMDs for LCP (RCP) pulses, which in turn strongly affects the corresponding asymmetries. For asymmetric charge configurations with the nuclei having different charges, we found that the LCP and RCP PEMDs differ more compared to the symmetric model system where the PEMDs are mirror images of each other.

In the last years, there have been many experiments and theoretical work (see, e.g. Refs. (*26*, *27*, *29*, *30*, *37*, *38*)) examining the strong-field ionization of oriented (and aligned) molecules with circularly polarized laser fields. While our employed model system only considers a single active electron, it is our hope that the ionization results presented here could be of relevance in space-fixed real systems as cited above. In the future, we aim at investigating the influence of the internuclear distance, as both the ionization rate, the electron dynamics following ionization, and the resulting angular distribution of the photoelectrons depend on the internuclear distances, as was shown theoretically in other model systems (*28*, *30*). We also plan to investigate in detail the role of excited electronic states for the observed dynamics and the role of the range of the potential for the photoelectron momentum distributions. This way, we may gain better understanding of the different factors contributing to the multi-photon PECD in asymmetric systems.

Disclosure statement

No potential conflict of interest was reported by the authors.

Funding

The authors highly acknowledge financial support within the priority programme QUTIF (SPP) from the German Science Foundation (DFG) [grant number 4482/3-1].

References

(1) Lowry, T.M. *Optical Rotatory Power*; Dover Publications: New York, 1964.
(2) Powis, I. Photoelectron Circular Dichroism in Chiral Molecules In *Advances in Chemical Physics*, Vol. 138; Rice, S.A., Ed.; John Wiley &; Sons: Hoboken, New Jersey, 2008; 267–329.
(3) Powis, I. Photoelectron Circular Dichroism, In *Comprehensive Chiroptical Spectroscopy*: Berova, N.; Polavarapu, P.L.; Nakanishi, K.; Woody, R.W., Eds.; John Wiley & Sons: Hoboken, New Jersey, 2012, pp. 407–431.
(4) Powis, I. *J. Chem. Phys.* **2000,** *112,* 301–310.
(5) Lux, C.; Wollenhaupt, M.; Bolze, T.; Liang, Q.; Kö, J.; Sarpe, C.; Baumert, T. *Angew. Chem.* **2012,** *124,* 5086–5090.
(6) Lehmann, C.S.; Ram, N.B.; Powis, I.; Janssen, H.M. *J. Chem. Phys.* **2013,** *139,* 234307.
(7) Janssen, M.H.M.; Powis, I. *Phys. Chem. Chem. Phys.* **2014,** *16,* 856–871.
(8) Dreissigacker, I.; Lein, M. *Phys. Rev. A* **2014,** *89,* 053406.
(9) Lux, C.; Wollenhaupt, M.; Sarpe, C.; Baumert, T. *Chem. Phys. Chem.* **2015,** *16,* 115–137.
(10) Garcia, G.A.; Dossmann, H.; Nahon, L.; Daly, S.; Powis, I. *Phys. Chem. Chem. Phys.* **2014,** *16,* 16214–16224.
(11) Fanood, M.M.R.; Powis, I.; Janssen, M.H.M. *J. Phys. Chem. A* **2014,** *118,* 11541-1–11546-2.
(12) Ritchie, B. *Phys. Rev. A* **1976,** *13,* 1411–1415.
(13) Schönhense, G. *Phys. Scr.* **1990,** *1990,* 255–275.
(14) Appling, J.R.; White, M.G.; Orlando, T.M.; Anderson, S.L. *J. Chem. Phys.* **1986,** *85,* 6803–6804.
(15) Westphal, C.; Bansmann, J.; Getzlaff, M.; Schönhense, G. *Phys. Rev. Lett.* **1989,** *63,* 151–154.
(16) Westphal, C.; Kaduwela, A.P.; Fadley, C.S.; Van Hove, M.A. *Phys. Rev. B* **1994,** *50,* 6203–6208.
(17) Reid, K.L.; Leahy, D.J.; Zare, R.N. *Phys. Rev. Lett.* **1992,** *68,* 3527–3530.
(18) Motoki, S.; Adachi, J.; Ito, K.; Ishii, K.; Soejima, K.; Yagishita, A.; Semenov, S.K.; Cherepkov, N.A.; *J. Phys. B* **2002,** *35,* 3801–3819.

(19) Jahnke, T.; Weber, T.; Landers, A.L.; Knapp, A.; Schössler, S.; Nickles, J.; Kammer, S.; Jagutzki, O.; Schmidt, L.; Czasch, A.; Osipov, T.; Arenholz, E.; Young, A.T.; Díez Muiño, R.; Rolles, D.; García de Abajo, F.J.; Fadley, C.S.; Van Hove, M.A.; Semenov, S.K.; Cherepkov, N.A.; Rösch,, J.; Prior, M.H.; Schmidt-Böcking, H.; Cocke, C.L.; Dörner, R. *Phys. Rev. Lett.* **2002,** *88,* 073002.
(20) Geßner, O.; Hikosaka, Y.; Zimmermann, B.; Hempelmann, A.; Lucchese, R.R.; Eland, J.H.D.; Guyon, P.-M.; Becker, U. *Phys. Rev. Lett.* **2002,** *88,* 193002.
(21) Reid, K.L. *Anni. Rev. Phys. Chem.* **2003,** *54,* 397. pMID: 12574491.
(22) Lebech, M.; Houver, J.C.; Dowek, D.; Lucchese, R.R. *Phys. Rev. Lett.* **2006,** *96,* 073001.
(23) Dörner, R.; Mergel, V.; Jagutzki, O.; Spielberger, L.; Ullrich, J.; Moshammer, R.; Schmidt-Böcking, H. *Phys. Rep.* **2000,** *330,* 95–192.
(24) Barth, I.; Smirnova, O. *Phys. Rev. A* **2011,** *84,* 063415.
(25) Kaushal, J.; Smirnova, O. *Phys. Rev. A* **2013,** *88,* 013421.
(26) Holmegaard, L.; Hansen, J.L.; Kalhoj, L.; Louise Kragh, S.; Stapelfeldt, H.; Filsinger, F.; Kupper, J.; Meijer, G.; Dimitrovski, D.; Abu-samha, M.; Martiny, C.P.J.; Madsen, L.B. *Nat. Phys.* **2010,** *6,* 428–432.
(27) Dimitrovski, D.; Abu-samha, M.; Madsen, L.B.; Filsinger, F.; Meijer, G.; Küpper, J.; Holmegaard, L.; Kalhøj, L.; Nielsen, J.H.; Stapelfeldt, H. *Phys. Rev. A* **2011,** *83,* 023405.
(28) Yuan, K.-J.; Bandrauk, A.D. *Phys. Rev. A* **2011,** *84,* 013426.
(29) Spanner, M.; Gräfe, S.; Chelkowski, S.; Pavicic, D.; Meckel, M.; Zeidler, D.; Bardon, A.B.; Ulrich, B.; Bandrauk, A.D.; Villeneuve, D.M.; Dörner, R.; Corkum, P.B.; Staudte, A. *J. Phys. B* **2012,** *45,* 194011.
(30) Doblhoff-Dier, K.; Dimitriou, K.I.; Staudte, A.; Gräfe, S. *Phys. Rev. A* **2013,** *88,* 033411.
(31) Feit, M.D.; Fleck, J.A.; Steiger, A. *J. Comput. Phys.* **1982,** *47,* 412–433.
(32) Frigo, S.G.J.M. *ICASSP Conf. Proc.* **1998,** *3,* 1381–1384.
(33) Kosloff, R.; Tal-Ezer, H. *Chem. Phys. Lett.* **1986,** *127,* 223–230.
(34) Heather, R.; Metiu, H. *J. Chem. Phys.* **1987,** *86,* 5009–5017.
(35) Keller, A. *Phys. Rev. A* **1995,** *52,* 1450–1457.
(36) Martiny, C.P.J.; Madsen, L.B. *Phys. Rev. Lett.* **2006,** *97,* 093001.
(37) Hansen, J.L.; Holmegaard, L.; Kalhøj, L.; Kragh, S.L.; Stapelfeldt, H.; Filsinger, F.; Meijer, G.; Küpper, J.; Dimitrovski, D.; Abu-samha, M.; Martiny, C.P.J.; Madsen, L.B. *Phys. Rev. A* **2011,** *83,* 023406.
(38) Yuan, K.J.; Bandrauk, A.D. *Phys. Rev. A* **2011,** *84,* 013426.

3.2 Paper 2: Imprints of the Molecular Electronic Structure in the Photoelectron Spectra of Strong-Field Ionized Asymmetric Triatomic Model Molecules

The paper "Imprints of the Molecular Electronic Structure in the Photoelectron Spectra of Strong-Field Ionized Asymmetric Triatomic Model Molecules" investigates the complex structure in the PEMDs of triatomic model systems. The strong field-driven electron dynamics and the corresponding PEMDs were calculated by fully ab initio quantum dynamical methods and analyzed by means of classical trajectories within the SMM and numerical solutions of the SFA. The primary focus is set on the analysis of the threefold pattern observed in these PEMDs and how such structures relate to the triatmomic molecular potential.

From a computational point of view, the full treatment of the interaction of intense laser fields with polyatomic molecules is not feasible, as too many degrees of freedom on different time scales are involved. Even for the simple molecules, such as H_2 [78], H_2^+ [75], and H_3^{2+} [112, 113], the physics of the ionization dynamics becomes significantly more complicated than for atoms. Yet, these kind of molecules can be regarded as prototype systems since observed physical effects also occur in larger molecules. Therefore, this paper is focused on the simplest, non-colinear molecule, H_3^{2+}.

The triatomic model system consists of three space-fixed nuclei (frozen core approximation) and a single active electron with two degrees of freedom x, y. The electronic density is distributed around the origin of the coordinate system at the center of mass and charge. The charges of the three nuclei are varied to investigate symmetric and asymmetric configurations, while the ionization potential I_p is kept constant. As before, the symmetric system exhibits a mirror symmetry along the y-axis. By decreasing the range of the potential, the number of excited states and the long-range Coulomb-interaction in the continuum can be systematically reduced. For various types of triatomic model systems (see Tab. 1 of paper 2), the TDSE was numerically integrated on a 2D-grid using the split-operator technique [132] and the FFTW3 library [142] as outlined in Sec. 2.2. The obtained electronic wavefunction was used to calculate snapshots of the electronic density at specific times and to simulate the corresponding PEMDs by applying the wavefunction splitting method [137, 138] (see Sec. 2.2.4). To obtain the PEMDs within the SFA formalism, the time integrals in Eq. (2.56) were numerically calculated, while the groundstate was obtained via imaginary time propagation [134] (ITP). The classical trajectories were calculated by solving the classical Newton's equation of motion (Eq. 2.7)

employing a Runge-Kutta algorithm of fourth order (Cash–Karp method [140]) and initial conditions according to the SMM (see Sec. 2.3.2). The ionization rate and the initial conditions in space were numerically calculated via Eqs. (2.62) and (2.61), while the initial momentum $p = (p_\perp, p_\parallel = 0)$ was simulated via Gaussian-distributed random numbers (see Sec. 2.3.2). In the multiphoton regime ($\lambda = 800$ nm), the center of the Gaussian momentum distribution at $\mathbf{p} = (0 \pm \mathbf{p}_0, 0)$ was additionally shifted by $\mathbf{p}_0 = 0.22$, with the plus sign for LCP, and the minus sign for the RCP pulse, corresponding to the excess energy the electron will acquire in the above-threshold ionization case.

The influence of the long-range Coulomb interaction and the excited states on the structure of the PEMDs was studied by comparing PEMDs of various kinds of symmetric model systems with different potential ranges (see Tab. 1 in Paper 2). All of the PEMDs, obtained by fully ab initio quantum-dynamical calculations, showed the same threefold symmetric structure with the expected ATI-rings, in which the intensities and the positions of these three peaks differ for different model potentials: in comparison to the short-range systems, the PEMD of the Coulomb-like system shows a very different intensity profile, in which the threefold peak structure is shifted clockwise (see Fig. 2 in Paper 2). Since the number of excited states is reduced and multiphoton ionization from higher-lying excited states is not possible within short-range systems, the total ionization yield is significantly decreased for these kind of potentials. The finger-like structure (see panel (A) in Fig. 2 in Paper 2), which is a result of multiphoton ionization, was therefore only observed in the PEMDs (located at small momenta) of the Coulomb-type system.

The origin of the threefold structure was identified by means of classical trajectories. To this end, the evolution of the electronic density in the continuum was presented in form of snapshots of the electronic density at certain times t. The threefold structure in the electronic density, which has built up during the course of ionization, could be analyzed by three characteristic trajectories (see Fig. 1 in Paper 2). These trajectories start at different times t_n and tunnel exits, near the three nuclei Z_1, Z_2, and Z_3. The final momenta of these three selected trajectories could be assigned to the three peaks in the PEMD. Eventually, the relation between the molecular potential with the three nuclei Z_1, Z_2, and Z_3 and the threefold structure observed in the PEMDs was revealed by these three classical trajectories. The spectra calculated with the full CTMC method and the SFA were in good agreement with the results obtained from direct TDSE simulations, but only for short-range systems where the major part of ionization originates from the groundstate. Nevertheless, the Coulomb-corrected trajectories were able to reproduce the clockwise rotation observed in the PEMDs of the Coulomb-like potential.

For asymmetric potentials, where all charges differ and no mirror symmetry is present, the PEMDs induced by LCP and RCP electric fields are no longer mirror images of each other.

The higher the degree of asymmetry in the molecular potential (difference of the three nuclear charges), the larger the differences between both LCP and RCP spectra (CDAD). Due to the large changes in the electronic structure, the three-fold shape vanishes and the resulting CDAD increases. These asymmetric changes in the PEMDs were analyzed by means of classical trajectories as well, but only for short-range-systems. Tunnelexits and ionization probabilities, Eq. (2.62), were recalculated by including the Stark-shift $\boldsymbol{\mu}\mathbf{E}$ in Eq. (2.61), where $\boldsymbol{\mu}$ is defined as the permanent dipole moment of the groundstate ($\boldsymbol{\mu} = -\langle\psi_0|\mathbf{r}|\psi_0\rangle$). Here, the intensities of the ionization probability maxima $w_k(t_{max})$ and the time t_{max} of their appearance are changed significantly when the Stark shift is included in the simulation. The spectra, calculated with the full classical trajectory Monte-Carlo (CTMC) method on the basis of the recalculated ionization probability $w_k(t_{max})$ (Fig. 4 in Paper 2), were in good agreement with the results of the TDSE simulations (Fig. 3 in Paper 2), while the peaks in the spectra show the same clockwise and counterclockwise shifts for both methods.

As this is a paper in a Letter format, many facets have not been discussed in detail, such as excited-states and the dependence of the internuclear distance and the molecular orientation on the ionization mechanism. A more detailed analysis of the tri-atomic model system is part of the next paper.

Contribution to the appended publication

- Paul, M., Yue, L. and Gräfe, S.
  Imprints of the molecular electronic structure in the photoelectron spectra of strong-field ionized asymmetric triatomic model molecules.
  Phys. Rev. Lett. **120**, 233202 (2018)

authors:	**Paul, M.**	**Yue, L.**	**Gräfe, S.**
creating the program code	X		
running the simulations	X		
analyzing the results	X	X	X
generating images	X		
writing the manuscript	X		X
revision of the manuscript	X	X	X
publication equivalents	**1.0**	-	-

Next, the article 'Imprints of the molecular electronic structure in the photoelectron spectra of strong-field ionized asymmetric triatomic model molecules' will be reprinted. [Reprinted from Paul et al. Phys. Rev. Lett. **120**, 233202 (2018) with permission from Yue, L. and Gräfe, S.; Copyright 2018 American Physical Society.].

Imprints of the Molecular Electronic Structure in the Photoelectron Spectra of Strong-Field Ionized Asymmetric Triatomic Model Molecules

Matthias Paul, Lun Yue, and Stefanie Gräfe*
Institute for Physical Chemistry and Abbe Center for Photonics, Friedrich-Schiller Universität Jena, Helmholtzweg 4, 07743 Jena, Germany

(Received 6 December 2017; published 8 June 2018)

We examine the circular dichroism in the angular distribution of photoelectrons of triatomic model systems ionized by strong-field ionization. Following our recent work on this effect [Paul, Yue, and Gräfe, J. Mod. Opt. **64**, 1104 (2017)], we demonstrate how the symmetry and electronic structure of the system is imprinted into the photoelectron momentum distribution. We use classical trajectories to reveal the origin of the threefolded pattern in the photoelectron momentum distribution, and show how an asymmetric nuclear configuration of the triatomic system effects the photoelectron spectra.

DOI: 10.1103/PhysRevLett.120.233202

Angle-resolved photoelectron spectroscopy has been very successful in probing photoionization and intramolecular dynamics of molecules [1]. The photoelectron angular distributions depend on the symmetry and vibrational dynamics of the probed system, the molecular orbital from which the electron is emitted, the experimental geometry, and the wavelength of the interacting laser pulse. The scattering of the emitted photoelectron off the molecular potential yields the molecular-frame photoelectron angular distribution, which provides rich structure and can be strongly anisotropic. The relative orientation of the molecule to the laser polarization axis or plane strongly determines the shape of the photoelectron angular distributions. Photoelectron angular distributions have been recorded for atoms and molecules interacting with weak [2–4] or intense fields [5–9].

While in the last decades strong-field physics has mainly focused on atoms and small diatomic molecules, also larger and chemically more interesting molecules have moved into the center of research. Many experiments have investigated ionization and fragmentation dynamics of smaller polyatomic molecules in strong laser fields [10–14]. From the theoretical side, it is clear that it is impossible to treat the interaction of polyatomic molecules with intense laser fields fully numerically, as too many degrees of freedom on many different time scales are involved. In addition, in larger systems, many different phenomena such as multielectron or scattering effects may occur. Consequently, the simplest molecules H_2 and H_2^+ have been in the center of theoretical and numerical research [15–21]. They can be regarded as prototype systems, as many effects first detected there have been observed later in larger molecules as well. The molecules H_3^{2+} and H_3^+, the simplest polyatomic molecules, have attracted considerable theoretical interest [22–25]. While also larger nonlinear molecules have been theoretically examined [26–29], most of the work utilized approximations or assumptions to describe the strong-field interaction. On the other hand, a lot of the understanding of strong-field phenomena is based on the strong-field approximation (SFA) [30–32], providing analytical expressions for ionization and photoelectron momentum distributions. In the SFA, it is assumed that the laser field is so strong that after (strong-field) ionization, the electron is solely driven by the laser field and the parent ion represents a small perturbation, which can be neglected. Several attempts have been made to adapt the SFA to molecules to address the additional complications or challenges introduced by the multiatomic center nature of molecules [33–36].

For chiral molecules being ionized by circularly polarized laser pulses, circular dichroism in the photoelectron angular distribution can be observed, with circular dichroism referring to a difference in the interaction of a sample with left- and right-circularly polarized light. However, it has been theoretically predicted [37,38] and later experimentally verified [39,40] that circular dichroism in the photoelectron angular distribution occurs with the sufficient condition of nonplanarity of three vectors defining the experimental system: the propagation axis of the circularly polarized light, the photoelectron momentum, and the molecular axis. Thus, achiral, oriented diatomic molecules can feature circular dichroism in the photoelectron angular distribution. Experimental examples include valence and inner shell photoionization of adsorbed CO molecules [39,40], aligned NO molecules [41–43], and the case of resonant dissociative photoionization of autoionizing H_2 [44].

In this Letter, we extend the investigation towards nonsymmetric, noncolinear molecular systems interacting with intense laser fields. We demonstrate for the first time, to the best of our knowledge, using fully *ab initio* quantum dynamical simulations, how the electronic structure and symmetry of nonlinear triatomic molecules are imprinted

into the photoelectron momentum distribution following strong-field ionization. We are, in particular, interested to analyze which properties of the electronic structure are imprinted into the strong-field photoelectron momentum distribution. For this, we employ our recently developed triatomic model system [45] consisting of a single active electron with two spatial degrees of freedom $\boldsymbol{r} = (x, y)$ interacting with intense, circularly polarized, near- and midinfrared electric fields $\boldsymbol{E}(t)$. The beauty of this model system is that by fine-tuning the charges of the nuclei, we control the symmetry (or its absence). Additionally, we control the range of the potential environment and can investigate which influence the Coulomb potential imprints onto the photoelectron momentum distributions. We analyze the strong-field electron dynamics and the photoelectron momentum distributions by combining different methods, by application of the numerical solution of the time-dependent Schrödinger equation (TDSE), as well as the classical trajectory Monte Carlo (CTMC) and SFA calculations. This enables us to relate the molecular electronic structure to strong-field photoelectron momentum distributions.

The dynamics of the system is governed by the TDSE which reads (atomic units are used unless stated otherwise)

$$\mathrm{i}\frac{\partial}{\partial t}\psi(\boldsymbol{r},t) = \left[-\frac{1}{2}\nabla^2 + V(\boldsymbol{r}) + \boldsymbol{p}\cdot\boldsymbol{A}(t)\right]\psi(\boldsymbol{r},t). \quad (1)$$

In the above equation, the interaction with the external field is given in velocity gauge, with $\boldsymbol{p} = (p_x, p_y)$ the momentum operator and $\boldsymbol{A}(t) = [A_x(t), A_y(t)]$ the vector potential, defined as

$$A_x(t) = \pm\frac{E_0}{\omega} f(t)\sin[\omega(t-t_0) - \phi_{\mathrm{CEP}}],$$
$$A_y(t) = -\frac{E_0}{\omega} f(t)\cos[\omega(t-t_0) - \phi_{\mathrm{CEP}}]. \quad (2)$$

The positive (negative) sign describes right- (left-) circularly polarized (RCP and LCP) fields, E_0 is the field strength, ω the laser frequency, $\phi_{\mathrm{CEP}} = 0$ the carrier-envelope phase, and $t_0 = 0$ fs the time when the Gaussian envelope $f(t)$ is maximum. The model potential $V(\boldsymbol{r}) = V_{nn} + V_{en}(\boldsymbol{r})$ describes bare Coulomb repulsion between the three nuclei V_{nn} with charges Z_i fixed at nuclear positions $\boldsymbol{R}_i$, as well as the interaction of the electron with three nuclei, $V_{en}(\boldsymbol{r})$; see Fig. 1 (a1) and (b1) and the Supplemental Material [46] for details. The positions of the nuclei are set to form an equilateral triangle with internuclear distances between two adjacent nuclei of $R = 3.5$ a.u. The central question of our investigation is to analyze the structure in the photoelectron momentum distributions and how it can be related to the molecular potential. We aim at distinguishing Coulomb effects as originating from excited electronic states and those acting on the continuum electron (long-range contributions).

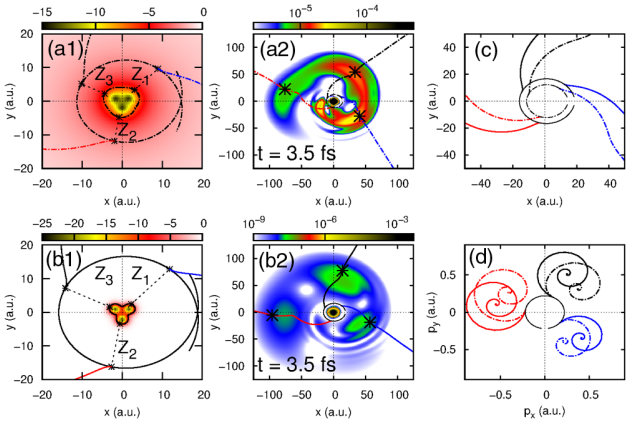

FIG. 1. Comparison of long- and short-range model systems: (a1) Coulombic and (b1) short-range potential (color scale in eV), shifted down to 0. The "circle" around the potential indicates the classical tunnel exits. (a2/b2) Snapshots of the electron density $|\psi(x, y, t_{fix})|^2$ in long-range (a2) and short-range (b2) potentials. The stars indicate the current position of the electron moving along the trajectory. (c),(d) Three selected classical trajectories in coordinate (c) and momentum space (d). The solid lines represent trajectories in the short-range potential, while the dashed lines are trajectories in the Coulomb potential.

We therefore employ potentials of different range to describe the nuclear-electron attraction,

$$V_{en}(\boldsymbol{r}) = -\sum_{i=1}^{3}\frac{Z_i \exp\left(-\beta|\boldsymbol{r}-\boldsymbol{R}_i|^2\right)}{\sqrt{|\boldsymbol{r}-\boldsymbol{R}_i|^2 + \alpha}}, \quad (3)$$

with the softening parameter $\alpha = 1$. The parameter β defines the range of the potential, for $\beta = 0$, the potential is Coulombic. For all cases considered in this work, the nuclear charges Z_i and the short-range parameters β are chosen such that the ionization potential is the same, $I_P = 8.64$ eV (with the specific values being listed in the Supplemental Material [46]). Note that the system is designed such that for the symmetric configuration $Z_1 = Z_2 = Z_3$, the center of mass and charge lies at the origin of the coordinate system, and the system exhibits a mirror symmetry along the y axis.

We numerically integrate the TDSE in Eq. (1) on a 512×512 grid using the split-operator technique [47] and the FFTW 3 library [48]; for details, please refer to Ref. [45] and the Supplemental Material [46]. The photoelectron spectra are obtained by the wave function splitting methods [49,50]. Electronic eigenstates $\varphi_n(\boldsymbol{r})$ are obtained via imaginary time propagation [51]. In all results presented in this work, the initial state is the electronic ground state $\varphi_1(\boldsymbol{r})$.

We compare the results of our *ab inito* quantum dynamics with results obtained by CTMC calculations and the SFA, where after ionization the electron is subjected to the laser field only, completely neglecting the molecular potential. The photoelectron momentum

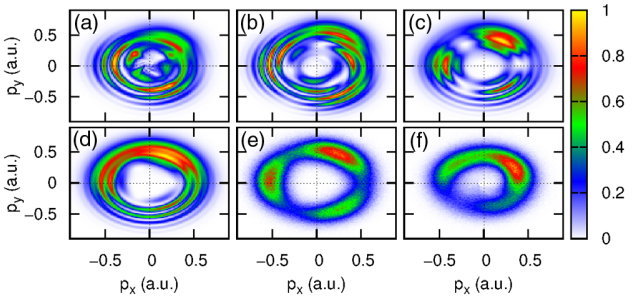

FIG. 2. Photoelectron momentum distributions of the symmetric model system induced by an intense few-cycle LCP laser pulse with $\lambda = 800$ nm, Gaussian full width at half maximum $= 5$ fs, and $E_0 = 0.02$ a.u.. (a) Coulombic potential, (b),(c) short-range potentials ($\beta = 0.005$ and $\beta = 0.3$), (d) short-range SFA, and (e) short-range ($\beta = 0.3$), and (f) long-range CTMC calculations.

distributions $\sigma(\boldsymbol{p})$ are calculated as detailed in the Supplemental Material [46], which contains Refs. [52–54].

We start by investigating the photoelectron momentum distribution of a symmetric model system V_{sym}. Starting from the electronic ground state $\varphi_1(\boldsymbol{r})$, the system interacts with a LCP 800 nm laser pulse with field strength $E_0 = 0.02$ a.u. and a Gaussian full width at half maximum of 5 fs. This rather intense pulse ionizes the system [17% of the norm of $\psi(\boldsymbol{r}, t)$ leaving the grid], yielding a photoelectron momentum distribution (rescaled to the maximal value) as shown in Fig. 2(a).

It can be seen that the photoelectron momentum distribution originating from the Coulombic system [panel (a)] features the expected above-threshold ionization (ATI) ring structure, together with some groups of prominent signal peaks near $\boldsymbol{p} = (-0.4, 0), \boldsymbol{p} = (0.2, -0.4)$, and some weaker peaks near $\boldsymbol{p} = (0.2, 0.4)$, forming a threefold symmetric structure. Our aim is to assign the observed features of the photoelectron momentum distributions to the structure of the molecular potential and distinguish which features result from contributions of intermediate states and which part can be assigned to the Coulomb character of the continuum. We therefore repeat the calculations with short-range potentials, see Figs. 2(b) and (c). The first prominent difference is that the total ionization yield is reduced substantially (not shown in the figure), the shorter the range of the potential. As in short-range potentials the number of excited states is finite, in contrast to Coulomb-type potentials, and in the limit of true δ potentials reduced to only one single bound state, the multiphoton mechanism of ionization is substantially reduced and ionization proceeds predominantly via tunneling [55,56]. The second difference can be seen at very small momenta: while the Coulombic case shows some fingerlike structure which can be assigned to excited states and multiphoton ionization, these structures are absent for the short-range potentials. The third and most prominent difference of the photoelectron momentum distributions from short-range potentials is that the threefold symmetric peak structure is much more pronounced compared to the Coulombic case. Also shown in Fig. 2 are the results of an SFA calculation, panel (d), and CTMC calculations (see Supplemental Material [46]), panel (e), featuring likewise the threefold symmetric structure.

What is the origin of this threefold structure in the photoelectron momentum distributions? Snapshots of the electronic density (Fig. 2, Supplemental Material [46]) during laser interaction clearly show how the threefold structure is built up during the course of ionization. The origin of the threefold structure during the ionization can be assigned to three different ionization events, reflected by three typical trajectories, see Figs. 1(c) and (d) (solid lines). These trajectories depicted here start with an initial transversal momentum (see Supplemental Material [46]) at tunnel exits located near the nuclei's positions and end up at momenta corresponding to the ones of the short-range quantum dynamical momentum distribution (and also the SFA). We also display the corresponding trajectories for long-range potentials Figs. 1(c) and (d) (dashed lines). It can be clearly seen that the Coulomb continuum causes a pronounced shift to the trajectories, which is, not surprisingly, the strongest at early times, when the electron is close to the nuclear positions. Also, as indicated in Fig. 1, the tunnel exits for the Coulomb potential lie closer to the nucleus than for short-range potentials. Thus, the classical picture suggests that the main influence of the Coulomb continuum is a rotation of the photoelectron momentum distribution. The rotation can also be seen when comparing Figs. 2(a)–(c) and is most pronounced for small momenta (inner ATI rings). This is, however, not all of the differences we can gather if we reconsider Fig. 2(a), as an inner fingerlike structure can be seen. This suggests that the influence of excited states seems to be of importance for the dynamics, as to be expected for strong-field processes with dominant multiphoton character. Still, in order to relate the electronic structure to the photoelectron momentum distributions, in the following discussion, we will thereby focus primarily on short-range potentials, where the influence of excited states is substantially reduced and the overall structure is more pronounced.

We now consider asymmetric potentials. Figure 3 displays the corresponding photoelectron momentum distributions for asymmetric short-range potentials for LCP and RCP pulses. While for the symmetric potential, the change of the polarization direction from LCP to RCP corresponds merely to a mirror image of the photoelectron momentum distribution (reflected on the p_y axis), this is not the case for the asymmetric potentials: these photoelectron momentum distributions differ substantially, as the mirror symmetry in the system is absent. The higher the degree of asymmetry imprinted by the nuclear potential, the less visible becomes the threefold symmetric structure of the photoelectron momentum distributions. At the same time, the intensity pattern of the photoelectron

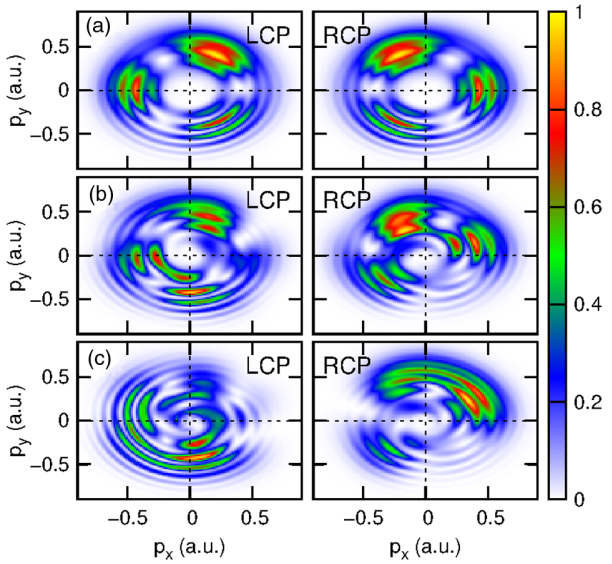

FIG. 3. Photoelectron momentum distributions for LCP (left) and RCP (right) fields for short-range asymmetric potentials. (a) Symmetric case, for comparison. The degree of asymmetry, thus the differences in the charges Z_i of the nuclei, increases from the middle (b) to the lower panels (c). For the corresponding results of the SFA; see Fig. 1, Supplemental Material [46].

momentum distributions differ for these few-cycle pulses: while for the LCP pulses, the intense peaks in the photoelectron momentum distributions are located at negative p_y values [$\boldsymbol{p} = (0.1, -0.4)$, third quadrant], the intense peaks for RCP pulses can be seen at positive p_y values [$\boldsymbol{p} = (0.4, 0.2)$, first quadrant], thus causing a strong circular dichroism in the angular distribution.

The reason for this can be understood when considering the classical trajectory picture, see Fig. 4 for LCP and RCP pulses: For LCP, the ionization rate around Z_1 and Z_2 is similar as in the symmetric case, while the ionization rate at times when the electric field vector points in the opposite direction of Z_3 is strongly suppressed. For RCP pulses, ionization around Z_3 behaves similar to the symmetric case, but ionization at times when the electric field vector points in the opposite direction of Z_1 and Z_2 is strongly enhanced; see also Fig. 2 of the Supplemental Material [46]. This results in a strong difference in the intensity pattern. The second difference can be attributed to a difference in ionization times: taking a closer look at the ionization times, we gather that for LCP pulses, ionization around Z_2 happens slightly earlier in asymmetric potentials, while ionization around Z_1 and Z_3 occurs later, leading to a clock- and anticlockwise shift in the photoelectron momentum distributions. For the RCP pulses, the situation differs: ionization around Z_2 happens later for asymmetric potentials, while ionization around Z_1 is almost the same as for symmetric potentials, resulting in an anticlockwise shift in the photoelectron momentum distributions.

To summarize, we have presented results from our *ab initio* quantum dynamical calculations in a two-dimensional,

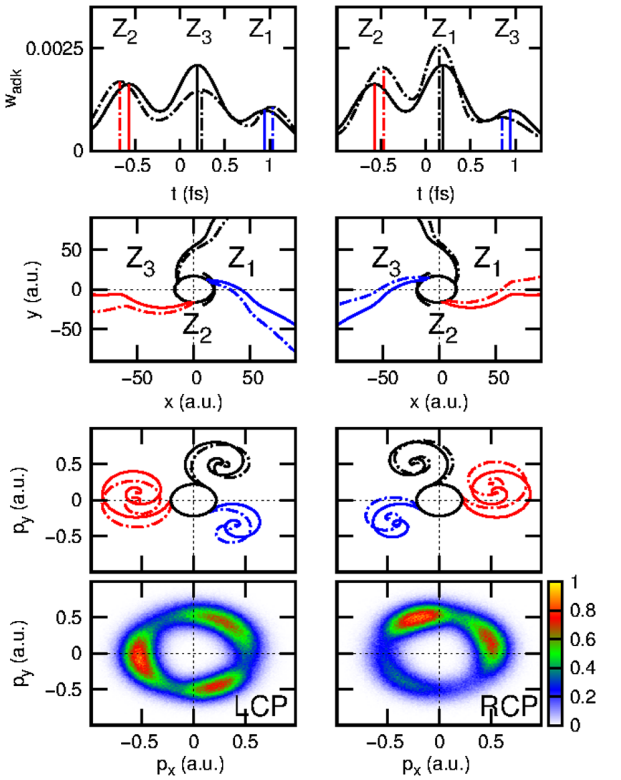

FIG. 4. Overview of the CTMC calculations for the short-range asymmetric potential environment subject to LCP (left column) and RCP (right column) laser fields, respectively. The upper panels display the ionization rate as a function of time for symmetric (solid) and asymmetric potentials (dashed lines). The second and third rows display selected trajectories in coordinate and momentum space. For comparison, also the corresponding trajectories of the symmetric case are displayed (solid lines), while the trajectories for the asymmetric case are represented by dashed lines. The lowest panels show the photoelectron momentum distributions as obtained from the CTMC calculations. Note that the red, blue, and black colors represent representative ionization events.

single-active electron model system aiming at answering the question of which information of the molecular electronic structure is imprinted in the photoelectron angular distributions when the system is ionized by intense, few-cycle circularly polarized laser pulses. We have shown that the symmetry of the molecular electronic structure is reflected in the photoelectron momentum distributions, and that Coulomb effects, both due to the presence of excited electronic states and the long-range character of the continuum, are visible in the photoelectron momentum distributions. These Coulomb effects, however, become much less pronounced for longer driving wavelengths; see also the Supplemental Material [46]. In the future, we will expand our investigations towards three-dimensional systems, aiming to describe multiphoton photoelectron circular dichroism occurring in the forward and backward direction with purely *ab initio* calculations. For this, the

results obtained from the calculations in two dimensions and the analysis of different methods in the current simple model system represent an important precursor.

The authors highly acknowledge financial support within the priority programme QUTIF (SPP) from the German Science Foundation (DFG), Grants No. GR 4482/3-1 and No. GR 4482/2-1. S. G. would like to acknowledge fruitful discussions with Professor Manfred Lein and Professor Ulf Saalmann.

*s.graefe@uni-jena.de

[1] K. L. Reid, Annu. Rev. Phys. Chem. **54**, 397 (2003).
[2] M. Yamazaki, J. i. Adachi, T. Teramoto, A. Yagishita, M. Stener, and P. Decleva, J. Phys. B **42**, 051001 (2009).
[3] N. Saito, K. Ueda, A. D. Fanis, K. Kubozuka, M. Machida, I. Koyano, R. Dörner, A. Czasch, L. Schmidt, A. Cassimi, K. Wang, B. Zimmermann, and V. McKoy, J. Phys. B **38**, L277 (2005).
[4] J. Adachi, K. Ito, H. Yoshii, M. Yamazaki, A. Yagishita, M. Stener, and P. Decleva, J. Phys. B **40**, 29 (2007).
[5] M. Wollenhaupt, M. Krug, J. Köhler, T. Bayer, C. Sarpe-Tudoran, and T. Baumert, Appl. Phys. B **95**, 647 (2009).
[6] A. Rouzée, Y. Huismans, F. Kelkensberg, A. Smolkowska, J. H. Jungmann, A. Gijsbertsen, W. K. Siu, G. Gademann, A. Hundertmark, P. Johnsson, and M. J. J. Vrakking, in *Ultrafast Phenomena in Molecular Sciences—Femtosecond Physics and Chemistry*, Spinger Series in Chemical Physics (Springer, New York, 2014), Vol. 107.
[7] L. Holmegaard, J. L. Hansen, L. Kalhoj, S. Louise Kragh, H. Stapelfeldt, F. Filsinger, J. Kupper, G. Meijer, D. Dimitrovski, M. Abu-samha, C. P. J. Martiny, and L. B. Madsen, Nat. Phys. **6**, 428 (2010).
[8] D. Dimitrovski, M. Abu-samha, L. B. Madsen, F. Filsinger, G. Meijer, J. Küpper, L. Holmegaard, L. Kalhøj, J. H. Nielsen, and H. Stapelfeldt, Phys. Rev. A **83**, 023405 (2011).
[9] J. L. Hansen, L. Holmegaard, L. Kalhøj, S. L. Kragh, H. Stapelfeldt, F. Filsinger, G. Meijer, J. Küpper, D. Dimitrovski, M. Abu-samha, C. P. J. Martiny, and L. B. Madsen, Phys. Rev. A **83**, 023406 (2011).
[10] V. R. Bhardwaj, D. M. Rayner, D. M. Villeneuve, and P. B. Corkum, Phys. Rev. Lett. **87**, 253003 (2001).
[11] X. Xie, K. Doblhoff-Dier, S. Roither, M. S. Schöffler, D. Kartashov, H. Xu, T. Rathje, G. G. Paulus, A. Baltuška, S. Gräfe, and M. Kitzler, Phys. Rev. Lett. **109**, 243001 (2012).
[12] X. Xie, K. Doblhoff-Dier, H. Xu, S. Roither, M. S. Schöffler, D. Kartashov, S. Erattupuzha, T. Rathje, G. G. Paulus, K. Yamanouchi, A. Baltuška, S. Gräfe, and M. Kitzler, Phys. Rev. Lett. **112**, 163003 (2014).
[13] X. Xie, S. Roither, M. Schöffler, E. Lötstedt, D. Kartashov, L. Zhang, G. G. Paulus, A. Iwasaki, A. Baltuška, K. Yamanouchi, and M. Kitzler, Phys. Rev. X **4**, 021005 (2014).
[14] B. Wolter, M. G. Pullen, A.-T. Le, M. Baudisch, K. Doblhoff-Dier, A. Senftleben, M. Hemmer, C. D. Schröter, J. Ullrich, T. Pfeifer, R. Moshammer, S. Gräfe, O. Vendrell, C. D. Lin, and J. Biegert, Science **354**, 308 (2016).
[15] T. Zuo and A. D. Bandrauk, Phys. Rev. A **52**, R2511 (1995).
[16] A. Giusti-Suzor, F. H. Mies, L. F. DiMauro, E. Charron, and B. Yang, J. Phys. B **28**, 309 (1995).
[17] T. Kjeldsen, L. Madsen, and J. Hansen, Phys. Rev. A **74**, 035402 (2006).
[18] A. Saenz, Phys. Rev. A **61**, 051402 (2000).
[19] M. Lein, E. Gross, T. Kreibich, and V. Engel, Phys. Rev. A **65**, 033403 (2002).
[20] S. Gräfe and M. Y. Ivanov, Phys. Rev. Lett. **99**, 163603 (2007).
[21] S. Saugout, C. Cornaggia, A. Suzor-Weiner, and E. Charron, Phys. Rev. Lett. **98**, 253003 (2007).
[22] C. Lefebvre, H. Z. Lu, S. Chelkowski, and A. D. Bandrauk, Phys. Rev. A **89**, 023403 (2014).
[23] A. Chen, M. F. Kling, and A. Emmanouilidou, Phys. Rev. A **96**, 033404 (2017).
[24] A. Chen, C. Lazarou, P. H., and A. Emmanouilidou, J. Phys. B **49**, 235001 (2016).
[25] K.-J. Yuan, H. Lu, and A. D. Bandrauk, J. Phys. B **50**, 124004 (2017).
[26] T. K. Kjeldsen, C. Z. Bisgaard, L. B. Madsen, and H. Stapelfeldt, Phys. Rev. A **71**, 013418 (2005).
[27] K. Doblhoff-Dier, M. Kitzler, and S. Gräfe, Phys. Rev. A **94**, 013405 (2016).
[28] A. Russakoff, S. Bubin, X. Xie, S. Erattupuzha, M. Kitzler, and K. Varga, Phys. Rev. A **91**, 023422 (2015).
[29] J. Caillat, J. Zanghellini, M. Kitzler, O. Koch, W. Kreuzer, and A. Scrinzi, Phys. Rev. A **71**, 012712 (2005).
[30] L. V. Keldysh, Zh. Eksp. Teor. Fiz. **47**, 1945 (1964) [Sov. Phys. JETP **20**, 1307 (1965)].
[31] F. H. M. Faisal, J. Phys. B **6**, L89 (1973).
[32] H. R. Reiss, Phys. Rev. A **22**, 1786 (1980).
[33] E. Hasović and D. B. Milošević, Phys. Rev. A **86**, 043429 (2012).
[34] D. B. Milošević, Phys. Rev. A **74**, 063404 (2006).
[35] D. Dimitrovski, C. P. J. Martiny, and L. B. Madsen, Phys. Rev. A **82**, 053404 (2010).
[36] V. I. Usachenko and S.-I. Chu, Phys. Rev. A **71**, 063410 (2005).
[37] N. Cherepkov, Chem. Phys. Lett. **87**, 344 (1982).
[38] R. L. Dubs, S. N. Dixit, and V. McKoy, Phys. Rev. Lett. **54**, 1249 (1985).
[39] C. Westphal, J. Bansmann, M. Getzlaff, and G. Schönhense, Phys. Rev. Lett. **63**, 151 (1989).
[40] C. Westphal, A. P. Kaduwela, C. S. Fadley, and M. A. Van Hove, Phys. Rev. B **50**, 6203 (1994).
[41] K. L. Reid, D. J. Leahy, and R. N. Zare, Phys. Rev. Lett. **68**, 3527 (1992).
[42] T. Jahnke *et al.*, Phys. Rev. Lett. **88**, 073002 (2002).
[43] O. Geßner, Y. Hikosaka, B. Zimmermann, A. Hempelmann, R. R. Lucchese, J. H. D. Eland, P.-M. Guyon, and U. Becker, Phys. Rev. Lett. **88**, 193002 (2002).
[44] D. Dowek, J. F. Pérez-Torres, Y. J. Picard, P. Billaud, C. Elkharrat, J. C. Houver, J. L. Sanz-Vicario, and F. Martín, Phys. Rev. Lett. **104**, 233003 (2010).
[45] M. Paul, L. Yue, and S. Gräfe, J. Mod. Opt. **64**, 1104 (2017).
[46] See Supplemental Material at http://link.aps.org/supplemental/10.1103/PhysRevLett.120.233202 for the model potentials, numerical details, and wavelength dependence of the photoelectron spectra.

[47] M. D. Feit, J. A. Fleck, and A. Steiger, J. Comput. Phys. **47**, 412 (1982).
[48] S. G. J. M. Frigo, ICASSP Conf. Proc. **3**, 1381 (1998).
[49] R. Heather and H. Metiu, J. Chem. Phys. **86**, 5009 (1987).
[50] A. Keller, Phys. Rev. A **52**, 1450 (1995).
[51] R. Kosloff and H. Tal-Ezer, Chem. Phys. Lett. **127**, 223 (1986).
[52] S. V. Popruzhenko, J. Phys. B **47**, 204001 (2014).
[53] J. E. Gentle, *Random Number Generation and Monte Carlo Methods* (Springer, New York, 2003).
[54] N. B. Delone and V. P. Krainov, J. Opt. Soc. Am. B **8**, 1207 (1991).
[55] O. Smirnova, M. Spanner, and M. Y. Ivanov, J. Phys. B **39**, S307 (2006).
[56] S. Gräfe, J. Doose, and J. Burgdörfer, J. Phys. B **45**, 055002 (2012).

Supplementary Material for Imprints of the molecular electronic structure in the photoelectron spectra of strong-field ionized asymmetric triatomic model molecules

Matthias Paul, Lun Yue and Stefanie Gräfe*
Institute for Physical Chemistry and Abbe Center for Photonics, Friedrich-Schiller Universität Jena, Germany
(Dated: May 8, 2018)

NUMERICAL DETAILS

Model Potentials

We employ our recently developed numerical model system [1] consisting of a single active electron with two spatial degrees of freedom $\boldsymbol{r} = (x, y)$ interacting with an intense, circularly polarized, infrared electric field $\boldsymbol{E}(t)$. Briefly, the dynamics of the system is governed by the time-dependent Schrödinger equation (TDSE) with reads (atomic units are used unless stated otherwise):

$$\mathrm{i}\frac{\partial}{\partial t}\,\psi(\boldsymbol{r},t) = \left[-\frac{1}{2}\nabla^2 + V(\boldsymbol{r}) + W(t)\right]\psi(\boldsymbol{r},t). \qquad (1)$$

In the above equation, $W(t)$ describes the interaction with the external field in velocity gauge:

$$W(t) = \boldsymbol{p}\cdot\boldsymbol{A}(t), \qquad (2)$$

with $\boldsymbol{p} = (p_x, p_y)$ the momentum operator and $\boldsymbol{A}(t) = (A_x, A_y)$ the vector potential. The vector potential is defined as

$$\begin{aligned} A_x(t) &= \pm\frac{E_0}{\omega} f(t)\sin\big[\omega(t-t_0) - \phi_{CEP}\big] \\ A_y(t) &= -\frac{E_0}{\omega} f(t)\cos\big[\omega(t-t_0) - \phi_{CEP}\big], \end{aligned} \qquad (3)$$

where the positive (negative) sign describes right- (left-) circularly polarized (RCP and LCP) fields. E_0 is the field strength, ω the laser frequency, ϕ_{CEP} the carrier-envelope phase (CEP), and t_0 the time when the Gaussian envelope $f(t)$ is maximum. The model potential $V(\boldsymbol{r})$ describes Coulomb repulsion between the three nuclei with charges Z_i fixed at nuclear positions $\boldsymbol{R}_i$, as well as the interaction of the electron with three nuclei.

$$\begin{aligned} V(\boldsymbol{r}) &= V_{nn} + V_{en}(\boldsymbol{r}) \\ V_{nn} &= \sum_{j<i}^{3}\frac{Z_i Z_j}{|\boldsymbol{R}_i - \boldsymbol{R}_j|}, \end{aligned} \qquad (4)$$

The positions of the nuclei are given as $\boldsymbol{R}_1 = (1.75, 1.01)$, $\boldsymbol{R}_2 = (0.00, -2.02)$, $\boldsymbol{R}_3 = (-1.75, 1.01)$, such that internuclear distance between two adjacent nuclei is 3.5 a.u., see Fig. 1, main manuscript. In this work, we aim at investigating the role of the excited electronic states, thus we employ different potentials describing the nuclear-electron attraction, including besides screened Coulomb interaction also short-range potentials

$$V_{en}(\boldsymbol{r}) = -\sum_{i=1}^{3}\frac{Z_i\exp\left(-\beta|\boldsymbol{r}-\boldsymbol{R_i}|^2\right)}{\sqrt{\left|\boldsymbol{r}-\boldsymbol{R}_i\right|^2 + \alpha}}. \qquad (5)$$

with the softening parameter $\alpha = 1$, and β defining the range of the potential. For all cases considered in this work, the nuclear charges Z_i and the soft-core (short-range) parameters are chosen such that the ionization potential is the same, $I_P = 8.64$ eV. Not that the system is such designed that for the symmetric configuration $Z_1 = Z_2 = Z_3$, the center of mass and charge lies at the origin of the coordinate system, and the system exhibits a mirror plane along the y axis. Table I lists the parameters for the charges Z_i and the resulting ionization potential I_P for the potentials discussed in this paper. The potential and the numbering of the nuclei is depicted in Fig. 2, main manuscript.

Model potential	Z_1	Z_2	Z_3	I_p (eV)	β ($\alpha = 1$)
$V_{sym,long}$	0.340	0.340	0.340	8.64	0.0
$V_{sym,short1}$	0.394	0.394	0.394	8.64	0.025
$V_{sym,short2}$	0.882	0.882	0.882	8.64	0.3
$V_{asym,1}$	0.812	0.862	0.953	8.64	0.3
V_{asym_2}	0.612	0.862	1.029	8.64	0.3

TABLE I. Parameters of the potentials utilized in this work, with the positions of the nuclei: $R_1 = (1.75, 1.01), R_2 = (0.00, -2.02), R_3 = (-1.75, 1.01), R_{nn}$= 3.5 a.u.

Quantum Dynamics

We numerically integrate the TDSE in Eq. (1) on a grid ranging $[-x_{\max}, x_{\max}] \times [-y_{\max}, y_{\max}]$, with $x_{\max} = y_{\max} = 220$ a.u, with 512 grid points in each direction, using the split-operator technique [2] and the FFTW 3 library [3]. The time step is set to be 0.001 fs. Electronic eigenstates $\varphi_n(\boldsymbol{r})$ are obtained via imaginary time propagation [4]. In all results presented in this work, the initial state is the electronic ground state $\varphi_1(\boldsymbol{r})$.

The photoelectron spectra are obtained by dividing the grid into an inner and outer region. In the inner region, the propagation is performed with the full Hamil-

tonian, while in the outer, asymptotic region, the nuclear-electron interaction is neglected and the electron dynamics evolve in momentum space, subject to the Hamiltonian $T+W(t)+V_n$. In every time step, the wave function is multiplied by a mask function $c(\boldsymbol{r})$ [5, 6]

$$c(\boldsymbol{r}) = \left[1 + \mathrm{e}^{(|x|-x_{\max}/1.3)/\epsilon}\right]^{-1} \left[1 + \mathrm{e}^{(|y|-y_{\max}/1.3)/\epsilon}\right]^{-1}, \tag{6}$$

with $\epsilon = 6$ being the smoothing parameter, thereby splitting the total wave function into an inner part, $\psi_{in}(\boldsymbol{r},t) = c(\boldsymbol{r})\psi(\boldsymbol{r},t)$, and an outer part, $\psi_{out}(\boldsymbol{r},t) = [1-c(\boldsymbol{r})]\psi(\boldsymbol{r})$. Every time step, the outer part of the wave function is Fourier-transformed into momentum space and coherently added to the previously absorbed parts. At asymptotic times $t \to \infty$, the total momentum wave function $\psi_{out}(\boldsymbol{p}, t \to \infty)$ directly yields the spectra

$$\sigma(\boldsymbol{p}) = \left|\psi_{out}(\boldsymbol{p}, t \to \infty)\right|^2. \tag{7}$$

The time limit is defined as the time when the norm of the wave function in the inner (or outer) region becomes constant, which is the case at $t_{end} = 50$ fs for the calculations with $\lambda = 800$ nm.

Classical Trajectory Monte Carlo Calculations

Ensembles of classical trajectories are propagated mimicking the electronic dynamics of the quantum system. The dynamics of each trajectory is described by Newton's equations of motion,

$$\frac{\partial \boldsymbol{r}}{\partial t} = \boldsymbol{p} \tag{8}$$

$$\frac{\partial \boldsymbol{p}}{\partial t} = -\nabla[V(\boldsymbol{r}) + \boldsymbol{r}\boldsymbol{E}(t)]. \tag{9}$$

The initial condition of each trajectory represents one phase-space coordinate of the quantum system and is randomly chosen. Here, each trajectories starts with an initial transverse momentum following the Delone-Krainov momentum distribution [7]. We would like to note that for the $\lambda = 800$ nm calculations – in the multi-photon case – we shift the center of the perpendicular Gaussian momentum distribution around by $\boldsymbol{p_0} = \pm 0.22$ a.u., (with the + sign for LCP, and the − sign for RCP pulses) corresponding to the excess energy the electron will acquire in the above-threshold ionization case. For the calculations at longer wavelenghts, $\lambda = 1800$ and 3000 nm, the center of the initial Gaussian distribution in momentum space is located at $\boldsymbol{p_0} = 0$ a.u., as this is more in the tunneling regime of ionization. The width of the perpendicular momentum distribution is given by [7]

$$\sigma_{perp} = \sqrt{\frac{\omega}{2\gamma}} \tag{10}$$

The initial coordinate values are located at the classical tunnel exit. The tunnel exit $\boldsymbol{r}_0$ is numerically found using the Newton-Raphson method, specifically by defining at each time t_i a parametric line pointing in the direction of the electric field vector, $\boldsymbol{E}(t_i)$. The coordinate of the tunnel exit is defined as the point when the value of the combined potential $V(\boldsymbol{r}) + \boldsymbol{r} \cdot \boldsymbol{E}(t_i) = -I_P$.

Typically, 10^6 trajectories are propagated by numerically integrating the Newton equations (eqs. 8, 9) applying a Runge-Kutta algorithm of fourth order with adaptive stepzise control.

For the ionization rate, we apply a modified expression taking into account the non-spherical symmetry of the model system, which, consequently, leads to spatially anisotropic tunneling rates. We adapt the expression for the tunnel rate Γ from the recent review by Popruzhenko [8], which includes the dependence on the Keldyhsh-parameter γ in the exponential term:

$$\Gamma_{Popr} \propto \exp\left[-2K_0 f_K(\gamma)\right], \tag{11}$$

with $K_0 = I_P/\omega$ representing the number of photons required for ionization, and the so-called Keldysh function $f_K(\gamma)$ given by

$$f_K(\gamma) = \left(1 + \frac{1}{2\gamma^2}\right) \operatorname{arcsinh}\gamma - \frac{\sqrt{1+\gamma^2}}{2\gamma}. \tag{12}$$

In order to account for different barrier widths of the molecular model system, instead of utilizing the expression for the Keldysh-parameter γ

$$\gamma = \frac{\sqrt{2I_P}\omega}{E}, \tag{13}$$

we directly include the barrier width b_0 into the expression: As the Keldysh-parameter γ can be interpreted as the ratio of the time the electron takes to cover the distance b_0 moving with the atomic velocity $v_{at} = \sqrt{2I_P}$, we express γ in the following form:

$$\gamma = \frac{b_0\,\omega}{v_{at}} = \frac{b_0\,\omega}{\sqrt{2I_P}}. \tag{14}$$

As described above, we calculate the barrier widths b_0 at every time step numerically and insert the corresponding value into the instantaneous Keldysh-parameter and thus, the ionization rate.

We mimic the initial Gaussian distributions by transforming the calculated random numbers (RAN2) by a Box-Muller transform [9].

In the case of the asymmetric potentials, we need to include a permanent dipole moment $\boldsymbol{\mu}$. In our CTMC calculations, this is addressed by calculating the tunnel exits via the condition:

$$V(\mathbf{r}) + (\mathbf{r} + \boldsymbol{\mu})\mathbf{E}(t_i) + I_p = 0 \tag{15}$$

Strong-Field Approximation

The molecular system in its initial state $\psi_i(t)$ propagates up to a time τ subject to the molecular potential only. At time τ, ionization occurs and the electron is propagated in the laser field only, completely neglecting the molecular potential. The final state can be described by the Volkov function $\psi_{\boldsymbol{p}}^V(t)$. The ionization process is described by the (SFA) transition amplitude

$$M(\boldsymbol{p}) = -\mathrm{i}\int^{\infty} \mathrm{d}\tau\, \langle \psi_{\boldsymbol{p}}^V(\tau)|W(\tau)|\psi_i(\tau)\rangle. \qquad (16)$$

The time evolution of the ground state,

$$\psi_i(\tau) = \mathrm{e}^{\mathrm{i}I_P\tau}\varphi_1(\boldsymbol{r}) \qquad (17)$$

and of the Volkov state

$$\psi_{\boldsymbol{p}}^V(\tau) = \frac{1}{\sqrt{2\pi}} \times \exp\left[\mathrm{i}(\boldsymbol{p}+\boldsymbol{A}(\tau))\cdot\boldsymbol{r} - \frac{\mathrm{i}}{2}\int^{\tau} \mathrm{d}t''(\boldsymbol{p}+\boldsymbol{A}(t''))^2\right] \qquad (18)$$

are analytically known. The photoelectron momentum distribution $\sigma(\boldsymbol{p})$ is obtained from the absolute squared of the transition amplitude [10–12],

$$\sigma^{SFA}(\boldsymbol{p}) = |M^{SFA}(\boldsymbol{p})|^2 = \left|-\mathrm{i}\int^{\infty} \mathrm{d}\tau \langle \boldsymbol{p}+\boldsymbol{A}(\tau)|\boldsymbol{r}\cdot\boldsymbol{E}(\tau)|\varphi_1\rangle\, \mathrm{e}^{\mathrm{i}S(\tau)}\right|^2 \qquad (19)$$

In above equation, $\langle \boldsymbol{p}+\boldsymbol{A}(\tau)|$ refers to a plane wave with momentum $\boldsymbol{p}+\boldsymbol{A}(\tau)$ and the action $S(\tau)$ is given by

$$S(\tau) = I_P\tau + \frac{1}{2}\int^{\tau} \mathrm{d}t''(\boldsymbol{p}+\boldsymbol{A}(t''))^2. \qquad (20)$$

Numerically, for each time τ we calculate first

$$A_p(\tau) = e^{-i\mathbf{A}(\tau)\cdot\mathbf{r}}\mathbf{r}\cdot\mathbf{E}(\tau)\varphi_1(\boldsymbol{r}), \qquad (21)$$

Fourier transform this expression into momentum space by using the FFTW3-library [3], and multiply the result by the action $e^{iS(\tau)}$. Subsequently, we sum over the calculated transition amplitudes for each time step τ, multiply by $-idt$ and calculate the absolute squared to obtain the final photoelectron momentum distribution $\sigma^{SFA}(\boldsymbol{p})$.

For calculating the EPMD $\sigma^{SFA}(\boldsymbol{p})$ of the asymmetric model system, we include the permanent dipole $\boldsymbol{\mu}$

$$\boldsymbol{\mu} = -\langle\varphi_1|\boldsymbol{r}|\varphi_1\rangle \qquad (22)$$

in the calculation by performing a coordinate transformation $(x,y) = (x+\mu_x, y+\mu_y)$. This way, the center of charge of the asymmetric model system remains at the origin of coordinate system.

ASYMMETRIC POTENTIAL

SFA Calculations

In the following, additional information for the case of asymmetric potentials is given. Figure 1 shows the corresponding SFA results for left- and right- circularly polarized light in an asymmetric nuclear potential environment. As described in the main text, the difference in the intensity pattern caused by the field is captured in the corresponding photoelectron momentum distributions obtained by SFA calculations.

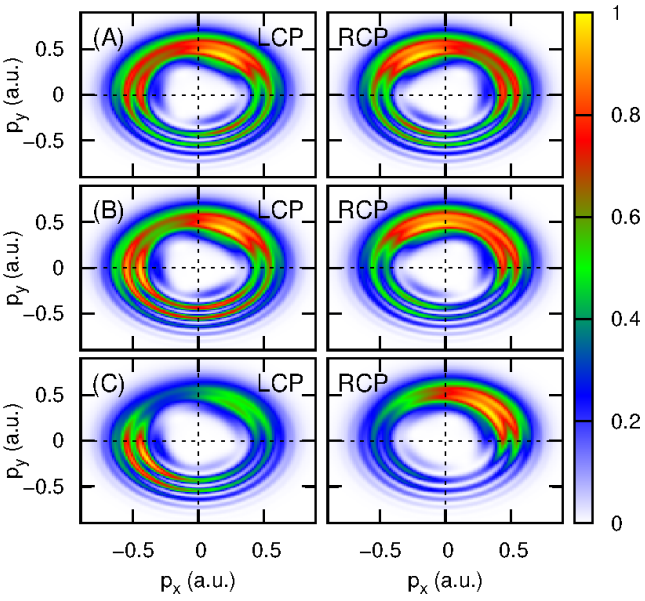

FIG. 1. As in Fig. 3, main manuscript: photoelectron momentum distributions for LCP (left) and RCP (right) fields calculated using the SFA: (A) symmetric case, (B,C) for asymmetric potentials. The degree of asymmetry of the potentials increases from the (B) to (C).

TDSE Calculations

Figure 2 displays snapshots of the electron density in coordinate space $|\psi(x,y,t_{fix})|^2$ for three different times, comparing symmetric and asymmetric (short-range) potentials, compare to Fig. 4, main text. It can be seen that the asymmetric potential environment causes distinct differences in the dynamics of the continuum electron wavepacket, depending on the direction of the polarization of the pulses. Thereby, Z_3 (located in the second quadrant, see Fig. 2, main manuscript) causes the most pronounced differences, while Z_1 (located in the first quadrant) causes the smallest differences. We would like to note parenthetically that also the absolute ionization yield (and the ionization rates) for the asymmetric

potentials in LCP and RCP pulses differ.

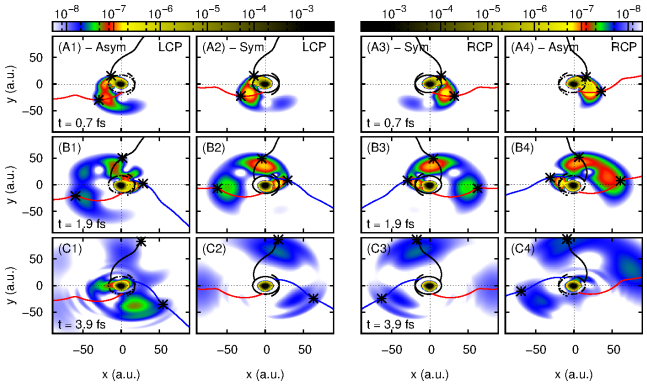

FIG. 2. As in the main manuscript, snapshots of the electron density in coordinate space $|\psi(x, y, t_{fix})|^2$ for three different times, comparing symmetric and asymmetric (short-range) potentials, as labelled. Left panels: LCP pulses, right panels: RCP pulses. Overlaid are representative classical trajectories.

Wavelength Dependence

We finally discuss the wavelength dependence of the photoelectron momentum distributions for the symmetric model potentials. In Fig. 3, we compare results of the SFA calculations (A1–A3) with those obtained by the numerical solution of the time-dependent Schrödinger equation for short-range (B1–B3), long-range Coulomb potentials (C1–C3) and long-range CTMC calculations (D1–D3). While for the $\lambda = 800$ nm case, the above discussed three-fold symmetric structure can be gathered, going from $\lambda = 1800$ nm (middle column) to $\lambda = 3000$ nm, the photoelectron momentum distributions become much smoother and a ring-shaped structure with a pronounced maximum in the first quadrant, around $\boldsymbol{p} = (0.5, 0.8)$ ($\lambda = 1800$ nm) and $\boldsymbol{p} = (0.6, 1.0)$ ($\lambda = 3000$ nm) builds up. Please note, that still features of the three-fold structure remain visible. Not surprisingly, we can see that increasing the wavelength towards the mid-IR regime, SFA, TDSE and CTMC calculations agree much better. Also, while for $\lambda = 1800$ nm, shifts caused by the long-range nature of the Coulomb potential can be gathered, these become less pronounced for $\lambda = 3000$ nm. This indicates, that for these longer wavelengths, not only the importance of excited electronic states is minor, but also the long-range character imprints much smaller changes/shifts to the photoelectron momentum distributions. Excited states are expected to play a minor role, as for longer wavelengths the tunneling mechanism to ionization becomes more important compared to the multiphoton mechanism. The long-range character is less important, as the electron upon "occuring" in the continuum is driven away from the parent ion by a stronger vector potential and thus is not attracted by the Coulomb potential substantially. Thus, the intensity distribution of the photoelectron momentum distributions is dominated by the electric field and here, for the few-cycle pulses considered, by the CEP of the pulse.

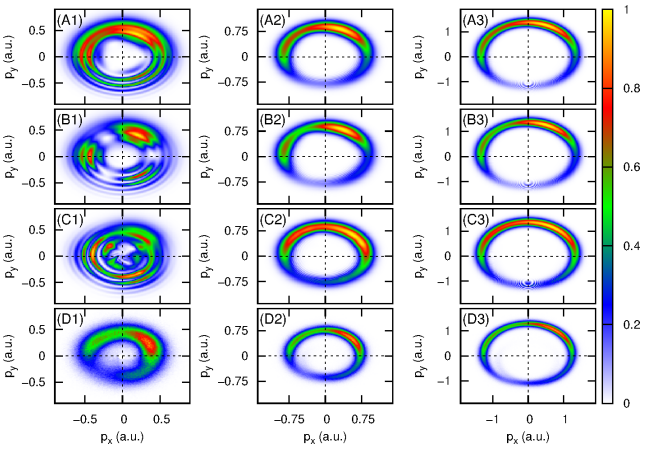

FIG. 3. Photoelectron momentum distributions for pulses with different wavelengths λ, while keeping the field strength, CEP and number of cylces constant. (A) depicts results from the (short-range) SFA; (B) short-range TDSE; (C) Coulomb-type TDSE, (D) long-range CTMC. Column (1): $\lambda = 800$ nm, column (2): $\lambda = 1800$ nm, column (3): $\lambda = 3000$ nm.

BIBLIOGRAPHY

* s.graefe@uni-jena.de

[1] M. Paul, L. Yue, and S. Gräfe, J. Mod. Opt. **64**, 1104 (2017).
[2] M. D. Feit, J. A. Fleck, and A. Steiger, J. Comput. Phys. **47**, 412 (1982).
[3] S. G. J. M. Frigo, ICASSP conference proceedings **3**, 1381 (1998).
[4] R. Kosloff and H. Tal-Ezer, Chem. Phys. Lett. **127**, 223 (1986).
[5] R. Heather and H. Metiu, J. Chem. Phys. **86**, 5009 (1987).
[6] A. Keller, Phys. Rev. A **52**, 1450 (1995).
[7] N. B. Delone and V. P. Krainov, J. Opt. Soc. Am. B **8**, 1207 (1991).
[8] S. V. Popruzhenko, Journal of Physics B: Atomic, Molecular and Optical Physics **47**, 204001 (2014).
[9] J. E. Gentle, *Random Number Generation and Monte Carlo Methods* (Springer, 2003).
[10] L. Keldysh, Sov. Phys. JETP **20**, 1307 (1965).
[11] F. H. M. Faisal, J. Phys. B: At. Mol. Phys. **6**, L89 (1973).
[12] H. R. Reiss, Phys. Rev. A **22**, 1786 (1980).

3.3 Paper 3: Strong-field ionization dynamics of asymmetric equilateral triatomic model molecules in circularly polarized laser fields

The paper "Strong-field ionization dynamics of asymmetric equilateral triatomic model molecules in circularly polarized laser fields" aims at unraveling the exact influence of excited states on the ionization dynamics of triatomic model molecules with different internuclear distances. For a detailed characterization of the ionization process, a combination of full ab-initio quantum dynamical simulations with a modified version of the classical trajectory Monte-Carlo (CTMC) method and an extended version of the strong-field-approximation (SFA) was applied. Here, the CTMC was primarily employed to study the long-range Coulomb interaction between the photoelectrons and the parent ion, whereas the extended version of the SFA was developed to investigate the exact influence of the first two excited bound states on the ionization process. Thus, the effect of excited states and long-range Coulomb interactions on the PEMDs are efficiently simulated. Finally, the influence of different molecular orientations on the PEMDs was investigated.
Thus, in order to theoretically describe the strong-field ionization of larger molecules, several approaches exist, e.g. the real-time real-space time-dependent density functional theory (RT-TDDFT) [143–145] and the molecular SFA [81, 83]. However, these approximate methods introduce new sources of errors; e.g. the self-interaction of the electrons (RT-TDDFT) and the asymptotic behavior in the continuum (molecular SFA) are described inaccurate. On the other hand, fully numerical treatment without using such approximations is not feasible for systems larger than prototypes molecules, such as H_2^+ [75], HeH^+ [146], and H_3^{2+} [112, 113]. Especially, the non-colinear arrangement of H_3^{2+} and the permanent dipole of the linear molecule HeH^+ render a theoretical description much more challenging than the linear diatomic molecule H_2^+, which features an inversion symmetry.
The focus of this study is set on variations of the simplest non co-linear polyatomic molecule H_3^{2+} interacting with few-cycle circularly polarized electric fields. As before, the model system itself consists of an single active electron with two spatial degrees of freedom $\mathbf{r} = (x, y)$ and three nuclei with fixed positions, forming a equilateral triangle. To mimic nuclear motion, model systems with different internuclear distances R_{ij} of 3.5 and 5.5 au were simulated. By tuning the range of the potential, the number of bound states was systematically reduced. In order to keep the same regime of strong-field ionization for all model systems, the parametrization is chosen such that the I_p is kept constant for all cases (Tab. 1 in Paper 3). For the described model system, the

TDSE was numerically integrated on a two dimensional grid using the split-operator technique [132] and the FFTW3 library [142] as outlined in Sec. 2.2. The photoelectron spectra are calculated via the wavefunction splitting method [137, 138] (see. Sec. 2.2.4). The first three electronic eigenstates ϕ_n, $n \in \{1, 2, 3\}$, are obtained via the imaginary time propagation [134] (see Sec. 2.2.3), and the corresponding time-dependent coefficients $c_n(t)$ were extracted by projection from the numerically propagated wavefunction $\psi(t)$ of the TDSE simulation. They built the foundation for the calculation of the time-dependent superposition state: $\psi_s(\mathbf{r}, t) = \sum_{n=1}^{3} \langle \phi_n | \psi(t) \rangle \phi_n(\mathbf{r}) = c_n(t)\phi_n(\mathbf{r})$. To obtain the PEMDs within the SFA formalism, the time-integrals in Eq. (2.56) were numerically calculated, while the initial state ψ_i was either chosen to be the electronic groundstate $\psi_0(\mathbf{r}) = \phi_1(\mathbf{r})$ or the time-dependent superposition state $\psi_s(\mathbf{r}, t)$. The post-ionization dynamics was studied via classical trajectories with initial conditions according to the SMM model (see Sec. 2.3.2). Depending on the model potential (table 1 in Paper 3) and the ionization regime, the initial conditions were slightly modified (for details see Paper 3). In order to account for the spatial anisotropy of the model molecule, the ionization rate was calculated numerically via the tunnel barriers [Eq. (2.61) and (2.62)]. Classical trajectories were calculated by solving the classical Newton's equation of motion [Eq. (2.7)] by employing a Runge-Kutta algorithm of fourth order with adaptive step-size control (Cash–Karp method [140]).

First, the symmetric short-range model is studied, where the number of excited states is finite. The evolution of the electronic density in the continuum was presented in form of snap-shots of the electronic density at certain times t. The electronic density snapshots clearly showed that a three-fold structure is built up during the course of ionization. Each of these three ionization events could be traced back to one representative trajectory. The trajectories start at three temporally well-separated ionization events near the nuclei Z_1, Z_2, and Z_3, respectively, at times when the tunnel barrier b_0^M is narrow and hence the ionization rate is high. The ionization occurs from the groundstate at the "down-field side" of the electric field vector (see Fig. 1 in Paper 3). In the multiphoton regime ($\lambda = 800$ nm), the classical trajectories of the CTMC method need an additional initial momentum $\mathbf{p}_\perp$. Only if $\mathbf{p}_\perp$ is equal to 0.22 au, the momenta of the three peaks in the PEMD are sufficiently high enough to generate results similar to those from TDSE simulations.

For the system with a larger internuclear distance ($R_{ij} = 5.5$ au), a different ionization behavior was found. The three-fold structure in both, the electron density snapshots and the PEMDs, was rotated by about 60°. Also the intensity pattern changed significantly (see Fig. 3 in Paper 3). CTMC simulations revealed that ionization occurs here from the excited state at the nuclei from the "up-field site" of the electric field vector (see Fig. 1 in Paper 3), thus giving rise to an alternative ionization mechanism to the one

already observed in the system with shorter internuclear distance ($R_{ij} = 3.5$ au). The three trajectories with the highest ionization probability start at different times from different tunnelexits and consequently from different nuclei at the "up-field site" of the electric field vector. The three representative trajectories are qualitatively in very good agreement with the results of the TDSE simulation and thus provide an accurate model to describe the evolution of the electronic density in the continuum with its 60° shift (see Fig. 3 in Paper 3).

In order to understand the influence of the excited states qualitatively, a extended version of the SFA was applied, in which the ionization occurs from the time-dependent superposition state $\psi_s(r,t)$. The dynamics of this bound superposition state ψ_s was examined for both systems with internuclear distance R_{ij} of 3.5 and 5.5 au, respectively. Depending on the internuclear distance, a strong localization of the electronic density peaked along the direction ($R_{ij} = 3.5$ au, "down-field side") or in the opposite direction ($R_{ij} = 5.5$ au, "up-field side") of the electric field vector [see. Fig. 4 in Paper 3]. This indicates that the ionization occurs from different nuclei, which means that the ionization mechanism depends on the internuclear distance of the triatomic model system. The PEMDs calculated with the standard and an extended version of the SFA illustrates the importance of the excited states during ionization. Only the extended SFA was able to reproduce all significantly features appearing in the PEMDs of the TDSE calculations. The deviations between the standard SFA and the TDSE was more significant in the system with a higher internuclear distance, since here the excited states are energetically closer, resulting in a strong-mixing of the first two bound excited states (quasi-resonant population transfer) with the ground-state.

For Coulomb-like systems, the electronic structure in the PEMDs become more complex and new features arise at small momenta. This finger-like structure is a result of ionization from higher-lying excited states with lower binding energy and is located at small momenta within the three-fold ATI-ring structure. Here, the three-fold electronic structure is only weakly pronounced and the corresponding peaks are rotated clockwise in comparison to the peaks observed in the PEMD of the short-range system (see. Fig. 7 in Paper 3). The corresponding kinetic energy spectrum $\sigma(E_{kin}, \phi)$ revealed that the released wavepacket is decelerated during its evolution in the continuum resulting in energetically lowered ATI-rings. The classical trajectories obtained from the CTMC method successfully reproduced both, the energy shift and the clockwise rotation (ϕ decreases) of the ATI peaks. However, the PEMD intensity pattern obtained by the TDSE simulation could only be reproduced for the short-range system. For Coulomb like systems, on the other hand, with a larger internuclear distance $R_{ij} = 5.5$ au, a different tunnel-mechanism was proposed since the over-the-barrier mechanism becomes dominant. The initial phase-space condition were

changed: The inital position $r_i(t_0)$ was chosen to be at the maximum of the tunnel-barrier, and the initial momentum $p = (p_\parallel, p_\perp)$ was modified in parallel direction of the laser-field with $p_\parallel = \sqrt{2E_{OBI}}$, where E_{OBI} corresponds to the excess energy [see. Fig. 8 in Paper 3]. The change in momentum leads to a counterclockwise rotation of the trajectories in momentum space. The same shift was observed in the triatmomic structure of the PEMDs obtained by the TDSE calculation.

The PEMDs calculated with the extended SFA (Coulomb-like systems) are in good agreement with the PEMDs obtained by the TDSE simulation: both the clockwise ($R_{ij} = 3.5$ au) and counterclockwise ($R_{ij} = 5.5$ au) rotation of the three peaks could be reproduced quantitatively. This means that both, the excited states and the long-range interaction, induce the same shift (only for systems with $R_{ij} = 3.5$ au), which eventually leads to a clockwise rotation of the triatomic electronic structure. However, not all features in the PEMDs could be reproduced due to the limited number of excited states considered in superposition state ψ_s.

Until now, only the PEMDs of the symmetric system are considered, where all nuclear charges Z_1, Z_2, and Z_3 are equal. They thus exhibit a mirror axis along the p_y-axis and the vectors of the LCP and RCP electric fields are chosen so that they are mirror images of each other along the p_y-axis. The resulting PEMDs behave therefore like mirror image as well. For asymmetric systems, where all charges are different, this symmetry relation is broken. Resulting asymmetric changes in the intensity profile of the PEMDs were examined by an extended version of the CTMC model. Within this extended version, new tunnel exits and, consequently, ionization probabilities, Eq. (2.62), were calculated by including the Stark shift $\boldsymbol{\mu}\mathbf{E}$ in Eq. (2.61), where $\boldsymbol{\mu}$ is defined as the permanent dipole of the asymmetric groundstate ($\boldsymbol{\mu} = -\langle\psi_0|\mathbf{r}|\psi_0\rangle$). Here, the intensities of the ionization probability maxima $w_k(t_{max})$ and the time t_{max} of their appearance are changed significantly when the Stark shift is included in the simulation. The altered ionization probability maxima $w_k(t_{max})$ were assigned to the three nuclei Z_1, Z_2, and Z_3, giving insight into the ionization dynamics of such asymmetry systems. For laser wavelength of $\lambda = 3000$ nm (tunnel-regime) and Coulomb-like systems, the resulting PEMDs are in very good agreement with results obtained in TDSE simulations. This indicates that ionization from the nuclei Z_3 and Z_2 is strongly suppressed for the LCP-case, whereas ionization from the nuclei Z_1 and Z_2 is strongly enhanced in the RCP case (see. Fig. 11 in Paper 3). In the multiphoton regime ($\lambda = 800$ nm), the number of involved excited states complicates the analysis of obtained spectra significantly. Furthermore, the trajectory model cannot explain the complex asymmetric changes in the PEMDs (see. Fig. 10 in Paper 3). Even the extended SFA was not able to reproduce the features appearing in the PEMDs of the TDSE simulations. The best agreement with results of the TDSE were obtained for

asymmetric short-range systems: here, a qualitatively correct electronic structure was obtained, but the calculated intensity profiles were inaccurate. The approximations made in the SFA address only the pre-exponential factor in the ionization rate (see Sec. 2.3.1), which may result in spectra with inaccurate intensities even for short-range systems.
Under typical experimental conditions, the molecules are typically not aligned with respect to the laser-field, but the shape of the PEMD depends on the molecular potential and thus on its orientation in space. The paper investigated how the threefold pattern in the PEMD changes for different orientations of the triatomic model molecule [see. Fig. 12 in Paper 3]. This threefold structure disappears when the PEMD is averaged over all molecular orientation. In that case, only the ATI-ring structure remains as a clear structure in the PEMD. The corresponding intensity profile depends on the electric field parameters, such as the CEP and the pulse duration, but not on the molecular potential itself.
The CDAD spectra were defined as the difference of the PEMDs induced by left- and right- circularly polarized laser fields. For short-pulse durations, a pronounced CDAD effect was observed, which strongly depends on the CEP of the electric field (see Fig. 14 in Paper 3). However, for laser fields with longer pulse durations, the corresponding CDAD effects become smaller. For Coulomb-like systems, the overall shape of the CDAD-effect changes since the related molecular averaged PEMDs are strongly affected by long-range interaction and excited states contributions (LCP/RCP: clockwise/counterclockwise rotation of the peak structure). The averaged PEMDs and thus the CDAD spectra of the symmetric and asymmetric Coulomb-like systems differ not significantly from each other (see Fig. 16 in Paper 3). This indicates that the CDAD-effect is primarily produced by the CEP of the laser field and not by the asymmetry of the potential.

Contribution to the appended publication

- Paul, M. and Gräfe, S.
  Strong-field ionization dynamics of asymmetric equilateral triatomic model molecules in circularly polarized laser fields.
  Phys. Rev. A submitted for publication (submission number: AY11760).

authors:	**Paul, M.**	**Gräfe, S.**
creating the program code	X	
running the simulations	X	
analyzing the results	X	X
generating images	X	
writing the manuscript	X	X
revision of the manuscript	X	X
publication equivalents	**1.0**	-

Next, the article 'Strong-field ionization dynamics of asymmetric equilateral triatomic model molecules in circularly polarized laser fields.' will be reprinted [Reprinted from Paul et al. Phys. Rev. A submitted for publication (with permission from Gräfe, S.). Unpublished work copyright 2019 American Physical Society.].

Strong-field ionization dynamics of asymmetric equilateral triatomic model molecules in circularly polarized laser fields

Matthias Paul and Stefanie Gräfe*

Institute for Physical Chemistry and Abbe Center for Photonics,

Friedrich-Schiller Universität Jena, Germany

(Dated: February 28, 2019)

Abstract

The strong-field driven ionization dynamics of larger, non-diatomic molecules still constitutes a major challenge for the theoretical and numerical description. While a full numerical treatment of all electronic and nuclear degrees of freedom is computational prohibited, several approaches exist to model photoelectron spectra employing certain approximations. Among them are classical trajectory methods or the so-called strong-field approximation (SFA). Here, we investigate in detail the strong-field ionization dynamics of simple, non-co-linear triatomic model systems. For a detailed characterization of the ionization process of our system, we combine quantum dynamical simulations, modified classical trajectory calculations, and extensions of the SFA in order to analyze the complex pattern of the photoelectron momentum distribution. We aim at disentangling the contributions of excited states and the long-range character of the potential. We show that upon interaction with circularly polarized laser fields, the long-range character merely induces a small shift in the spectra, while the contribution of excited states is in several cases essential: in particular in near-infrared laser fields, compared to mid-infrared drivers, and for systems with larger internuclear distances, when excited electronic states are energetically closer. Key modifications are for our trajectory model to explicitly incorporate the numerically obtained tunnel barrier width directly into the ionization rate, thereby enabling a spatially anisotropic ionization rate, and an approximate treatment of the contribution of excited states via the Stark shift. In contrast, for the SFA, it is important to include electronically excited states for the description of the initial state. We also discuss the effect of the carrier-envelope phase on the ionization dynamics, as well as the influence of molecular averaging.

* s.graefe@uni-jena.de

I. INTRODUCTION

The interaction with short and strong light fields with molecules gives rise to many different phenomena, starting from excitation of possibly many rotational, vibrational and electronic states to (multiple) ionization, for a great overview, see, e.g. Refs. [1, 2]. An accurate description of the strong-field response of even small or medium-sized molecules with all degrees of freedom is computationally prohibitive. Thus, in order to theoretically model the strong-field dynamics, several approaches exist: (a) The dynamics is modeled by instead of numerically solving the time-dependent Schrödinger equation (TDSE), e.g. the multi-configurational time-dependent Harte-Fock equations [3–7], or the real-time real-space time-dependent density functional theory (RT-TDDFT) is employed, and the time-dependent Kohn-Sham orbitals are propagated on a spatial grid [8–14]. While this enables to treat real molecules and their ionization dynamics, several problems are known, mainly related to the proper choice of the exchange-correlation functional. Among them, the wrong asymptotic behavior of the electrostatic potential, the self-interaction of the electron and the description of the nuclear dynamics, which is mainly incorporated via a mean-field (Ehrenfest) approach. Of course, several approaches exist how to diminish these problems [15]. However, it is hard to draw generalized conclusions from these calculations. (B) Approximations are introduced, such as the separation of nuclear and electronic degrees of freedom, the single-active electron approximation [16, 17] or the (molecular) strong-field approximation (SFA) [18–23], which assumes that the laser field is strong that the (molecular) Coulomb potential merely represents a small perturbation to the electron after ionization, and can be neglected. Alternatively, instead of a quantum description of dynamics, some or many degrees of freedom are either frozen or represented by classical dynamics. The latter has the advantage that it can provide insight into the ionization dynamics. (C) Fully numerical treatment of all degrees of freedom for prototype molecular systems [7]. As a consequence, most of our current understanding of strong-field ionization dynamics, is based on the investigation with small diatomic molecules, and here, in particular the prototype molecule H_2^+ (and H_2) [24–29]. While nowadays a full-dimensional treatment of the strong-field driven, coupled nuclear-electronic dynamics is possible [30, 31], and, also together with simulations with reduced dimensionality, have led to important insight into the strong-field dynamics of molecules in general, this particular model system H_2^+ may not recover all aspects of the

general strong-field response of larger molecules, as it: (i) features inversion symmetry and no permanent dipole, (ii) is linear, and (iii) has a large transition dipole moment between the lowest electronic states, which linearly increases as a function of the internuclear distance, leading to pronounced population transfer and electron localization dynamics. Thus, several other, simple molecules (and model molecules) have been examined, in order to address some of the features not inherent to H_2^+. Among them are HeH^+, which features a pronounced charge asymmetry and thus, a permanent dipole moment [32–36], or H_3^{2+}, which is non co-linear [37–39].

In this work, we aim at extending the physical understanding of the strong-field ionization dynamics of small, non co-linear model molecules by systematically investigating their dynamics, thereby employing a large toolbox of different methods. We consider different prototypical aspects of strong-field ionization: (A) We compare symmetric and asymmetric systems and analyze the imprint of the charge asymmetry (permanent dipole moment) to the ionization dynamics. (B) We investigate regular and stretched nuclear geometries and analyze the increased importance of electronically excited states for the latter. (C) We consider the interaction of these systems with different laser wavelengths, ranging from the near to the mid-infrared and describe the difference in the ionization dynamics. (D) We consider molecules, which are not fixed in space but may take different orientations. (E) All these investigations are done by numerically solving the TDSE for one single active electron as a reference, and analyzing these dynamics with the help of classical trajectory calculations and utilizing the strong-field approximation. By tuning the range of the potential, we disentangle contributions of the excited states from long-range contributions. We show, that with some small modifications to the standard methods for both, classical trajectory and SFA methods, major parts of the full quantum dynamics can be reliably be described. Key modifications are for the trajectory model to explicitly incorporate the numerically obtained tunnel barrier width directly into the ionization rate, thus enabling a spatially anisotropic ionization rate, and an approximate treatment of the contribution of excited states via the Stark shift. In contrast, for the SFA, key is the consideration of excited states for the description of the initial state.

The focus lies here on the interaction with short, circularly polarized laser fields, as we are aiming to generalize our considerations in a future work for non-planar systems, giving rise to circular dichroism in the emission direction of photoelectrons [40–45]. The here considered

planar symmetric and asymmetric model systems and their difference in the interaction with left- and right-circularly polarized laser fields are an essential precursor for that.

The paper is organized as follows: Section II provides a detailed description of the model systems utilized (Sec. II A), and the numerical methods employed for solving the TDSE (Sec. II B), setting up the classical trajectory calculations (Sec. II C), and calculating the SFA spectra (Sec. II D). The results are presented in Section III for fixed-in-space molecules, and Section IV considering randomly arranged model molecules. In these section, we discuss the influence of the long-range character and the excited states by tuning the range, the internuclear distance and the (a)symmetry of the nuclear charge environment, as described above. The paper ends with a discussion and conclusion in Section V.

II. NUMERICAL METHODS

In this section, we present the basic features of our triatomic model system, interacting with an intense circularly polarized laser pulse. To describe the ionization dynamics, we numerically solve the TDSE, which gives access to the time-dependent electronic density and the PEMD. Generally, these PEMDs are very complex and difficult to analyze. In order to reveal the underlying physics, we apply two additional methods: CTMC and SFA. A detailed description of all three methods employed in this work is summarized in this section.

A. The non co-linear triatomic model system

Our numerical model system consists of a single active electron with two spatial degrees of freedom $\mathbf{r} = (x, y)$ and three nuclei with fixed positions at $\mathbf{R}_1$, $\mathbf{R}_2$ and $\mathbf{R}_3$. The model potential $V(\mathbf{r})$ itself includes screened Coulomb attraction V_{en} between the three nuclei and the electron, as well as the bare Coulomb repulsion between the nuclei V_{nn} (atomic units are used unless stated otherwise):

$$V(\mathbf{r}) = V_{en}(\mathbf{r}) + V_{nn} = -\sum_{i=1}^{3} \frac{Z_i \exp\left(-\beta|\mathbf{r}-\mathbf{R}_i|^2\right)}{\sqrt{\left|\mathbf{r}-\mathbf{R}_i\right|^2 + \alpha}} + \sum_{i>j}^{3} \frac{Z_i Z_j}{|\mathbf{R}_i - \mathbf{R}_j|}. \tag{1}$$

The positions of the nuclei are chosen to create different equilateral triangles. The internuclear distances between the adjacent nuclei are varied between $R_{ij} = 3.5$ and 5.5 a.u.,

mimicking the effect of nuclear motion (vibration). These structural changes of our triatomic system strongly affect its ionization dynamics. By changing the nuclear charges Z_i, we are able to simulate either symmetric or asymmetric molecular configurations. Setting all nuclear charges to the same value ($Z_1 = Z_2 = Z_3$), we reduce the complexity of our system by introducing a mirror plane into our system, with the mirror plane lying along the y axis. The classical center of charge (between the point charges Z_n) resides at the origin of the coordinate system (no permanent dipole for the symmetric configuration). Please note that for the asymmetric case, where all charges differ, a small permanent dipole $\boldsymbol{\mu}$ remains. In order to investigate the influence of the excited states and long-range Coulomb effects, we change the range of the potential by utilizing different short-range parameters β, while keeping the softening parameter fixed at $\alpha = 1$. Changing β allows to gradually switch between short- and long-range interaction. Please remember that for short range potentials, the number of bound states is finite. The parametrization is such that the ionization potential I_p is *identical* for all cases, in order to keep the same regime of strong-field ionization. We chose $I_p = 8.64$ eV, a value typical for molecules. The parameters for the different model systems are listed in table I.

model	R_{ij} (a.u.)	Z_1	Z_2	Z_3	I_{p1} (eV)	I_{p2} (eV)	I_{p3} (eV)	β ($\alpha = 1$)
$V_{sym,short}$	3.5	0.882	0.882	0.882	8.64	3.42	3.42	0.3
$V_{sym,short}$	5.5	1.156	1.156	1.156	8.64	7.59	7.59	0.3
$V_{sym,long}$	3.5	0.340	0.340	0.340	8.64	4.78	4.78	0.0
$V_{sym,long}$	5.5	0.413	0.413	0.413	8.64	6.16	6.16	0.0
$V_{asym,long}$	3.5	0.230	0.320	0.457	8.64	4.88	4.47	0.0
$V_{asym,short}$	3.5	0.612	0.862	1.029	8.64	3.91	1.62	0.3

TABLE I. Parameters for the different symmetric (V_{sym}) and asymmetric model (V_{asym}) potentials. Listed are the internuclear distances R_{ij}, the charges of the nuclei Z_i, the ionization potential of the ground state I_{p1} and the first two electronically excited states I_{p2}, I_{p3}, and the softening parameters α and β (see eq.1).

The system interacts with an intense, few-cycle, circularly polarized electric field $\mathbf{E}(t)$, defined via the corresponding vector potentials $\mathbf{A}(t)$ as

$$A_x(t) = \pm\frac{E_0}{\omega} f(t-t_0)\sin\big[\omega(t-t_0) - \phi_{CEP}\big] \tag{2}$$

$$A_y(t) = -\frac{E_0}{\omega} f(t-t_0)\cos\big[\omega(t-t_0) - \phi_{CEP}\big]. \tag{3}$$

with E_0 the laser field strength ($E_0 = 0.02$, if not stated otherwise), ω the laser frequency, ϕ_{CEP} ($\phi_{CEP} = 0$, if not stated otherwise) the carrier-envelope phase (CEP), t_p the full with half maximum of the pulse, and t_0 the time when the Gaussian envelope $f(t)$ reaches its maximum. The positive and negative sign describes right (RCP) and left (LCP) polarized fields, respectively. The dynamics is governed by the time-dependent Schrödinger equation (TDSE) in velocity gauge

$$\mathrm{i}\frac{\partial}{\partial t}\,\psi(\mathbf{r},t) = \left[-\frac{1}{2}\boldsymbol{\nabla}^2 + V(\mathbf{r}) + \mathbf{p}\cdot\mathbf{A}(t)\right]\psi(\mathbf{r},t). \tag{4}$$

By solving the TDSE, we extract the time-dependent electronic density $|\psi(\mathbf{r},t)|^2$ and consequently the final momenta of the ejected electrons (PEMD). The TDSE is solved numerically as detailed in what follows.

B. Numerical solution of the time-dependent Schrödinger equation

We numerically integrate the TDSE (eq. 4) as described in our recent work [39, 46]. Shortly, the propagation is on a two dimensional grid with a time step of 0.001 fs using the split-operator technique [47] and the FFTW3 library [48]. Our two-dimensional grid consists of 512×512 points and ranges from $[-r_{max} : r_{max}]$ along each axis with r_{max}=220 a.u. The electronic eigenstates ϕ_n are calculated via imaginary time propagation [49]. The initial wavefunction was chosen to be the ground state ϕ_1. The photoelectron spectra are obtained by the wave function splitting method [50, 51]. We apply an mask function

$$c(\mathbf{r}) = [1 + \mathrm{e}^{(|x|-x_{max}/1.3)}/\delta]^{-1}[1 + \mathrm{e}^{(|y|-y_{max}/1.3)}/\delta]^{-1}, \tag{5}$$

to split the wavefunction $\psi(\mathbf{r},t)$ into an inner $\psi_{in}(\mathbf{r},t) = c(\mathbf{r})\psi(\mathbf{r},t)$ and an outer part $\psi_{out}(\mathbf{r},t) = [1 - c(\mathbf{r})]\psi(\mathbf{r},t)$. The propagation of $\psi_{in}(\mathbf{r},t)$ is performed with the full Hamiltonian, while the outer part evolves in the asymptotic region far away from the nuclei with the Hamiltonian $H_{out} = T + \mathbf{pA} + V_{nn}$, neglecting the nuclear-electron attraction term V_{en}.

For each time step, we Fourier-transform ψ_{out} into momentum space and coherently add this part to the wavefunction which was already absorbed before. The photoelectron momentum distribution (PEMD) σ is obtained by calculating the absolute squared of the collected outgoing wavefunction at a certain time $T \to \infty$, when the norm of inner wavefunction remains constant

$$\sigma(\boldsymbol{p}) = |\psi_{out}(\boldsymbol{p}, t = T)|^2. \tag{6}$$

Depending on the pulse duration and the wavelength of the electric field, T takes values between 60 and 100 fs. The asymmetries of the spectra, $a(\boldsymbol{p})$, are calculated via the differences of the PEMDs induced by left and right circularly polarized electric fields

$$a(\boldsymbol{p}) = [\sigma^{LCP}(\boldsymbol{p}) - \sigma^{RCP}(\boldsymbol{p})]/\epsilon, \tag{7}$$

where ϵ was defined as the maximum of all σ^{LCP} and σ^{RCP} values.

C. Classical trajectory Monte Carlo method

In order to describe the post-ionization dynamics via classical trajectories, we utilize the classical trajectory Monte Carlo (CTMC) method with the initial conditions according to the tunnel ionization conditions. At each time step t_i, an ensemble of classical trajectories is released at the classical tunnel exits with randomly chosen initial momenta $\boldsymbol{p} = (p_\parallel, p_\perp)$. Depending on the ionization rate Γ, we release up to 1000 trajectories (when Γ reaches its absolute maximum) at each time step t_i. For Γ we evoke the expression for the tunnel rate from the recent review by Popruzhenko [52], which includes the dependence of the Keldysh parameter γ in the exponential term:

$$\Gamma \propto \mathrm{e}^{-2K_0 f_k(\gamma)}, \tag{8}$$

with $K_0 = I_{p1}/\omega$ representing the number of photons required for ionization, and the so-called Keldysh function $f_k(\gamma)$ given by

$$f_k(\gamma) = \left(1 + \frac{1}{2\gamma^2}\right) \mathrm{arcsinh}(\gamma) - \frac{\sqrt{1+\gamma^2}}{2\gamma}. \tag{9}$$

In contrast to atoms, in molecules the tunnel barrier widths are not spherical symmetric, and, consequently, the ionization is spatially anisotropic. In order to account for this ionization anisotropy, we explicitly calculate at every time step t_i the Keldysh parameter γ via the numerically obtained widths of the tunnel barriers b_0

$$\gamma = \frac{b_0\omega}{v_{at}} = \frac{b_0\omega}{\sqrt{2I_{p1}}}. \tag{10}$$

The tunnel barrier widths b_0 are obtained numerically at every time step t_i by solving the equation

$$V(\mathbf{r}) + \mathbf{r}\mathbf{E}(t_i) + I_{p1} = 0 \tag{11}$$

via the Newton-Raphson method. The width of the tunnel barrier b_0 is then the difference between the two zero points $\boldsymbol{r}_{out}$ and $\boldsymbol{r}_{in}$ (see, e.g., Fig. 1 C), in which $\boldsymbol{r}_{out}$ ($|\boldsymbol{r}_{out}| \geq |\boldsymbol{r}_{in}|$) represents the tunnel exit.

For the triatomic symmetric short-range model system with a large internuclear distance of $R_{ij} = 5.5$ a.u., the three nuclei are well separated from each other. Each of the nuclei can be approximately considered as an independent atom with a separate permanent dipole moment of $\boldsymbol{\mu} = \pm R_S$:

$$R_S = \pm\sqrt{R_{1x}^2 + R_{1y}^2} \approx \sqrt{R_{2x}^2 + R_{2y}^2} \approx \sqrt{R_{3x}^2 + R_{3y}^2}. \tag{12}$$

The sign of R_S depends on whether the considered nuclei, from which the ionization process take place, is located at the "up-field" ($R_S < 0, E_r < 0$) or the "down-field" site ($R_S > 0, E_r < 0$) of the electric field. For both cases, we calculate tunnel barriers b_0 and tunnel exits $\boldsymbol{r}_{out}$ via two separate formulas in polar coordinates with $(x, y) = (\boldsymbol{r}\cos\zeta, \boldsymbol{r}\sin\zeta)$. For the down-field core (eq. 13 and Fig. 1 B), we describe the ionization via the Stark-shifted (energy shift: $+R_S \cdot E_r < 0$) ground state

$$V(\boldsymbol{r}) + I_{p1} + \boldsymbol{r} - R_S) \cdot (E_x\cos\zeta(t_i) + E_y\sin\zeta(t_i)) = 0 \tag{13}$$

$$V(r) + \boldsymbol{r} \cdot E_r(\zeta(t_i)) = -I_{p1} + R_S \cdot E_r(\zeta(t_i)) \tag{14}$$

$$= -I_{st,down} \tag{15}$$

while for the up-field core (eq. 16 and Fig. 1 A) case, the ionization occurs from the Stark-shifted (energy shift: $-R_S \cdot E_r > 0$) first electronic excited state with the corresponding ionization potential I_{p2} (table I).

$$V(r) + I_{p2} + \boldsymbol{r} \cdot E_r(\zeta(t_i)) = -I_{p2} - R_S \cdot E_r(\zeta(t_i)) \tag{16}$$

$$= -I_{st,up} \tag{17}$$

For the asymmetric potentials, the system features a permanent dipole moment $\boldsymbol{\mu}$. Here, too, we include the dipole $\boldsymbol{\mu}$ of the electronic ground state via the Stark-shift and calculate b_0 and $\boldsymbol{r}_{out}$ via expression 18.

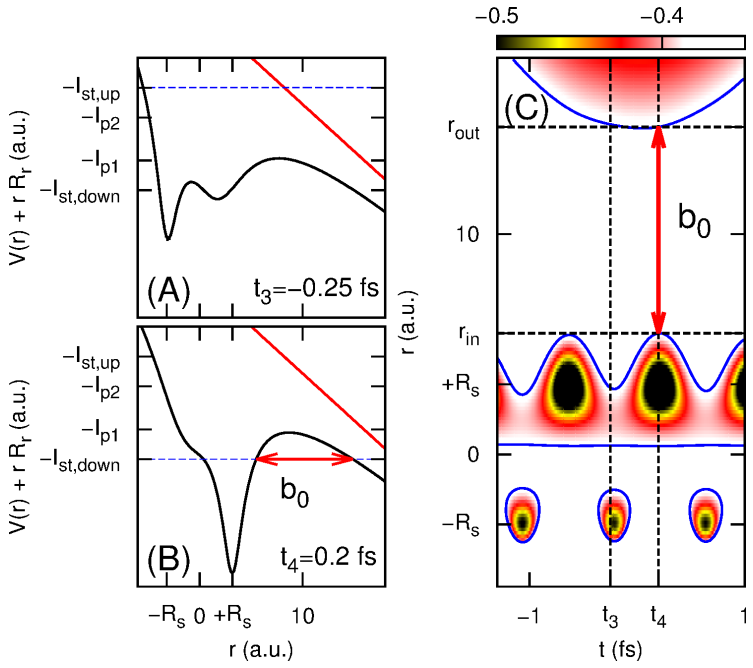

FIG. 1. Schematic representation of the initial conditions in the CTMC model. Shown is the field-dressed Coulomb potential $V(\boldsymbol{r}, t(\zeta)) + \boldsymbol{r}E_r$ (in atomic units) for the symmetric model with an internuclear distance $R_{ij} = 5.5$ a.u. (panel C) and two slices $V(\boldsymbol{r}, t_i(\zeta)) + rE_r$ at different times $t_i = -0.25$ and 0.2 fs, where the ionization mechanism differs: ionization from (A) $(-R_S)$ "up field" or (B) "down field" $(+R_S)$ of the electric field E (solid red line). The corresponding ionization potentials of the Stark-shifted ground (I_{p1}) and excited state (I_{p2}) $-I_{st,down}$ and $-I_{st,up}$ are indicated by blue dashed lines [eqs. (13) and (16)].

$$V(r) + \mathbf{r}\mathbf{E}(t_i) = -I_{p1} + \boldsymbol{\mu}\mathbf{E}(t_i) = -I_{p1} + \langle\phi_1|\mathbf{r}|\phi_1\rangle\mathbf{E}(t_i) \tag{18}$$

For the initial momenta, we employ the Delone-Krainov expressions [53], with the width of the initial parallel momentum $p_\parallel = 0$ and the initial transverse momentum $p_\perp$

$$\sigma_\perp = \sqrt{\frac{\omega}{2\gamma_s}}. \tag{19}$$

For the momenta, we utilize the "standard" Keldysh-parameter

$$\gamma_s = \frac{\omega\sqrt{2I_p}}{E}, \tag{20}$$

without explicitly including b_0. We note that the results calculated via $\sigma_\perp$ with the two different Keldysh parameters γ and γ_s do not differ significantly.

For the multi-photon case ($\gamma = 2.27$ for $\lambda = 800$ nm), we shift the center of the Gaussian $p_\perp$ by $p_0 = \pm 0.22$ a.u., (with the + sign for LCP, and the − sign for RCP pulses) corresponding to the excess energy, which the electron will acquire in the above-threshold ionization case. For the simulations in the tunnel regime with a corresponding laser wavelength of 3000 nm ($\gamma = 0.61$), the center of the initial Gaussian distribution in momentum space is located around $p_0 = 0$ a.u.

To generate random numbers following the Gaussian distribution specified above for the initial momenta $p_\perp$ of the trajectories, we convert uniformly distributed random numbers (RAN2) by a Box-Muller transform [54], multiply the numbers with $\sigma_\perp$ and add p_0.

For the triatomic Coulomb model system with a large internuclear distance of R_{ij} =5.5 au, we reach the over-the-barrier (OBI) regime. Here, we choose the starting point $\boldsymbol{r}_{out}$ of the trajectories at the maximum $V_{max}(\boldsymbol{r}, t_i)$ of the tunnel barriers at each time step t_i and add an additional initial parallel momentum $p_\parallel(t_i)$ via

$$p_\parallel(t_i) = \sqrt{2[-I_{st,up}(t_i) - V_{max}(t_i)]}. \tag{21}$$

As described before, ionization takes place from the Stark-shifted first excited state with ionization potential I_{p2}. The dynamics of the released trajectories is governed by Newton's equations of motion

$$\mathbf{p} = \frac{\partial \mathbf{r}}{\partial t} \tag{22}$$

$$\frac{\partial \mathbf{p}}{\partial t} = -\nabla_{\mathbf{r}}[V(\mathbf{r}) + \mathbf{r}\mathbf{E}(t)], \tag{23}$$

with the trajectories describing the dynamics of the ionized part of the wavefunction. Typically 10^6 trajectories are propagated by numerically integrating the Newton equations (eqs. 23) by a Runge-Kutta algorithm of fourth order with adaptive step-size control. The PEMDs are obtained from the final momenta $\boldsymbol{p}(T)$. The analysis of the trajectories enables us to study the dynamics of the liberated electrons. We can artificially switch on and off the Coulomb continuum and examine its influence the courses of the ejected electrons.

D. Photoelectron momentum distribution within the (extended) strong-field approximation

The SFA presents an analytical way to strong-field effects and calculate PEMDs, under the assumption that the molecular potential $V(\mathbf{r})$ in the Hamiltonian is a small perturbation and can be neglected. The physical meaning is the following: before ionization, the molecular system in its ground state $\phi_1(\tau)$, acquiring a phase up to time τ, determined by the molecular potential only with $I_{p1} = 8.64$ eV

$$\psi_i(\mathbf{r}, \tau) = \mathrm{e}^{\mathrm{i}I_{p1}\tau}\phi_1(\mathbf{r}). \tag{24}$$

After ionization at time τ, the electron is solely driven by the electric field, without the influence of the molecular potential. Ionization is described as the transition from the initial state $\psi_i(\tau)$ to the final state – the Volkov state $\psi_V(\tau)$, a plane wave with momentum $\mathbf{p} + \mathbf{A}$. The PEMD σ_{SFA} (length gauge) is given by the absolute squared of the transition amplitude

$$\begin{aligned} \sigma_{SFA}(\mathbf{p}) &= \left| -i \int_{-\infty}^{\infty} \mathrm{d}\tau \, \langle \psi_V(\tau) | \mathbf{r}\mathbf{E}(\tau) | \psi_i(\tau) \rangle \right|^2 \\ &\propto \left| -i \int_{-\infty}^{\infty} \mathrm{d}\tau \, \langle \mathbf{p} + \mathbf{A}(\tau) | \mathbf{r}\mathbf{E}(\tau) | \psi_i(\tau) \rangle \, \mathrm{e}^{iS(\tau)} \right|^2 . \end{aligned} \tag{25}$$

The action $S(\tau)$ is given by

$$S(\tau) = \frac{1}{2}\int_{-\infty}^{\tau} \mathrm{d}t' \, (\mathbf{p} + \mathbf{A}(t'))^2. \tag{26}$$

We integrate eq. 25 numerically to obtain the PEMD. For each time τ, we calculate first

$$A_p(\tau) = \mathrm{e}^{-\mathrm{i}\mathbf{A}(\tau)\mathbf{r}} \, \mathbf{r}\mathbf{E}(\tau) \, \psi_i(\mathbf{r}, \tau), \tag{27}$$

Fourier transform this expression into momentum space by using the FFTW3-library [48], and multiply the result by the action $\mathrm{e}^{iS(\tau)}$. Subsequently, we sum over the transition amplitudes for each time step τ, multiply by $-i\mathrm{d}\tau$ and calculate the absolute squared to obtain the final PEMD σ_{SFA}.

Due to the lack of gauge invariance of the SFA [19, 20, 55], the predictions of SFA results in length or velocity gauge may differ substantially, see e.g. [56]. We thus also apply the SFA in velocity gauge, where the expression for the spectra takes the following form [57]:

$$\sigma_{SFA,VG}(\mathbf{p}) \propto \left| -i \int_{-\infty}^{\infty} \mathrm{d}\tau \, \langle \mathbf{p} | \mathbf{p}\mathbf{A}(\tau) | \psi_i(\tau) \rangle \, \mathrm{e}^{iS(\tau)} \right|^2 . \tag{28}$$

Here, we extend the SFA to incorporate the dynamics of the first two excited states ϕ_2 and ϕ_3 with ionization potentials of I_{p2} and I_{p3} (table I), similarly as proposed by Becker et al. [58]. We extract the coefficients $c_n(\tau) = \langle \phi_n | \psi(\tau) \rangle$ from the numerically calculated wavefunction $\psi(\boldsymbol{r}, \tau)$ of the TDSE simulation. The initial state $\psi_i(\tau)$, from which the ionization takes place, is defined as the time-dependent superposition of the three eigenstates ϕ_1, ϕ_2 and ϕ_3.

$$\psi_i(\boldsymbol{r}, \tau) = \sum_{n=1}^{3} c_n(\tau) \phi_n(\mathbf{r}) \tag{29}$$

By including the excited states in the SFA, we aim at analyzing the influence of the excited states, by changing the initial wavefunction (eq. 24 vs. eq. 29). As the final states are Volkov states, the influence of the (long-range) continuum is switched off.

III. NUMERICAL RESULTS: FIXED-IN-SPACE MOLECULES

In order to understand the ionization dynamics of our complex triatomic model systems, as a first step, we first reduce the complexity and consider initially only symmetric short-

range potentials, excluding long-range contributions and excited states. We then consider the much more complex Coulombic potentials.

In many experiments, the molecules are not aligned with respect to the laser field. Consequently, each molecular orientation of the molecule contributes to the final PEMD. We therefore calculate PEMDs for many different molecular configuration of our triatomic model systems in order to understand their exact influence on the final PEMD.

A. Symmetric short-range potentials: Ionization dynamics and the role of excited states

We first solve the TDSE numerically for a short-range model V_{short} with an internuclear distance $R_{ij} = 3.5$ a.u., interacting with a laser pulse of $t_p = 5$ fs FWHM, field strength $E_0 = 0.02$ a.u. (corresponding to an intensity of 1.4×10^{13} W/cm^2) and wavelength $\lambda = 800$ nm. In Fig. 2, we present a snapshot of the electronic density $|\psi(\boldsymbol{r}, t)|^2$ at $t = 3.5$ fs and the resulting PEMD. The snapshot of the electronic density clearly shows, how a three-folded structure is built up during the course of ionization, leading finally to a PEMD with a pronounced three-folded pattern. To analyze the shape of the spectra, we used the CTMC model, with the tunnel exits, initial momenta and ionization rate Γ as described in section II C, see Fig. 2. The comparison between the PEMDs obtained by the CTMC method (panel D1) and the TDSE (panel E) shows, that the CTMC reproduces the TDSE results very well, for both, peak positions and the intensity profile of the peaks. We thus can proceed to the analysis of the trajectory picture.

Γ shows three distinct maxima at times t_n, panel (A), when the simulated tunnel barriers b_0 are the most narrow (blue dashed lines in Fig. 2 B). These three times t_1, t_2 and t_3 can be assigned to three temporally well separated ionization events, near the nuclei Z_2, Z_3 and Z_1. For each ionization event, we depict one representative trajectory with the most probable initial momentum $\boldsymbol{p} = (p_\perp, p_\parallel)$ of either $\boldsymbol{p} = (0, 0)$ or $\boldsymbol{p} = (0.22, 0)$ in coordinate (panel (C): red and black lines) and momentum space (D1 and D2). To compare the 2D-snapshot of the electronic density with the trajectories in coordinate space, we marked the current position of the electrons at time $t = 3.5$ fs along the trajectories with stars. From that we can see that the trajectories with an initial momentum of $p_\perp = 0.22$ a.u. (panel C: black stars) lead leads to a faster evolution of the electrons, in better agreement with the electronic density

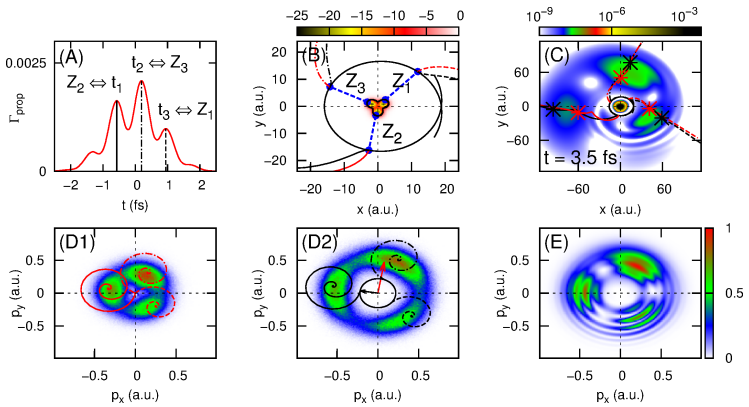

FIG. 2. Overview over the results obtained by the TDSE and CTMC simulations for the symmetric short-range model. Pulse parameters: pulse length $t_p = 5$ fs FWHM, field strength $E_0 = 0.02$ a.u. (corresponding to an intensity of 1.4×10^{13} W/cm^2) and wavelength $\lambda = 800$ nm. (A) The ionization rate Γ, eq. 8. (B) At three times t_i marked in panel (A), representative trajectories are launched at the classical tunnel exits (black dots). The corresponding widths of the tunnel barriers are indicated by the blue dashed lines. The color bar represents the potential in eV. (C) Comparison of the TDSE and CTMC results. The three selected trajectories are overlaid with a snapshot of the electron density $|\psi(\boldsymbol{r}, t)|^2$, with the stars are indicating the current position of the electrons along this trajectories at the same time $t = 3.5$ fs. The color bar represents the value of the electron density in atomic units. (D, E) PEMDs, with (D1, D2) obtained from CTMC calculations with different initial momenta $\boldsymbol{p}$=($p_\perp$,$p_\parallel$) = $(0, 0)$ (D1), and $\boldsymbol{p} = (0.22, 0)$ (D2), and (E) the corresponding TDSE result. The color bar represents the (normalized) spectral intensity.

of the TDSE simulation, as to be expected for a regime with predominantly multi-photon ionization character (the initial momentum of $p_\perp = 0.22$ a.u. corresponds approximately to the excess energy the electron acquires in the above-threshold ionization regime) [39]. In the PEMD (panels D2 and E), the peak with the highest intensity is located in the first quadrant with positive momenta in p_x and p_y. The trajectory analysis reveals that this corresponds to the strongest ionization to occur near nucleus Z_3, exactly at the time when the envelope of the electric field is close to its maximal field strength E_0. The intensity profile of the PEMDs strongly depends on the carrier-envelope phase ϕ_{CEP} of the electric field, as will be discussed in section IV. We note parenthetically, that the standard SFA is able to reproduce the PEMD qualitatively correctly, (see Fig. 5 (A1)), as will be discussed

in the next subsection.

1. *Larger internuclear distances*

Next, we examine the influence of the internuclear distance. We apply the same procedure as described above and present PEMDs, snapshots of the electronic density at selected times t and classical trajectories for a short-range potential with an internuclear distance $R_{ij} = 5.5$ a.u. in Fig. 3. Surprisingly, the three-folded shape of the PEMD, Fig. 3 (E), for the model system with larger $R_{ij} = 5.5$ a.u. shows a completely different behavior than for the case $R_{ij} = 3.5$ a.u. (panel D): the relative position of the peaks is rotated by almost 60° and the intensity profile has completely changed; the most intense peak of the spectrum is now located in the third quadrant, with negative p_x and p_y. This pronounced rotation can be gathered from the electronic density snapshots, panels (A) and (B), as well.

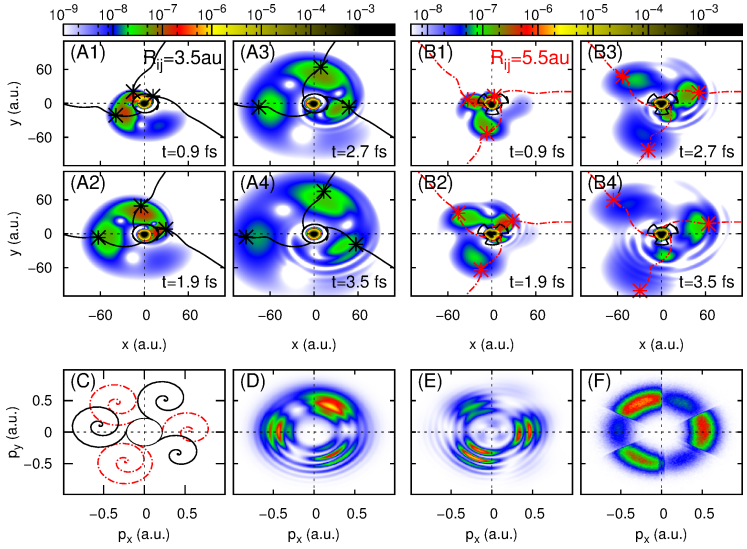

FIG. 3. Influence of the internuclear distance: (A,B) snapshots $|\psi(\boldsymbol{r},t)|^2$ for $R_{ij} = 3.5$ a.u. (A1-A4) $R_{ij} = 5.5$ a.u. (B1-B4). The color bar represents the value of the electron density in atomic units. Three representative trajectories are shown for different ionization times using an initial momentum of $\vec{p}$=($p_\perp$,$p_\parallel$) of $\vec{p_2}$=(0.22,0), [black circle (C)]. The trajectories are displayed in coordinate (A,B) and momentum space (C), with the stars indicating the current position of the electrons at the time t. (D - F) PEMDs for $R_{ij} = 3.5$ a.u. (D), $R_{ij} = 5.5$ a.u. (E) from TDSE, and (F) $R_{ij} = 5.5$ a.u. as obtained from CTMC calculations.

In order to analyze this pronounced difference in the ionization dynamics for larger R_{ij}, we evoke our classical trajectory calculations, with the resulting PEMD depicted in panel (F). The first striking difference can be seen in the ionization rate, Fig. 4 (B): Γ peaks at completely different times than previously for $R_{ij} = 3.5$ a.u. (cf. Fig. 2 (A)). What is the reason for this discrepancy in the ionization rate? Let us examine snapshots of the bound electron wavepacket: Fig. 4 shows that strong localization of the electron density occurs, which is peaked parallel to the direction of the laser field. The reason is a strong mixing of the first bound electronic states in the laser field, which, in turn, is favored for larger R_{ij}, as here the energy gap $\Delta E = I_{p1} - I_{p2}$ is small and a strong population transfer occurs under quasi-resonant conditions, see also the populations in Fig. 5 (C). We would like to stress that this is not an artifact of the model system but rather the typical scenario for stretched molecules: for larger internuclear distances R, the corresponding anti-bonding molecular orbitals are energetically much closer than for smaller R, enabling strong and quasi resonant population transfer between the lowest electronic states (see, e.g. Refs. [59–61]).

As a consequence, in contrast to the previous case of small R, where ionization takes place from the nuclei at the "down-field" site (Fig. 4 B) from the electronic ground state, ionization occurs now for larger R preferentially from the Stark-shifted excited states near the nuclei at the "up-field" site (R_s <0). As energetically higher lying excited states ϕ_2, ϕ_3 are involved, and additionally an energy up-shift due to the field-dressing ($R_s \cdot E_r > 0$) occurs, much narrower tunnel barrier widths b_0 and, consequently, higher ionization rates Γ (Fig. 4 (B), (C), see Γ at times t_1, t_3, t_5) result. Ionization from the "down-field" site (R_s >0), on the other hand, only occurs from the Stark-shifted electronic ground state, with larger b_0 and correspondingly smaller Γ (Fig. 4 (B), (C), see Γ at times t_2, t_4, t_6).

Let us analyze the bound electronic dynamics in more detail. Fig. 4 (A) (and Appendix Fig. 18) display the density of the time-dependent superposition state $|\phi_i(t)\rangle = \sum_{n=1}^{3} \langle \phi_n | \psi(t) \rangle | \phi_n \rangle$ for both model systems with $R_{ij} = 3.5$ and 5.5 a.u.. For both systems, the bound electronic density $|\phi_s(\boldsymbol{r}, t)|^2$ is driven by the field, however the spatial distribution of the electronic densities differs significantly. For $R_{ij} = 5.5$ a.u., the electronic density is mainly located at the nuclei parallel to the field vector (R_S <0, "up-field" site), while for systems with $R_{ij} = 3.5$ a.u., the opposite is the case (R_S >0, anti-parallel to the field vector), as already described above (see Appendix, Fig. 18 (A)). This can be mimicked in the CTMC model by the different initial conditions, where the ionization process starts from the

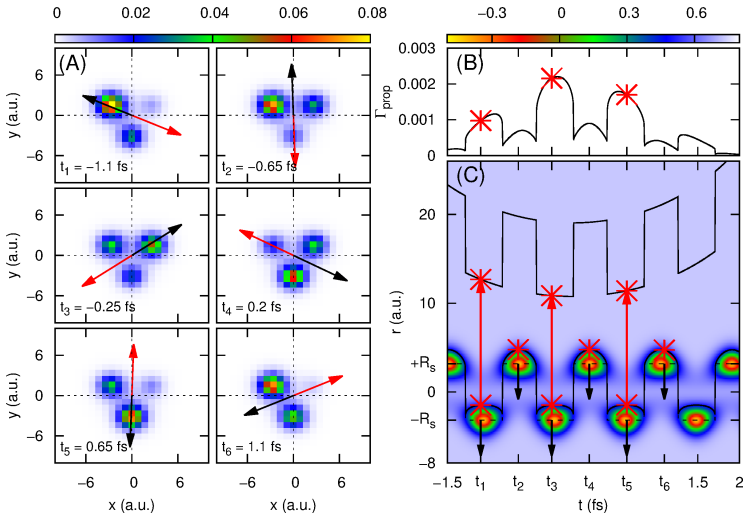

FIG. 4. Bound electron dynamics for the symmetric short range model system with larger $R_{ij} = 5.5$ a.u. (A) Snapshots of the bound electronic density of the superposition state $\phi_i(\boldsymbol{r}, t_i) = \sum_{n=1}^{3} c_n(t_i)\phi_n(\boldsymbol{r})$ with coefficients $c_n(t)$ extracted as described in section II D. Also shown are the characteristic electric field vectors $\mathbf{E}(t_i)$ (black arrows) at these times t_i. Tunneling occurs in the direction indicated by the red arrow. (B) Ionization rate Γ calculated with tunnel barriers b_0 as shown in panel (C). (C) Cuts along the potential $V(\boldsymbol{r}, t(\zeta))$, with ζ depending on the direction of the electric field vector $\mathbf{E}(t)$. The color bar in panel (C) denotes the value of the potential in atomic units.

different nuclei. Depending on the spatial distribution of the electronic density relative to the electric field vector, the ionization occurs either from the "up-" or the "down-field" site, resulting in complete different ionization dynamics and, ultimately, different peak positions in the PEMD. Although the peak positions of the PEMD calculated with the CTMC method Fig. 3 (F) are in good agreement with the quantum dynamical calculations, panel (E), the intensity profile differs. To understand this difference, we come back to the bound population dynamics, Fig. 5 (C-F): As can be seen, the populations $c_n(t)$ of the excited states change as a function of time, and the initial conditions chosen for the CTMC calculations to predominantly ionize from the (field-dressed) excited states overestimate their contributions, since ground state contributions are neglected. These field-driven bound-state dynamics are exactly the reason why the CTMC calculations provide an inaccurate intensity distribution.

Next, we investigate if the SFA can describe the PEMDs properly. We employ two variants

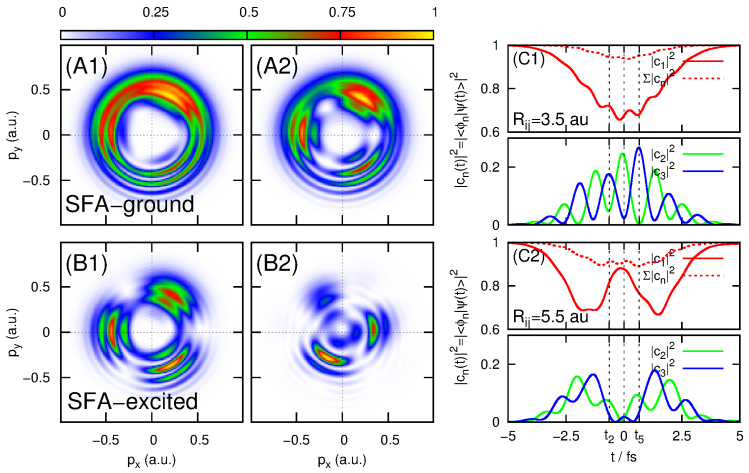

FIG. 5. PEMDs as obtained from the SFA, comparison for $R_{ij} = 3.5$ and 5.5 a.u. (A) Ground state SFA (eq. 24) and (B) excited-state SFA (eq. 29). (A1/B1) $R_{ij} = 3.5$ a.u. (A2/B2) $R_{ij} = 5.5$ a.u.. (C) The populations $|c_1(t)|^2$, $|c_2(t)|^2$, $|c_3(t)|^2$, and $|c_s(t)|^2 = \sum_{n=1}^{3} |c_n(t)|^2$ (dashed lines) are presented for $R_{ij} = 3.5$ a.u. (C1) and $R_{ij} = 5.5$ a.u. (C2).

of SFA, in which the ionization occurs either from the field-free ground state $\phi_1(\boldsymbol{r})$ (eq. 24) or from the time-dependent superposition wavepacket $\phi_s(\boldsymbol{r}, t)$ (eq. 29). The corresponding PEMDs are displayed in Fig.5 (A, B). The PEMDs for the triatomic model with shorter internuclear distance of $R_{ij} = 3.5$ a.u. (panels A1 and B1) show for both variants of the SFA the same three-folded structure discussed above. The position of the three peaks are in good agreement with TDSE calculations (see Fig. 3 D), with small deviations in the intensity pattern mainly due to an incomplete basis for the description of the initial wave function. We note that, that the influence of the third excited state is negligible with its population $|c_4|^2$ being in the order of magnitude of 10^{-7}. Hence, the main missing contribution is *transient* population of continuum states (panel (C), dashed lines, the difference between the sum of populated states, $|c_n(t)|^2$ and unity).

For the model potential with $R_{ij} = 5.5$ a.u., the differences between the PEMDs (Fig. 5, A2, B2) obtained by the two SFA approaches are striking. For larger internuclear distances, the standard SFA completely fails to describe the correct position and intensity pattern of the TDSE simulation (cf. Fig. 3 (E)) and Ref. [58]), while the "excited-state SFA" is able to reproduce all significant features. Here, too, the small deviations in the intensity pattern of the peaks in the PEMDs are due to an incomplete basis of the initial wavefunction $\psi_i(\boldsymbol{r}, t)$.

As can be seen from the population dynamics displayed in Fig. 5 (C2) (dashed lines), there is more, transient population in the continuum for larger R compared to small R.

Overall, the PEMD for the short-range potential with $R_{ij} = 3.5$ a.u. obtained by SFA, CTMC and TDSE calculations are in good qualitative (peak position and relative peak intensities) agreement to each other. The classical trajectories show clearly, from which nuclei the ionization originates and how the released photoelectrons move in the continuum. Increasing the internuclear distance to $R_{ij} = 5.5$ a.u. leads to a strongly modified PEMD, in which the peaks of the three-folded structure are rotated by about 60°. By including the influence of the first excited electronic states in the CTMC or SFA methods, this 60° shift could be reproduced. A more detailed analysis shows that the bound state dynamics of both model systems with $R_{ij} = 3.5$ and 5.5 a.u. is different, as for larger R the contribution of excited states is much stronger, leading to a different localization dynamics, and, in turn, the ionization dynamics to originate from different nuclei at the "up-" (including excited states) or "down-field" site (ground state only) of the electric field vector.

At this point, it should be discussed whether this difference in the ionization behavior is related to enhanced ionization (or charge-resonance enhanced ionization, CREI) [24]. First, we would like to remind that, in contrast to real molecules, we have fixed the ionization potential to 8.64 eV for both, the shorter and elongated geometry. Still, when comparing the total ionization yield for these two geometries, $R_{ij} = 3.5$ and 5.5 a.u., we find that ionization is substantially increased for the elongated internuclear distances, approximately by a factor 6. This can be well explained by the increased contribution of the (field-dressed) excited electronic state, as discussed above. However, in contrast to the standard CREI picture, the field-dressed excited state is still below the internuclear barrier. Thus, it is not CREI we observe here but rather resonance-enhanced multi-photon ionization.

B. Symmetric Coulomb potentials: Distinguishing contributions from excited states and other long-range contributions

The short-range model discussed in the previous section represents the simplest system, as no Coulomb effects influence the ionization dynamics. The aim of this section is to investigate these contributions. We therefore repeated our calculations for V_{long} (table I). An overview of all results is depicted in Figs. 6 and 7.

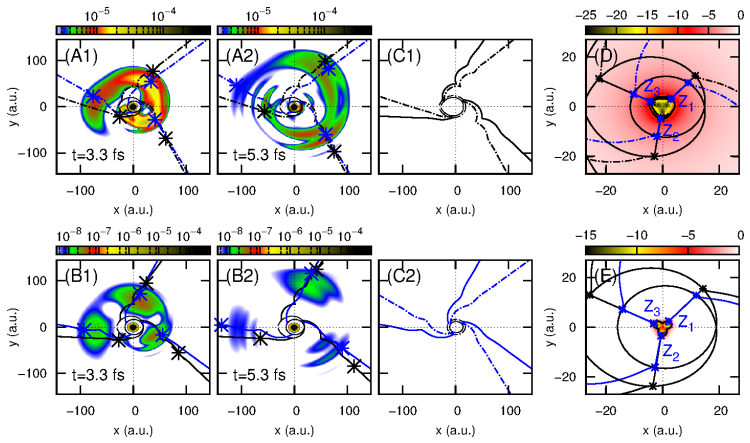

FIG. 6. Imprint of the long-rage character on the dynamics. Snapshots $|\psi(\boldsymbol{r},t)|^2$ at different times for the Coulomb (A1/A2) and the short (B1/B2) range potentials. (C) Selected trajectories. The potentials and the tunnel exits (black circle) with the corresponding barrier widths b_0 (straight lines) are depicted in panels (D) for the Coulomb and (E) the short-range potential. The color bar represents the potential in eV. For each model system (short-range: solid lines, Coulomb: dashed lines) six trajectories (B/C: three black and three blue lines) with identical initial momentum are chosen, with the stars indicating the current position of the electrons along this trajectory.

We first compare the electron density for the short- and long-range cases. The snapshots of the electronic density for the long-range case (Fig. 6 A) feature the same evolution of the three-folded pattern as for the short-range simulation (Fig. 6 B). However, the three-fold shape is less pronounced, and the corresponding peaks in the PEMDs feature an additional clockwise rotational shift. The peaks also show significant differences in their intensity profiles: The most intense peak is now located in the second quadrant, near $\boldsymbol{p} = (0.2, -0.4)$ in the PEMD (Fig. 7 A). Additionally to the clockwise rotated peaks, we also observe a finger-like structure with small momenta in the PEMD, which is a result of transitions from energetically higher lying electronic states (Rydberg series) and can, consequently, not be found in short-range simulations [62]. Ionization from these excited states does not require high field strengths since their binding energy is relatively small. Thus, ionization of these states can occur at later times when the pulse is relatively weak. We note, that the overall ionization probability is significantly higher for the long-range simulation due to the presence of (infinitely) many excited states, which increase the contribution of (resonant)

multi-photon ionization [63, 64].

We start our analysis of strong-field ionization for Coulomb potentials with the trajectory model. In Fig. 6, we display six representative trajectories for each model system at three different ionization events related to the position near the three nuclei. All six trajectories are released at different times t_i and only differ by their initial position in space - the tunnel exit: We emphasize that the tunnel exits (panels C - E) for the short (D) and Coulomb-type (E) potentials differ significantly: the tunnel exits are at smaller radii $\boldsymbol{r}$ for Coulomb potentials compared to the short-range potentials. Consequently, the width of the tunnel barrier differs, and thus the ionization rate. The trajectories (Fig. 6 C) feature the same characteristics as the long-range quantum dynamics: the deceleration of the electrons and the clockwise rotation.

To investigate how the PEMD is affected by the long-range contributions, we calculated the kinetic energy E_{kin} via $p_r(\phi)^2/2$ as function of the polar angle ϕ. In comparison to the short-range case, the peaks in the E_{kin}-spectra of the Coulomb model V_{long} are shifted to smaller angles and energies. Not surprisingly, the attractive character of the Coulomb continuum does not only lead to a rotation of the triatomic peak structure but also causes a deceleration of the photoelectrons, thus lowering the energy of the ATI-rings. This deceleration can also be gathered in the snapshots (Fig. 6). To further analyze the long-range interaction between the nuclei and the continuum electrons, we applied the CTMC model. We likewise convert the Cartesian momentum $\mathbf{p} = (p_x, p_y)$ of the trajectories to polar coordinates and calculate the corresponding kinetic energy $p_r^2(\phi(t))/2$ (Fig. 7 E, F) as a function of time t. Our trajectory analysis shows that the energetically higher lying ATI-rings are associated with trajectories, which are released near the center of the pulse envelope near t_0, when the electric fields $E(t)$ is strongest, leading, in turn, to higher final momenta. In contrast, trajectories with smaller final E_{kin} are released at times t when electric field strength is relatively low.

Comparison of the final momenta (red crosses) of the trajectories calculated with the short-range (solid lines) and the Coulomb-like (dashed lines) potential shows an energetic shift induced by the long-range interaction. These energetic shifts are most pronounced for the blue trajectories, suggesting that the ATI rings (TDSE simulation) with larger kinetic energy E_{kin} should undergo a stronger shift. This is in contrast to the results obtained by the TDSE simulations (panels E and F). It is not very surprising that the CTMC fails

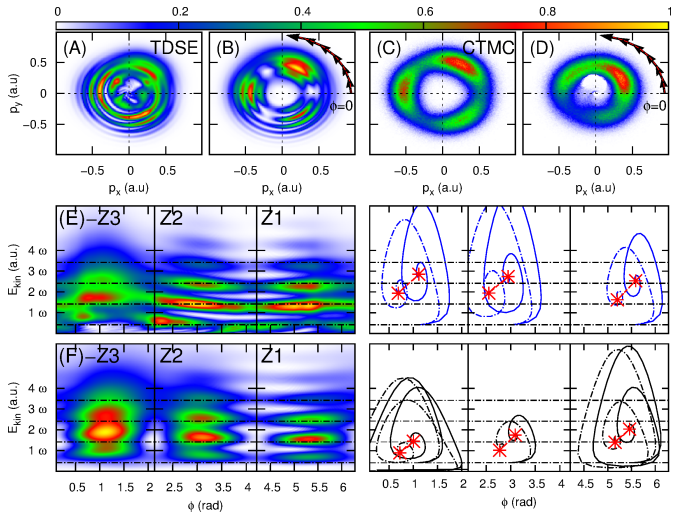

FIG. 7. Imprint of the long-rage character on the PEMDs. Comparison of the PEMDs and energy spectra obtained by TDSE calculations (A, B) with results simulated via the CTMC method (C, D) for two different models. (E, F) Energy spectra obtained by TDSE calculations for the Coulomb (A, E) and short-range (B, F) potential. The energy of six selected trajectories (see Fig. 6) are shown for the short-range (dashed lines) and the Coulomb (solid lines) potential. The red stars indicate the final kinetic energy of the released electrons. The black dashed lines in the energy spectra indicate the energies $E_N = N\hbar\omega + E_i$ of the N absorbed photons, with $E_i = p_\perp^2/2 = 0.024$ a.u.

to describe the correct shift for the ATI-rings with lower energies since the spatial initial conditions of the black trajectories are not optimal, as discussed before. This is in particular important for ionization events at weaker electric fields: here, initial conditions based on the tunneling picture become less suited. The tunnel exits of the resulting (black) trajectories are too large, and the interaction between the photoelectron and the nuclei is underestimated. These trajectories can thus not properly characterize the part of the wavefunction, which evolves slowly in the continuum (related to small final momenta).

In section III A, we have already shown for the short-range potential, that an increased internuclear distance $R_{ij} = 5.5$ a.u. leads to a completely different PEMD with an 60° rotated three-fold structure. A pronounced clockwise rotation can also be seen in PEMD of the Coulomb case (Fig. 8 B), with the difference that the rotation angle is here much smaller ($\approx 30°$). As already suggested by the cut along the potential in panel (E), for the CTMC calculations, we need to employ initial conditions evoking the over-the-barrier ionization

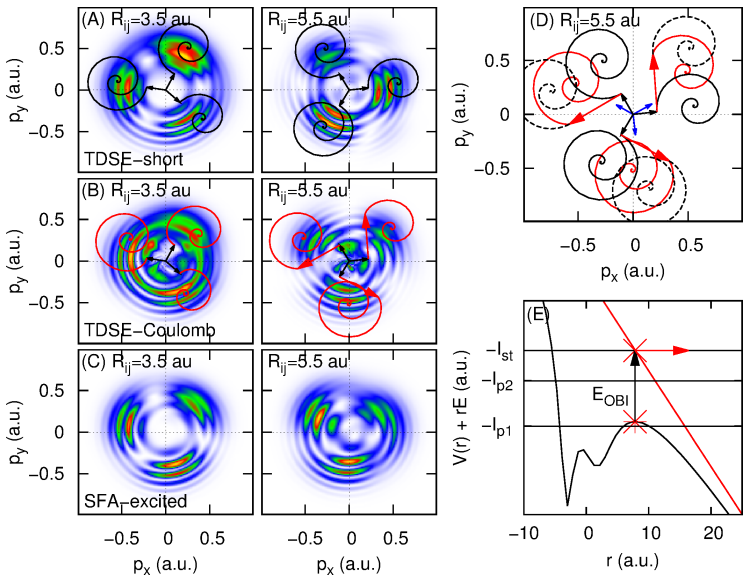

FIG. 8. Direct comparison between the PEMDs calculated for model potentials with different internuclear distance R_{ij}, analyzed by classical trajectories and SFA. Shown are the PEMDs, which are calculated by solving the TDSE for two models: (A) short-range and (B) Coulomb potential. For the SFA (panel (C)), $\psi_i(\boldsymbol{r},t)$ was chosen to be the time-dependent superposition state $\phi_s(\boldsymbol{r},t)$ (eq. 29) of the Coulomb potential. (D) The trajectories are calculated with different initial momenta $\mathbf{p} = (p_\perp, p_\parallel)$, which are presented by the black ($p_\perp$) and red ($p_\parallel$) arrows. For comparison, we also calculated trajectories (black dashed) for the Coulomb model, but with the condition that the Coulomb-interaction is set to zero after the trajectory is released to the continuum. (E) Also presented is a cut of the total potential $V(\boldsymbol{r},t_i)+\mathbf{rE}(t_i)$ [red line: $\mathbf{rE}(t_i)$] at a certain time t_i. The black arrow represents the excess energy $E_{OBI} = p_\parallel^2/2$ (eq.(21)) with the red arrow pointing in direction of $p_\parallel$.

scenario: The initial spatial positions of the trajectories are now located at the maximums of the tunnel barriers, and $p_\parallel$ is linked to the excess energy E_{OBI} (Fig. 8 E). It is this initial parallel momentum $p_\parallel$ (red arrows) which induces an anticlockwise rotation (against electric field), being the most pronounced for the ATI-rings with larger momenta.

The extended SFA is also capable of qualitatively reproducing the PEMDs, see Fig. 8. Depending on the internuclear distance, the triatomic pattern is rotated either clockwise ($R_{ij} = 3.5$ a.u.) or anticlockwise ($R_{ij} = 5.5$ a.u.) with respect to the pattern obtained by the short-range excited-states SFA simulations (cf. Fig. 5). The position of the peaks are in

good agreement with the TDSE calculations (Fig. 8), only the intensity profile differs. The latter is not surprising since the superposition of only three states provides an insufficient description of the initial state. Again, we note, that the clockwise rotation in the Coulomb potential is not only a result of long-range interactions but also due to contribution of excited states.

To summarize this section briefly, the PEMDs for the symmetric triatomic Coulomb potential displays more complex features than the corresponding PEMDs of the short-range model (Sec. III A): a clockwise shifted three-fold pattern, a different intensity profile, and a finger-like structure are additional characteristics of the PEMD. These features can be assigned to the complex excited-state dynamics as well as long-range interaction between the photoelectrons and the nuclei in the continuum. The long-range interaction has been investigated via classical trajectories and the modified SFA. This allowed us revealing the influence of the first two excited states, showing that the shift of the three-fold pattern is not only a result of the long-range interaction. For the case of the Coulomb potential with $R_{ij} = 5.5$ a.u., the OBI-mechanism set in: The initial parallel momentum $p_{\parallel}$ induces an anticlockwise shift of the peaks.

Now, we re-raise the question concerning CREI. Again, although having fixed the ionization potential also of the Coulomb-type potentials to 8.64 eV for both, the shorter and elongated geometry, the total ionization yield of the stretched geometry is again increased by a factor 6. However, in contrast to the short-range case, in these Coulomb-type potentials, the (field-dressed) excited state is now *above* the internuclear barrier. In this sense, this mimics a CREI-type mechanism [24, 59, 65, 66].

C. Asymmetric potentials: Influence of the permanent dipole moment

So far, we have examined symmetric triatomic models with all charges being equal. In this section, we investigate asymmetric model systems and their interaction with intense, left- and right-circularly polarized electric fields. The results and the direct comparison to the corresponding symmetric systems are presented in Figs. 9 - 11.

The few-cycle LCP and RCP fields are chosen such that their evolutions behaves mirror symmetrically to each other. Depending on the polarization of the electric field, the electronic density of the symmetric systems discussed above, evolves either clockwise (LCP) or

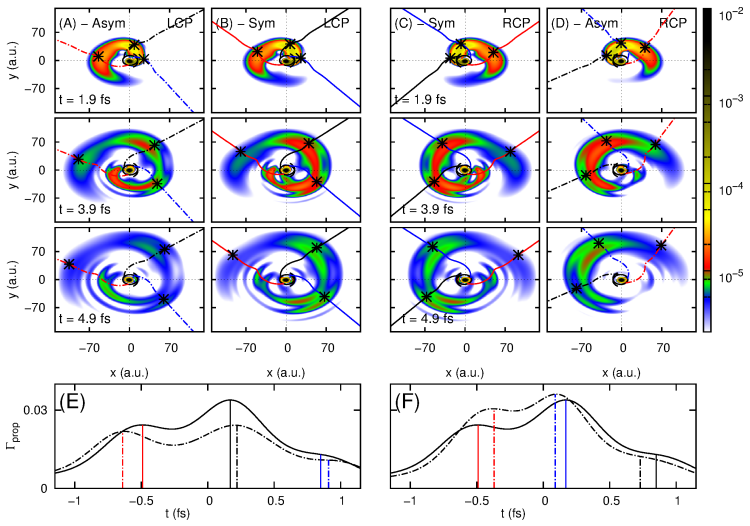

FIG. 9. Ionization dynamics of symmetric (B, C) and asymmetric (A, D) Coulomb potentials, highlighted with representative classical trajectories. Snapshots of the electronic density $|\psi(\boldsymbol{r},t)|^2$ at different times t for the symmetric (sym), panels (B, C), and asymmetric (asym), panels (A, D), potential interacting with LCP (A, B) and RCP (C, D) laser fields. Panels (E) and (F) display the ionization rates Γ for the symmetric (solid lines) and asymmetric (dashed line) potentials. The vertical lines indicate times when Γ reaches a maximum, corresponding to the tunneling times of the trajectories in panels (A–D).

anticlockwise (RCP); the dynamics are at each time t mirror symmetric to each other (Fig. 9 B, C). This mirror symmetry is captured in the PEMDs (Fig. 10 A).

To mimic a asymmetric molecule, the charges Z_i of all nuclei differ (V_{asym} in table I). Breaking the symmetry of our system also destroys the symmetry relation between the electronic dynamics induced by the LCP and RCP fields (Figs. 9 and 10). Consider, for example are the intensities of the peak in the first quadrant of the LCP simulation and the corresponding peak in the fourth quadrant of the RCP simulation (Fig. 9). While the intensity of the first mentioned peak (LCP) increases, the latter one decreases when going to the asymmetric model.

In order to investigate the different dynamics, we evoke classical trajectories, extending the model to including the permanent dipole of the asymmetric model system (see Sec. II C). Remember that the Stark-shift affects the tunnel barriers b_0, the tunnel exits, and the ionization rates Γ. The ionization rate Γ and representative trajectories in coordinate space

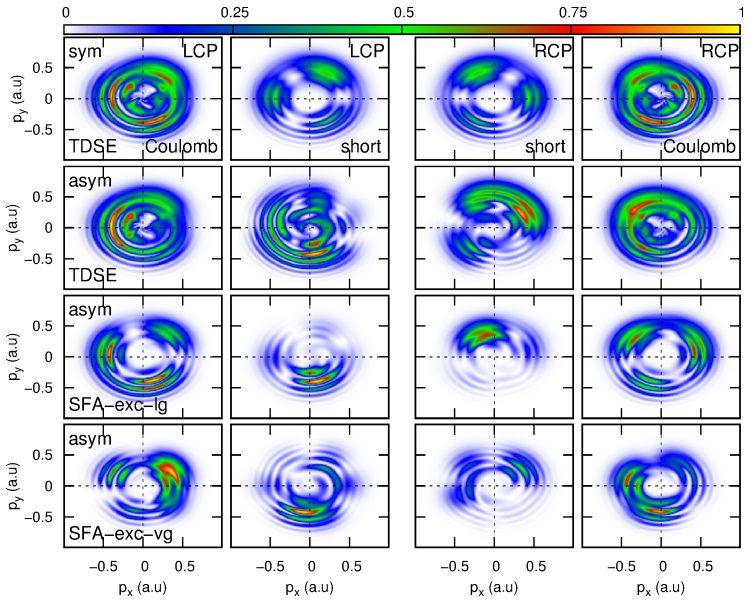

FIG. 10. Overview of the PEMDs for symmetric ("sym", A) and asymmetric ("asym", B –D) short-range and Coulomb model systems in few-cycle LCP and RCP fields, as labeled. Panels (A, B) depict results obtianed from the TDSE, panel (C) from the extended SFA in length gauge with $\psi_i(\boldsymbol{r}, t)$ as in eq. 29, and (D) from the extended SFA in velocity gauge with $\psi_i(\boldsymbol{r}, t)$.

(released when Γ is maximum) are depicted in Fig. 9. Following the same labeling as before, these three trajectories represent the ionization events associated to the three nuclei Z_2 (red), Z_3 (black) and Z_1 (blue). The chronological sequence of these events differ for the LCP ($Z_2 \to Z_3 \to Z_1$) and RCP ($Z_2 \to Z_1 \to Z_3$) simulations.

Since the maxima in Γ occur at different times for both systems (Fig. 9 E, F), the trajectories for the asymmetric model potential are released at different times compared to the symmetric case, inducing a clockwise (Z_3 and Z_1) or anticlockwise (Z_2) shift: In LCP fields, the red trajectories (Z_2) are released at earlier times, while for RCP fields the opposite is the case.

In order to disentangle the different effects, we first reduce the contribution of the excited states by increasing the laser wavelength to $\lambda = 3000$ nm ($t_p = 18.75$ fs), going from the multiphoton more to the tunnel regime. In Fig. 11, we compare the PEMDs obtained by the TDSE and CTMC method. Overall, the PEMDs obtained by TDSE and CTMC calculations show excellent agreement in this regime, where the Keldysh parameter $\gamma = 0.6$ is sufficiently

small, and the tunnel regime dominates. The contribution of excited states is negligible and the CTMC method provides accurate information on the enhanced/suppressed ionization rate associated to the three nuclei Z_n: The Stark-shift induces a shift of the peaks in the PEMDs. The peaks, which are related to three ionization events show an anticlockwise (red trajectory: Z_2) and clockwise (black trajectory: Z_3, blue trajectory: Z_1) shift as already observed for the 800 nm case . Furthermore, the intensity pattern strongly changes in the asymmetric case. While for the LCP simulations, the intensity of the peaks in the first and fourth quadrant (red, Z_2, and black, Z_3 trajectory) decreases, the opposite is true for the RCP calculations: Ionization, which proceeds via the nuclei Z_2 (red trajectory) and Z_1 (blue trajectory), is enhanced, thus leading to more intense peaks in the PEMD. To summarize, for $\lambda = 3000$ nm, the ionization dynamics, as well as the resulting PEMDs can thus be solely interpreted by properties of the electronic ground state (and its absence or presence of a permanent dipole $\boldsymbol{\mu}$) only.

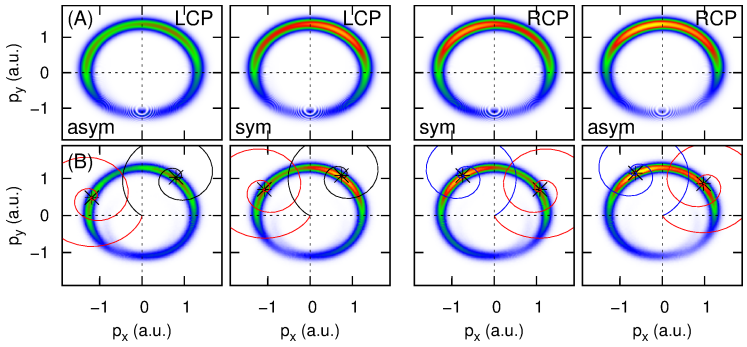

FIG. 11. PEMDs for the symmetric and asymmetric Coulomb model systems subject to LCP and RCP fields, with a wavelength of $\lambda = 3000$ nm, as labeled. (A) TDSE results; (B) CTMC results, including two characteristic trajectories. The color of the trajectories is connected to ionization near the three nuclei Z_1 (blue), Z_2 (red) and Z_3 (black).

Let us return to the $\lambda = 800$ nm case: The changes in the PEMDs induced by LCP and RCP laser fields with $\lambda = 800$ nm are more complex (Fig. 10). The first striking observation is that the overall pattern of the PEMDs of the Coulomb potentials (symmetric and asymmetric) induced by the same electric field (LCP or RCP) are very similar, with small variations in the intensity profile (panel A1 vs. B1). These differences occur as – depending on the polarization direction of the electric field – the intensity of the peaks related to the

ionization events near nuclei Z_2 (LCP: $\mathbf{p}$=(-0.5,0)) and Z_3 (RCP: $\mathbf{p}$=(-0.4,0.4)) increases, compared to the symmetric case. Due to this enhancement of ionization near different nuclei, the mirror symmetry between LCP and RCP (panels B1 and B4) is broken.

In order to again separate long-range contributions from the influence of excited states, we return to finite-range (asymmetric) potential, see Fig. 10. The reduction of the range of the asymmetric potential strongly affects the peak position. In contrast to the symmetric case, for asymmetric systems, the peaks show no uniform clockwise (LCP) or anticlockwise (RCP) rotation when going from the short-range to the Coulomb case. The trajectory calculations cannot capture this picture and predict the same clockwise shift induced by the long-range Coulomb interaction for both, the symmetric and asymmetric potential. As also the permanent dipoles $\boldsymbol{\mu}$ (and the resulting Stark-shifts) are very similar for both, the short-range and the Coulomb asymmetric systems, the ionization rate and the subsequent trajectory dynamics are almost identical. Consequently, the trajectories cannot explain the anticlockwise (LCP) and clockwise (RCP) rotation of the peaks in the second (LCP, Z_1) and fourth (RCP, Z_3) quadrant (Fig. 10).

We have also calculated the corresponding PEMDs via the extended SFA, see Fig. 10 (C, D). Not surprisingly, the standard SFA completely fails to provide an accurate picture, see also Ref. [39], and excited states have been included into the SFA. We note parenthetically that due to the absence of symmetry, the first two excited electronic states are no longer degenerate. The two realizations of the extended SFA in velocity and length gauge differ substantially: while the peak positions are somewhat similar, the intensity profile differs, in particular for the short-range cases. Comparison with the TDSE results, panel (B), shows for the short-range simulations some qualitative agreement for the peak positions with the already mentioned differences in the intensity profile. For the short-range simulations, it looks like the velocity gauge SFA agrees better with the TDSE results, however, none of the extended SFA calculations describes the TDSE results satisfactorily. Part of the problems can be again associated to the inaccurate description of the initial state ψ_i (SFA), as has been already discussed in Sec. III A, mainly caused by transient population of the continuum. However, as can be gathered from the populations (Appendix Fig. 19), the missing contribution is minor. Thus, the asymmetric multi-center nature of these potentials seems to cause problems to the SFA. Additionally, for the Coulomb-like systems, the differences between the PEMDs of the SFA and TDSE become more pronounced. For the Coulomb

systems, the length gauge extended SFA seems to agree better with the SFA results.

To summarize this section briefly, we have shown that an asymmetric potential breaks the mirror symmetry in the ionization dynamics induced by LCP and RCP fields. By including the permanent dipole moment $\boldsymbol{\mu}$ of the ground state, we showed, using the CTMC method, how the position and intensity of peaks changes when going to the asymmetric case. However, while this works well for electric fields with $\lambda = 3000$ nm, it is much worse for $\lambda = 800$ nm, where the multi-photon pathways to ionization dominate.

IV. NUMERICAL RESULTS: RANDOMLY ORIENTED MOLECULES

In many experiments, the molecules are not aligned with respect to the laser field. Consequently, each molecular orientation contributes to the final PEMD. In this section, we aim at investigating the contribution of different molecular configuration of our triatomic model systems to the final PEMD.

A. Randomly oriented short-range model systems – imprint of the carrier-envelope phase ϕ_{CEP}

So far, we have examined the ionization dynamics for one particular orientation of our triatomic model system. As in a typical experiment, the molecules are not aligned with respect to the laser field, the electric field interacts with all possible molecular orientation, and each of these molecular orientations contributes to the measured PEMDs. We mimic this effect by repeating the calculations for various orientations, while keeping the electric field unchanged. The results for the short-range model are summarized in Fig. 12.

A rotation of the triatomic potential by 180° rotates the triatomic pattern of the PEMD about the same angle, while the intensity pattern remains unchanged, with its maximum located in the upper hemisphere. If two molecular configurations behave mirror symmetrically to each other (with the mirror plane being the y-axis), the following symmetry relation between the PEMDs is valid (Fig. 13): $\sigma^{LCP}_{\pi/2}(p_x, p_y) = \sigma^{RCP}_{3\pi/2}(-p_x, p_y)$. This symmetry rule is generally valid for all configurations since for every molecular configuration (Fig. 12: $\sigma_{n_K(\pi/8)}$ with $n_K = 1, 7, 3, 5$) a mirror symmetric counterpart exist (Fig. 12: $\sigma_{n_K(\pi/8)}$ with $n_K = 15, 9, 13, 11$).

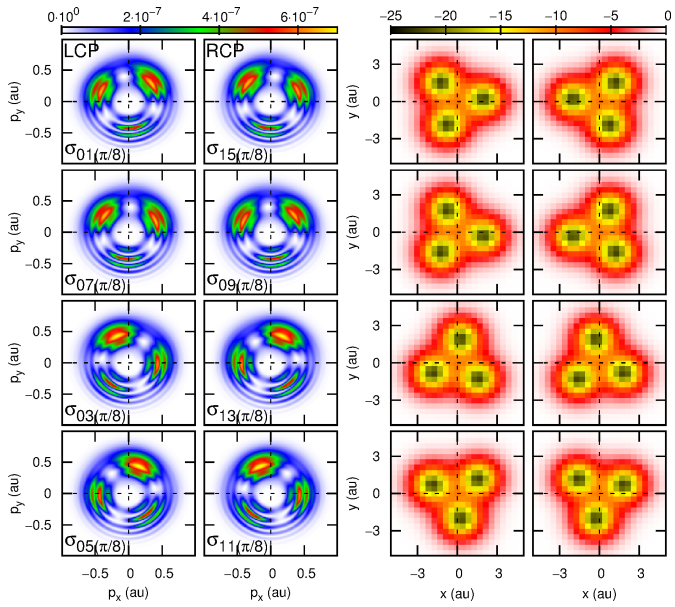

FIG. 12. Influence of the molecular orientation: shown are various absolute orientations of the short-range model system (right panels) and their corresponding PEMDs (left panels). The color bar represents the potential in eV.

In the case of short-range potentials, an additional symmetry relation between the PEMDs of different molecular configuration exist is valid (see Fig. 13): the systems shown in panels (B1) and (B2) differ by a rotation angle of 180°, and $\sigma^{LCP}_{n_K(\pi/8)}(p_x, p_y) \approx \sigma^{RCP}_{n_K(\pi/8)+\pi}(-p_x, p_y)$.

This relation is also the reason, why the molecular averaged PEMDs, panels (C1 and C2), are almost identical, which finally corresponds to averaged asymmetries $a(p_x, p_y)$ close to zero (D). These averaged spectra show no molecular structure anymore; the triatomic pattern is averaged out and only the ATI-rings remain. For both averaged spectra, the peak maximum is located at $\mathbf{p}$=(0,0.5). This maximum is a result of the CEP phase ϕ_{CEP} of the laser pulse. For $\phi_{CEP} = 0$, the absolute maximum of the vector field $\mathbf{A}_{max}(t_0) = (0, -E_0/\omega)$ has a negative sign, leading to photoelectrons with zero momentum in p_x and positive momentum in $p_y \approx -A_y$ (see panels C1 and C2).

Changing the relative phase to $\phi_{CEP} = \pi/2$ rotates the maxima either anticlockwise (RCP) or clockwise (LCP), depending on whether the sign of the vector field $\mathbf{A}_{max}(t_0) = (\pm E_0/\omega, 0)$ is positive (LCP) or negative (RCP) (Fig. 14 A). Consequently, the change of

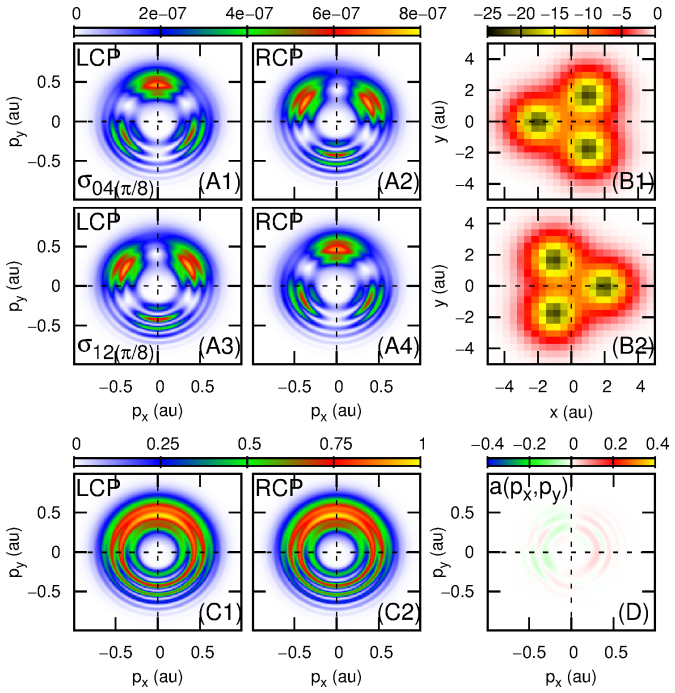

FIG. 13. (A1 - A4) PEMDs of two symmetric short-range potentials (B1, B2), rotated by 180° to each other. The color bar in panels (B) represents the potential in eV. The PEMDs result from interaction with LCP or RCP electric fields, as labeled. (C) PEMDs, which are averaged over 16 molecular orientations, and the corresponding asymmetries $a(p_x, p_y)$. Results for $\phi_{CEP} = 0$.

ϕ_{CEP} has strong impact on the PEMDs. For $\phi_{CEP} = \pi/2$, the differences between the averaged spectra are increased strongly, thus leading to large asymmetries $a(p_x, p_y)$ (Fig. 14 A). Thus, the corresponding asymmetry spectra strongly depend on the absolute phase of the laser pulse. For laser fields with longer pulse durations of $t_p = 20$ fs, the influence of the CEP-phase on the asymmetries vanishes, see Fig. 14 (B).

At this point, the question raises whether the structure observed and discussed in the individual PEMDs would be experimentally accessible under typical alignment conditions. Figure 15 presents averaged spectra starting from a "perfectly" aligned system to the completely averaged spectra by incrementally decreasing the degree of alignment. Panel (A) presents the PEMD for one configuration only, as a reference, while the following panels average over three, five and so on configurations differing by $\pi/8$ (or 22.5°), corresponding to an averaging over (B) 45°, (C) 90° and so on. As can be gathered clearly, even an averaging over 45°, corresponding to $\langle \cos^2(45°) \rangle = 0.5$ still displays the imprints of the molecular

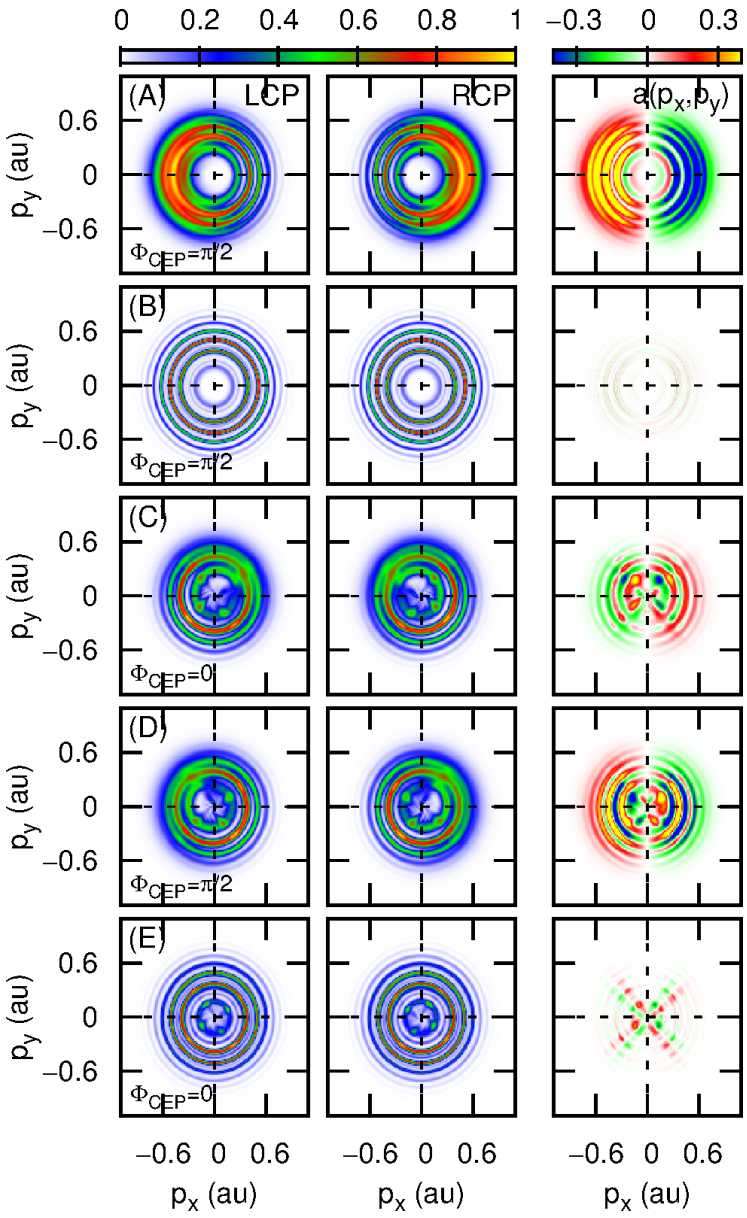

FIG. 14. Orientation-averaged PEMDs induced by LCP and RCP laser pulses and the resulting asymmetries $a(p_x, p_y)$ for different symmetric model systems: (A, B) short-range potential with $\phi_{CEP} = \pi/2$, FWHM of 5 (A) and 20 fs (B). (C – E) Coulomb potential: (C) FWHM of 5 fs, $\phi_{CEP} = 0$, (D) FWHM of 5 fs, $\phi_{CEP} = \pi/2$, and (E) and FWHM of 15 fs.

structure discussed above. Therefore, we believe that these structures will be experimentally accessible.

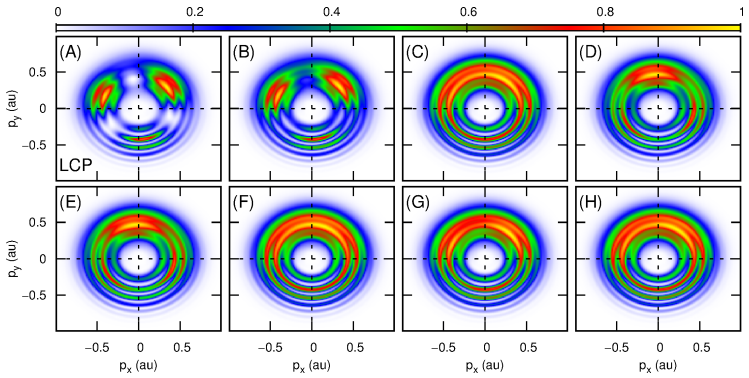

FIG. 15. As before, orientation-averaged PEMDs induced by LCP with a FWHM of $t_p = 5$ fs, $\phi_{CEP} = 0$, however, now for (partially) aligned model systems. Panel (A) displays the PEMD of one orientation only, $\sigma_{\pi/8}(p_x, p_y)$, while the following panels include averaging over the neighboring configurations rotated by $\pm n\pi/8$, with $n = 1, 2, 3$ for panels (B, C, D) and so on.

B. Randomly oriented Coulombic and asymmetric model systems

In comparison to the short-range case, the differences of the averaged PEMDs for the long-range potential (Appendix Fig. 17) are more profound. Since the long-range interaction and the excited states affect the relative peak position in the LCP (clockwise shift) and RCP (anticlockwise shift) spectra in different ways, even for ϕ_{CEP}, the peak maxima are located in different quadrants (RCP: second quadrant, LCP: third quadrant), thus leading to pronounced asymmetries. Thus, in contrast to short-range potentials, in Coulomb systems even for a CEP of $\phi_{CEP} = 0$, a non-zero asymmetry remains (Fig. 14 (C)), which changes substantially, when changing the CEP to $\phi_{CEP} = \pi/2$. Increasing the pulse duration to 15 fs leads to a significant reduction in the asymmetries $a(p_x, p_y)$, see Fig. 14 (E). The remaining small asymmetries are mainly located at small momenta and are a result of the large differences between the position of finger-like structure of both spectra. For higher momenta, the ATI-rings become centro-symmetric and $a(p_x, p_y)$ is close to zero.

As already discussed above, the intensity pattern of the peaks in PEMDs changes significantly for an asymmetric potential (see Fig. 10). However, many of these differences average out, and the averaged PEMDs of the asymmetric potential have almost the same shape as the corresponding PEMDs of the symmetric system (see Fig. 16). In general, for the asymmetric model system, there are no pairs of mirror-symmetric (Coulomb)

potentials. Nevertheless, there are configuration pairs (Fig. 16: $V_{(\pi/8)}(x,y)\&V_{(4\pi/8)}$ and $V_{(9\pi/8)}(x,y)\&V_{(12\pi/8)}$) where the corresponding PEMDs are approximately mirror symmetric to each other ($\sigma^{LCP}_{\pi/8}(p_x,p_y) \approx \sigma^{RCP}_{4\pi/8}(-p_x,p_y)$). For these types of configurations, although no overall mirror symmetry is present, the position of the nucleus with highest charge Z_3 (and Z_3') behaves mirror symmetric to each other, thus leading to the approximate relation described above. Thus, the asymmetries $a(p_x,p_y)$ of the averaged PEMD of the symmetric and asymmetric systems do not differ significantly from each other, and the major part of the asymmetry is caused by CEP effects of the laser field.

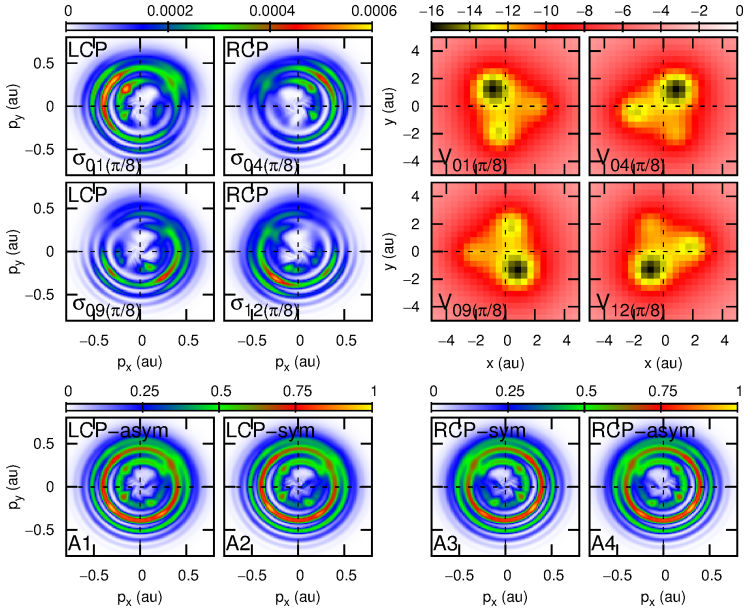

FIG. 16. Influence of the orientation on the PEMDs (normalized) for asymmetric Coulomb potentials. Shown are PEMDs $\sigma_{n_K(\pi/8)}$ induced by either LCP or RCP fields, calculated for four different orientations of the asymmetric potential. The color bar represents the potential in eV. The molecular configurations are rotated by $n_k(\pi/8)$ with $n_K = 1, 4, 9, 12$. Also shown are the orientation averaged PEMDs for the symmetric (sym) and asymmetric (asym) long-range systems (A1-A4).

V. DISCUSSION AND SUMMARY

In this work, we have systematically investigated the strong-field ionization dynamics of small, non-linear model molecules with very different properties. We have employed a large toolbox of different methods, namely besides the full numerical solution of the time-dependent Schrödinger equation (TDSE) classical trajectory Monte-Carlo (CTMC) calculations and the strong-field approximation (SFA). The CTMC calculations were modified such that the explicit barrier width b_0 directly entered the Keldysh parameter γ and thus influenced the ionization rate, enabling a spatially anisotropic ionization. The SFA calculations were extended in order to support a bound wavepacket rather than only the electronic ground state as initial state. The combination of methods allowed us to disentangle the contributions of the long-range tail of the (Coulomb) potential on the course of the liberated electron from contributions mainly caused by bound excited states.

Based on our analysis, we can identify several central aspects describing the strong-field ionization dynamics of non-linear model molecules: (A) Interaction with mid-infrared wavelengths, shifting the regime of ionization towards the tunneling mechanism, substantially reduces the influence of both, excited states, and the long-range character of the potential. This is due to the facts, that (i) population transfer to higher lying electronic states becomes negligible compared to the multi-photon case, and (ii) the vector potential is much higher, thus accelerating the electron occurring in the continuum much faster away from the parent ion, thereby reducing the impact of the long-range character. Thus, almost no information of the molecular system can be extracted from the photoelectron momentum distributions (PEMDs), which are mainly shaped by the electric field, i.e. the carrier-envelope phase of the field. Classical trajectory methods, as well as SFA calculations are very well suited to describe the PEMDs in this regime. (B) For near-infrared laser fields and wavelengths corresponding more to the multi-photon regime of ionization, the situation changes completely: both, excited states and the long-range character become important. While the long-range character merely decelerates the photoelectrons, and thus, induces a shift in the PEMDs, the role of excited states is many-faceted: as we have seen for the case of model systems with a larger internuclear distance, where the excited states are energetically closer, interaction with a (quasi-resonant) laser fields drives a bound-state wavepacket featuring a pronounced localization dynamics. These, in turn, strongly influences the ionization dynam-

ics, in particular, the ionization time. The resulting PEMDs feature a three-fold symmetric structure originating from the three-fold symmetry of the model potentials interacting with the few-cycles laser pulses. As excited electronic states are, in the presence of a strong laser field, additionally Stark shifted, the may even lie energetically above the quasi-static tunnel barrier, leading to conditions as for over-the-barrier ionization. Still, as long as the bound dynamics is governed by a few, dominating electronic states only, it is possible to calculate the PEMDs with the SFA, when extending it to include a bound wavepacket as an initial state, rather than the field-free ground state only. It is also possible to qualitatively calculate the PEMDs using classical trajectory methods, with the common assumptions for initial conditions in the over-the-barrier ionization range. (C) Coulomb potentials, in contrast to short-range potentials, substantially complicate the strong-field (ionization) dynamics for several reasons: (i) Coulomb potentials support an infinite number of electronically excited states, and thus makes a proper description of the bound initial state much harder. (ii) For similar ground-state energies, the quasi-static tunnel barrier in Coulomb potentials is lower than in short-range potentials, and thus, over-the-barrier ionization sets in earlier. (iii) Due to the contribution of Rydberg-like states, a finger-like structure with low momenta occurs in the PEMDs, which cannot be properly described with neither SFA nor CTMC methods. (D) Asymmetric model systems have the complication that the charge distribution is not symmetric and thus, a permanent dipole moment exists. As a consequence, the Stark-shifted states lead to changes in the ionization times and rates. As has been described already for OCS, a linear molecule with a permanent dipole moment, ionization when the permanent dipole points parallel to the electric field vector is enhanced, while the opposite is true for anti-parallel arrangement of permanent dipole and electric field vector [67–69]. (E) All the above holds, as long as the molecules are fixed in space or aligned. If we consider additionally that the laser pulses interact with an ensemble of randomly oriented molecules, many of the features in the PEMDs, which could be attributed to molecular properties, average out and CEP effects dominate.

Although we have examined planar model systems, we strongly believe that these findings provide important insight and physical understanding for the description and modeling of the strong-field ionization of general, real molecules and their corresponding photoelectron spectra. In future, we plan to extend our investigation for non-planar model systems and aim at investigating strong-field circular dichroism of the photoelectron momentum distribution.

VI. APPENDIX

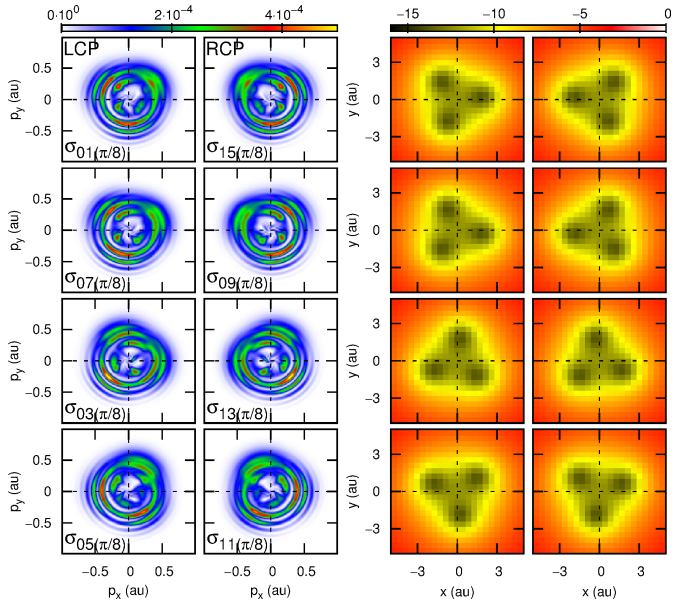

FIG. 17. The influence of the molecular orientation on the PEMDs for symmetric Couloub potentials. The color bar represents the potential in eV. Shown are PEMDs induced by either left (LCP) or right circularly polarized (RCP) electric fields, which are calculated for different orientations of the triatomic model system.

ACKNOWLEDGMENTS

The authors highly acknowledge financial support within the priority programme QUTIF (SPP) from the German Science Foundation (DFG), grants number GR 4482/3-1. M. P. acknowledges helpful discussions with Dr. Lun Yue.

VII. LITERATURE

[1] M. Y. Ivanov, M. Spanner, and O. Smirnova, J. Mod. Opt. **52**, 165 (2005).

[2] F. Krausz and M. Ivanov, Rev. Mod. Phys. **81**, 163 (2009).

[3] B. Zhang, J. Yuan, and Z. Zhao, Phys. Rev. Lett. **111**, 163001 (2013).

[4] D. Hochstuhl and M. Bonitz, J. Chem. Phys. **134**, 084106 (2011).

[5] D. J. Haxton, K. V. Lawler, and C. W. McCurdy, Phys. Rev. A **83**, 063416 (2011).

[6] S. Ohmura, T. Kato, T. Oyamada, S. Koseki, H. Ohmura, and H. Kono, J. Phys. B: At. Mol. Phys. **51**, 034001 (2018).

[7] J. Caillat, J. Zanghellini, M. Kitzler, O. Koch, W. Kreuzer, and A. Scrinzi, Phys. Rev. A **71**, 012712 (2005).

[8] A. Castro, M. A. L. Marques, and A. Rubio, J. Chem. Phys. **121**, 3425 (2004).

[9] U. De Giovannini, D. Varsano, M. A. L. Marques, H. Appel, E. K. U. Gross, and A. Rubio, Phys. Rev. A **85**, 062515 (2012).

[10] A. Sissay, P. Abanador, F. Mauger, M. Gaarde, K. Schafer, and L. K., J. Chem. Phys. **145**, 094105 (2016).

[11] X. Andrade, D. Strubbe, U. De Giovannini, A. H. Larsen, M. J. T. Oliveira, J. Alberdi-Rodriguez, A. Varas, I. Theophilou, N. Helbig, M. J. Verstraete, L. Stella, F. Nogueira, A. Aspuru-Guzik, A. Castro, M. A. L. Marques, and A. Rubio, Phys. Chem. Chem. Phys. **17**, 31371 (2015).

[12] X. Chu, Phys. Rev. A **82**, 023407 (2010).

[13] E. Penka Fowe and A. D. Bandrauk, Phys. Rev. A **84**, 035402 (2011).

[14] D. A. Telnov and S.-I. Chu, Phys. Rev. A **80**, 043412 (2009).

[15] X. Chu and S.-I. Chu, Phys. Rev. A **63**, 023411 (2001).

[16] W. Becker, F. Grasbon, R. Kopold, D. B. Milošević, G. G. Paulus, and H. Walther, *Above-threshold ionization: from classical features to quantum effects*, Vol. 48 (2002) p. 35.

[17] M. Awasthi, Y. V. Vanne, A. Saenz, A. Castro, and P. Decleva, Phys. Rev. A **77**, 063403 (2008).

[18] F. H. M. Faisal, J. Phys. B: At. Mol. Phys. **6**, L89 (1973).

[19] H. R. Reiss, Phys. Rev. A **22**, 1786 (1980).

[20] L. Keldysh, Sov. Phys. JETP **20**, 1307 (1965).

[21] D. B. Milošević, Phys. Rev. A **74**, 063404 (2006).

[22] D. Dimitrovski, C. P. J. Martiny, and L. B. Madsen, Phys. Rev. A **82**, 053404 (2010).

[23] V. I. Usachenko and S.-I. Chu, Phys. Rev. A **71**, 063410 (2005).

[24] T. Zuo and A. D. Bandrauk, Phys. Rev. A **52**, R2511 (1995).

[25] A. Giusti-Suzor, F. H. Mies, L. F. DiMauro, E. Charron, and B. Yang, Journal of Physics B: Atomic, Molecular and Optical Physics **28**, 309 (1995).

[26] T. Kjeldsen, L. Madsen, and J. Hansen, Phys. Rev. A **74**, 035402 (2006).

[27] A. Saenz, Phys. Rev. A **61**, 051402 (2000).

[28] M. Lein, T. Kreibich, E. K. U. Gross, and V. Engel, Phys. Rev. A **65**, 033403 (2002).

[29] S. Gräfe and M. Y. Ivanov, Phys. Rev. Lett. **99**, 163603 (2007).

[30] G. Sansone, F. Kelkensberg, M. F. Kling, M. Ivanov, J. F. Perez-Torres, F. Morales, W. Siu, O. Ghafur, P. Johnsson, M. Swoboda, E. Benedetti, F. Ferrari, F. Lepine, J. L. Sanz-Vicario, S. Zherebtsov, I. Znakovskaya, A. l'Huillier, M. Nisoli, F. Martin, and M. J. J. Vrakking, Nature **465**, 763 (2010).

[31] A. Palacios, J. L. Sanz-Vicario, and F. Martín, J. Phys. B: At. Mol. Phys. **48**, 242001 (2015).

[32] A. Saenz, Phys. Rev. A **67**, 033409 (2003).

[33] E. Dehghanian, A. D. Bandrauk, and G. Lagmago Kamta, J. Chem. Phys. **139**, 084315 (2013).

[34] D. Ursrey, F. Anis, and B. D. Esry, Phys. Rev. A **85**, 023429 (2012).

[35] L. Yue, P. Wustelt, A. M. Sayler, F. Oppermann, M. Lein, G. G. Paulus, and S. Gräfe, Phys. Rev. A **98**, 043418 (2018).

[36] P. Wustelt, F. Oppermann, L. Yue, M. Möller, T. Stöhlker, M. Lein, S. Gräfe, G. G. Paulus, and A. M. Sayler, Phys. Rev. Lett. **121**, 073203 (2018).

[37] C. Lefebvre, H. Z. Lu, S. Chelkowski, and A. D. Bandrauk, Phys. Rev. A **89**, 023403 (2014).

[38] K.-J. Yuan, H. Lu, and A. D. Bandrauk, J. Phys. B: At. Mol. Phys. **50**, 124004 (2017).

[39] M. Paul, L. Yue, and S. Gräfe, Phys. Rev. Lett. **120**, 233202 (2018).

[40] M. H. M. Janssen and I. Powis, Phys. Chem. Chem. Phys. **16**, 856 (2014).

[41] M. M. R. Fanood, I. Powis, and M. H. M. Janssen, J. Phys. Chem. A **118**, 11541 (2014).

[42] C. Lux, M. Wollenhaupt, T. Bolze, Q. Liang, J. Köhler, C. Sarpe, and T. Baumert, Angew. Chem. **124**, 5086 (2012).

[43] C. Lux, M. Wollenhaupt, C. Sarpe, and T. Baumert, Chem. Phys. Chem. **16**, 115 (2015).

[44] R. Cireasa, A. E. Boguslavskiy, B. Pons, M. C. H. Wong, D. Descamps, S. Petit, H. Ruf, N. Thire, A. Ferre, J. Suarez, J. Higuet, B. E. Schmidt, A. F. Alharbi, F. Legare, V. Blanchet, B. Fabre, S. Patchkovskii, O. Smirnova, Y. Mairesse, and V. R. Bhardwaj, Nat. Phys. **11**, 654 (2015).

[45] S. Beaulieu, A. Comby, B. Fabre, D. Descamps, A. Ferre, G. Garcia, R. Geneaux, F. Legare, L. Nahon, S. Petit, T. Ruchon, B. Pons, V. Blanchet, and Y. Mairesse, Faraday Discuss. **194**, 325 (2016).

[46] M. Paul, L. Yue, and S. Gräfe, J. Mod. Opt. **64**, 1104 (2017).

[47] M. D. Feit, J. A. Fleck, and A. Steiger, J. Comput. Phys. **47**, 412 (1982).

[48] S. G. J. M. Frigo, ICASSP conference proceedings **3**, 1381 (1998).

[49] R. Kosloff and H. Tal-Ezer, Chem. Phys. Lett. **127**, 223 (1986).

[50] R. Heather and H. Metiu, J. Chem. Phys. **86**, 5009 (1987).

[51] A. Keller, Phys. Rev. A **52**, 1450 (1995).

[52] S. V. Popruzhenko, Journal of Physics B: Atomic, Molecular and Optical Physics **47**, 204001 (2014).

[53] N. B. Delone and V. P. Krainov, J. Opt. Soc. Am. B **8**, 1207 (1991).

[54] J. E. Gentle, *Random Number Generation and Monte Carlo Methods* (Springer, 2003).

[55] F. H. M. Faisal, J. Phys. B **6**, L89 (1973).

[56] K. Rzazewski and R. W. Boyd, J. Mod. Opt. **51**, 1137 (2004).

[57] D. Bauer, D. B. Milošević, and W. Becker, Phys. Rev. A **72**, 023415 (2005).

[58] W. Becker, J. Chen, S. G. Chen, and D. B. Milošević, Phys. Rev. A **76**, 033403 (2007).

[59] N. Takemoto and A. Becker, Phys. Rev. A **84**, 023401 (2011).

[60] N. Takemoto and A. Becker, Phys. Rev. Lett. **105**, 203004 (2010).

[61] C. L. Erattupuzha, S. Covington, A. Russakoff, E. Lötstedt, S. Larimian, V. Hanus, S. Bubin, M. Koch, S. Gräfe, Baltuška, X. Xie, K. Yamnouchi, K. Varga, and M. Kitzler, J. Phys. B: At. Mol. Phys. **50**, 125601 (2017).

[62] D. G. Arbó, S. Yoshida, E. Persson, K. I. Dimitriou, and J. Burgdörfer, Phys. Rev. Lett. **96**, 143003 (2006).

[63] O. Smirnova, M. Spanner, and M. Y. Ivanov, J. Phys. B: At. Mol. Opt. Phys **39**, S307 (2006).

[64] S. Gräfe, J. Doose, and J. Burgdörfer, J. Phys. B: At. Mol. Phys. **45**, 055002 (2012).

[65] I. Kawata, H. Kono, and A. D. Bandrauk, Phys. Rev. A **64**, 043411 (2001).

[66] M. Spanner, S. Gräfe, S. Chelkowski, D. Pavicic, M. Meckel, D. Zeidler, A. B. Bardon, B. Ulrich, A. D. Bandrauk, D. M. Villeneuve, R. Dörner, P. B. Corkum, and A. Staudte, J. Phys. B **45**, 194011 (2012).

[67] L. Holmegaard, J. L. Hansen, L. Kalhoj, S. Louise Kragh, H. Stapelfeldt, F. Filsinger, J. Kup-

per, G. Meijer, D. Dimitrovski, M. Abu-samha, C. P. J. Martiny, and L. B. Madsen, Nat. Phys. **6**, 428 (2010).

[68] J. L. Hansen, L. Holmegaard, L. Kalhøj, S. L. Kragh, H. Stapelfeldt, F. Filsinger, G. Meijer, J. Küpper, D. Dimitrovski, M. Abu-samha, C. P. J. Martiny, and L. B. Madsen, Phys. Rev. A **83**, 023406 (2011).

[69] D. Dimitrovski, M. Abu-samha, L. B. Madsen, F. Filsinger, G. Meijer, J. Küpper, L. Holmegaard, L. Kalhøj, J. H. Nielsen, and H. Stapelfeldt, Phys. Rev. A **83**, 023405 (2011).

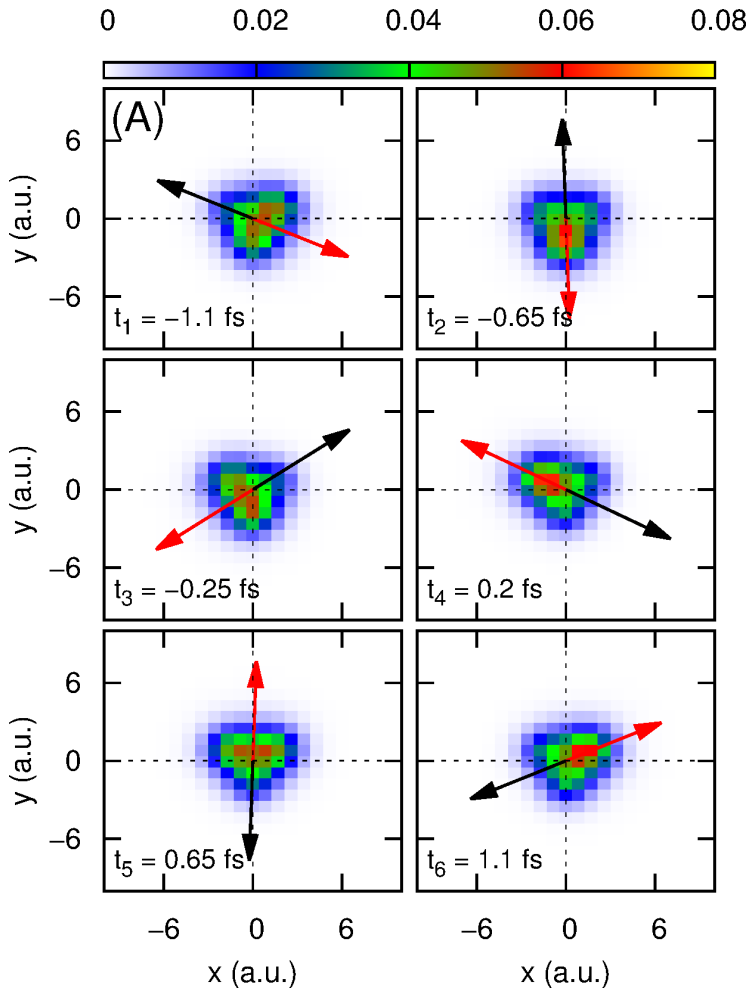

FIG. 18. As in Fig. 4: Bound electron dynamics for the symmetric short range model system, but here for small $R_{ij} = 3.5$ a.u. (A) Snapshots of the bound electronic density of the superposition state $\phi_i(\boldsymbol{r}, t_i) = \sum_{n=1}^{3} c_n(t_i)\phi_n(\boldsymbol{r})$ with coefficients $c_n(t)$ extracted as described in section II D. Also shown are the characteristic electric field vectors $\mathbf{E}(t_i)$ (black arrows) at these times t_i. Tunneling occurs in the direction indicated by the red arrow. (B) Ionization rate Γ calculated with tunnel barriers b_0 as shown in panel (C). (C) Cuts along the potential $V(\boldsymbol{r}, t(\zeta))$, with ζ depending on the direction of the electric field vector $\mathbf{E}(t)$. While for Fig. 4, the bound electron wavepacket localized in the direction parallel to the electric field, leading to ionization from the "up-field" side, here, for smaller $R_{ij} = 3.5$ a.u., the opposite is the case: localization is anti-parallel to the field vector, and ionization proceeds predominantly from the "down-field" side.

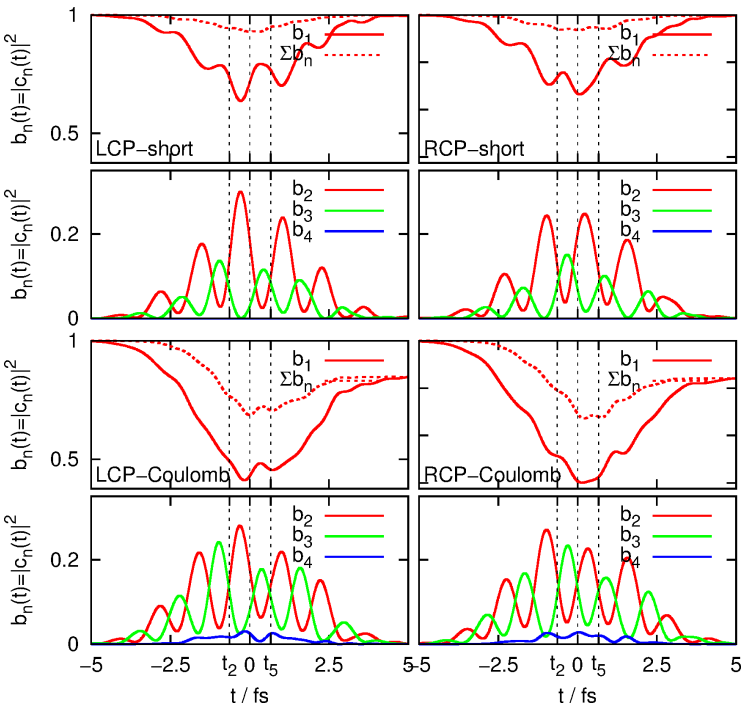

FIG. 19. Overview of the time-dependent populations $b_n(t) = |c_n(t)|^2$ of the ground state b_1 and the first three excited states b_{n+1} of all asymmetric model systems (short- and Coulomb-like potential) interacting with either left (LCP) or right (RCP) circularly polarized electric fields.

Chapter 4

Summary

This work investigates the influence of excited states and long-range Coulomb interaction on the ionization dynamics of triatomic model molecules with different potentials and molecular arrangements. The focus is on the interaction of such systems with intense few-cycle, circularly polarized infrared laser pulses, of varying CEPs, pulse durations, and wavelengths. Considered wavelengths range from 800 to 3000 nm corresponding to the multiphoton and the tunnel regime. For a detailed characterization of the ionization process, fully ab-initio quantum dynamical simulations were performed and analyzed by means of classical trajectories (CTMC method) and by an extended version of the strong-field approximation (SFA). Here, the CTMC was primarily employed to study the long-range Coulomb interaction between the photoelectrons and the parent ion, whereas the extended version of the SFA was developed to investigate the influence of excited bound states on the ionization process.

In the first part of this thesis, the interaction of triatomic model systems with intense few-cycle, circularly polarized infrared laser ($\lambda = 800$ nm) pulses was studied. The numerical model system, consisting of three space-fixed nuclei with tunable charges and a single active electron with two spatial degrees of freedom (within the plane of the molecule), was developed to examine CDAD-effects of nonlinear model-molecules by solving the TDSE. The time-dependent electronic density at specific times and the 2D-PEMD were calculated for both symmetric and asymmetric nuclear arrangements. CD effects were then defined as asymmetries between the normalized difference of PEMDs induced by left- and right-circularly polarized electric fields. For a more intuitive interpretation of the results, 800 nm laser fields with pulse durations of 1 and 5 fs are used. The snapshots showed that the electronic density starts its evolution from different nuclei Z_3 (LCP) and Z_1 (RCP) for different polarized fields, respectively. After the electron has left its parent nucleus, it evolves either clockwise (LCP) or counterclockwise (RCP) in the continuum. Here, it was found that the ionization process occurs within two half cycles, $t < t_0$ and

$t > t_0$, around the maximum intensity of the laser-pulse at t_0. The vector potentials $\mathbf{A}(t_0 < t)$ and $\mathbf{A}(t > t_0)$ were used to interpret the position and intensity of the two peaks in PEMD by means of the SFA. The difference in magnitude of these two peaks could be traced back to the transient population of excited states. The change in the CEP leads to a counterclockwise (clockwise) rotation in the PEMDs for LCP (RCP) field, which, in turn, strongly affects the corresponding asymmetries. For symmetric systems, the PEMDs of LCP and RCP fields are found to be mirror images of each other, as expected, leading to a pronounced CDAD spectrum with a characteristic symmetry. By increasing the pulse duration to 5 fs, an ATI-ring structure was found as observed in experiments. For asymmetric nuclear charge configurations, the snapshots revealed that a locally increased Coulomb attraction changes the ionization dynamics significantly. Since the asymmetric potential exhibits no mirror symmetry, the symmetry of the evolution of the RCP- and LCP-driven electronic density was broken. The higher the degree of asymmetry in the potential, the higher the corresponding CDAD-effect. This way, the complex pattern in the spectrum could be explained by a combination of fully quantum mechanical and semiclassical approaches, while a detailed theoretical analysis of the ionization process remains challenging.

In the second part of this thesis, the results obtained by the fully ab-inito quantum dynamical methods were analyzed in more detail by means of classical trajectories and a numerical solution of the SFA. The chosen methods are well suited to study the contribution of the long-range Coulomb interaction in the continuum and influence of the ground-state during the ionization process. To reduce the number of excited states and the contribution of the Coulomb interaction in the continuum, the range of the triatomic potential was systematically reduced. The numerical solution of the TDSE for model systems with different ranges were analyzed by means of classical trajectories (SMM) and the SFA. All calculated PEMDs showed the same threefold symmetric structure with the expected above-threshold ionization (ATI) rings, only the position and the intensities of the peaks differ. Classical trajectories revealed that the origin of this threefold structure could be traced back to three representative ionization events at times when the tunnelbarrier is relatively narrow, resulting in three trajectories starting at different tunnelexits at one of the three nuclei Z_1, Z_2, and Z_3. The final momenta of the three selected trajectories could then be assigned to the three peaks in the PEMD, while both, the final momenta of the trajectories and the threefold electronic structure, are rotated in the same clockwise direction for Coulomb-like systems. For Coulomb-like systems, an additional finger-like structure was observed, which was identified as contributions from energetically higher lying-excited states. For symmetric systems, the PEMDs induced by LCP and RCP fields are mirror images of each other. This symmetry relation vanishes for asymmetric nuclear

configurations. The higher the degree of asymmetry of the nuclear potential, the larger are the differences between both spectra. Due to the large changes in the electronic structure, the triatomic structure vanishes in both spectra and resulting differences (CDAD) increase. By including the permanent dipole via the Stark shift in the CTMC model, the intensities and positions of the three peaks in the spectra calculated with the semiclassical model were in good agreement with the results obtained via TDSE simulations.

In the third part of this thesis, the ionization dynamics of triatomic model with different orientation and internuclear distances was investigated. Building on the results of the first and second part of this thesis, the previously used methods, e.g. the CTMC and SFA, were extended to describe the altered ionization behavior found in triatomic systems with larger internuclear distance R_{ij}. For these short-range systems with larger R_{ij}, a different ionization mechanism was proposed, where the ionization takes place from the excited state at the nuclei from the "up-field site" of the electric field vector similar as for Charge-resonance enhanced ionization. The ionization mechanism was modeled by means of classical trajectories with modified initial conditions, while the trajectories show the same evolution in the continuum as the electronic density calculated with the TDSE. The corresponding final momenta of the trajectories were also in good agreement with the position of three peaks in the PEMDs, displaying the same 60° rotation when moving to the systems with smaller R_{ij}, in which the ionization occurs from the ground state at the "down-field side" of the electric field vector. An analysis of the dynamics of the bound superposition state $\psi_s(\mathbf{r}, t)$ (see Sec. 3.3) showed how the position of the corresponding electronic density peaks changes during propagation. Depending on the internuclear distance, a strong localization of the electronic density peaked along the direction ($R_{ij} = 3.5$ au,"down-field side") or in the opposite direction ($R_{ij} = 5.5$ au,"up-field side") of the electric field vector. Only the extended SFA, where ionization occurs via a superposition state $\psi_s(\mathbf{r}, t)$ including the first two excited states, was able to reproduce all significant features appearing in the PEMDs of the TDSE calculations, indicating the importance of excited states during ionization. For Coulomb-like systems with a larger internuclear distance, the over-the-barrier mechanism becomes the dominant ionization process. For this purpose, the initial phase-space conditions of the trajectories were modified, resulting in an counterclockwise rotation of the trajectories in momentum space, similar to the rotation of the peaks observed in PEMDs of the TDSE simulation. The PEMDs calculated with the extended SFA for the Coulomb-like systems were in good agreement with the results obtained by the TDSE simulation, showing that the excited states are also inducing a clockwise rotation of the threefold structure similar to the shift caused by long-range Coulomb interaction. The changes in the intensity profile of the PEMDs, related to asymmetric Coulomb systems, was only be reproduced by the

CTMC method in the tunnel-regime for laser with wavelengths of $\lambda = 3000$ nm. Here, the trajectories, which are released to times when ionization rate maxima (Stark-shift is included) appear, show how the ionization mechanism changes for these asymmetric systems: ionization from the nuclei Z_3 and Z_2 is strongly suppressed for the LCP-case, whereas ionization from the nuclei Z_1 and Z_2 is strongly enhanced in the RCP case. In the multiphoton-regime ($\lambda = 800$ nm), too many excited states are involved in the ionization process and the trajectory model cannot explain the complex asymmetric changes in the PEMDs. Not even the extended SFA in the length gauge was able to reproduce all significant features in PEMDs of the TDSE calculation for both, asymmetric short-range and Coulomb-like systems. Additionally, it was shown how the threefold electronic structure in the PEMD depends on the orientation of the triatomic model molecule. However, the threefold structure disappears when the PEMD is averaged over all molecular orientations; only the ATI-ring structure remains. The corresponding intensity profile only depends on the electric field parameter and not on the molecular potential itself. The molecular averaged PEMDs were used to calculate the CDAD spectra. It was found that the CDAD strongly depends on the CEP of the electric field, thus decreasing for laser-fields with longer pulse-durations. The averaged PEMDs and CDAD spectra of the symmetric and asymmetric Coulomb-like systems differ not significantly from each other. This indicates that the CDAD-effect is primarily produced by the CEP of the laser field and not by the asymmetry of the potential.

Overall, the present work presents a detailed investigation of the strong-field driven ionization dynamics of triatomic model systems. The influence of long-range Coulomb interactions and excited states for triatomic systems with different potential ranges, internuclear distances, and molecular orientation was investigated in detail by analyzing the fully ab initio quantum-dynamical simulations by means of classical trajectories and various versions of the SFA. Of particular importance are the CDAD spectra, calculated from the averaged PEMDs of the symmetric and asymmetric Coulomb-like systems. These spectra show considerable similarities, indicating that the CDAD-effect is primarily produced by the CEP of the laser field and not due to the asymmetry of the potential. The question arises, therefore, how the CEP affects the PECD. The results presented in this thesis provide an important precursor to understand such details of the ionization mechanism underlying the PECD by revealing how the CEP affects the characteristic forward/backward asymmetry.

In the future, the investigations of the two-dimensional model presented in this thesis can be expanded towards three-dimensional systems, aiming to describe multiphoton photoelectron circular dichroism occurring in the forward and backward direction with purely ab initio calculations.

Chapter 5

Zusammenfassung

Im Rahmen dieser Arbeit wird die Ionisationsdynamik von dreiatomigen Modellsystemen mit unterschiedlichen Kerngeometrien untersucht. Der Fokus liegt dabei auf der Wechselwirkung solcher Systeme mit ultrakurzen, zirkular polarisierten Lichtpulsen mit unterschiedlichen Träger-Einhüllenden (TE) Phasen, Pulsdauern und Wellenlängen. Um Ionisationsdynamiken sowohl im Multiphotonenregime als auch im Tunnelregime simulieren zu können, werden elektrische Felder mit Wellenlängen im infrarot Bereich von 800 bis 3000 nm verwendet. Die detaillierte Charakterisierung der Ionisationsdynamik erfolgt mithilfe von quantendynamischen ab initio Simulationen, klassischen Trajektorien und einer erweiterten Variante der Stark-Feld Näherung (SFN). Dabei wird das Trajektorienmodell zur Analyse der langreichweitigen Wechselwirkungen zwischen dem Photoelektron und dem ionisierten Modellsystem verwendet, wohingegen die erweiterte Variante der SFN dazu dient, um den Einfluss zwischenzeitlich angeregter Zustände auf die Ionisationsdynamik zu untersuchen.
Im ersten Teil dieser Doktorarbeit wird die Wechselwirkung von dreiatomigen Modellsystemen mit ultrakurzen, zirkular polarisierten Lichtpulsen im infrarot Bereich ($\lambda = 800$ nm) untersucht. Dafür wird ein numerisches Modellsystem entwickelt, das aus drei ortsfesten Kernen mit variabler Ladungszahl und einem aktivem Elektron besteht, welches sich entlang zweier räumlicher Dimensionen (2D) bewegen kann. Das Modell ist geeignet, den Zirkulardichroismus in den Photoelektronen-Winkelverteilungen (ZDPW) für nichtlineare Modellmoleküle mithilfe der Lösung der zeitabhängigen Schrödinger-Gleichung zu untersuchen und steht repräsentativ für komplexe Moleküle. Der ZDPW ist dabei der Unterschied zwischen den durch links- und rechtszirkular polarisierten (LZP und RZP) Licht erzeugten Photoelektronenspektren σ^{LZP} und σ^{RZP}. Zur Analyse des ZDPW werden zeitabhängige Elektronendichten und 2D-Photoelektronenspektren, sowohl für symmetrische (alle drei Kernladungszahlen sind gleich) als auch für asymmetrische (alle drei Kernladungszahlen sind voneinander verschieden) dreiatomige Modellsysteme zu

bestimmten Zeiten berechnet. Um Mehrfachwechselwirkungen, die die Interpretation der Spektren maßgeblich erschweren, zu vermeiden, werden elektrische Felder mit ultrakurzen Pulsdauern (1 und 5 fs) verwendet. Der Ionisationvorgang wird dabei mithilfe von Momentaufnahmen der Elektronendichte untersucht, wodurch gezeigt wird, wie sich die Ionisationsdynamik für die verschieden polarisierten Felder unterscheidet. Für ein RZP (LZP) Feld zum Beispiel beginnt die Dynamik der Elektronendichte am Kern Z_3 (Z_1) und propagiert anschließend in entgegen dem (in im) Uhrzeigersinn verlaufenden Kreisbewegungen weg vom Kern. Der Ionisationsvorgang an sich findet dabei innerhalb von zwei Halbzyklen ($t < t_0$ und $t > t_0$), im Zeitbereich um t_0 (Zeitpunkt, an dem das elektrische Feld maximal wird), statt. Mit Hilfe der SFN und dem Vektorpotential des elektrischen Feldes $\mathbf{A}(t_0 < t)$ und $\mathbf{A}(t > t_0)$ lässt sich sowohl die relative Lage als auch die Intensität der zwei in den Photoelektronenspektren beobachteten Peaks erklären. Die gefundenen Intensitätsunterschiede werden durch die vorübergehende Bevölkerung der elektronisch angeregten Zustände innerhalb des ersten Halbzyklus und der damit einhergehenden erhöhten Ionisation im zweiten Halbzyklus erzeugt. Die gefundene Doppel-Peak-Struktur hängt dabei stark von der TEP des elektrischen Feldes ab, wobei die Veränderungen in den Photoelektronenspektren sich ebenfalls stark auf die Form des ZDPM auswirkt. Bei Simulationen mit elektrischen Pulsen von 5 fs kommt es zu einer sogenannten *Above threshold ionization* (ATI) Ringstruktur in den Photoelektronenspektren. Die Photoelektronenspektren σ^{LZP} und σ^{RZP} verhalten sich für symmetrische Modellsysteme spiegelsymmetrisch zueinander. Die Spiegelsymmetrie ist dabei unabhängig von den Parametern des elektrischen Pulses. Für asymmetrische Systeme gilt diese Symmetriebeziehung sowohl für die zeitliche Entwicklung der Elektronendichte als auch für die Photoelektronenspektren nicht mehr. Dies führt letzten Endes dazu, dass sich Form des Zirkulardichroismus in den Photoelektronen-Winkelverteilungen signifikant verändert, wobei eine erhöhte Asymmetrie im Modellsystem mit einem verstärkten Zirkular-Dichroismus einhergeht. Die Ursache der komplexen Doppel-Peak-Struktur in den Photoelektronenspektren lässt sich weitestgehend mithilfe der SFN analysieren, wobei jedoch ein detailliertes Bild der Ionisationdynamik immer noch offen bleibt.

Im zweiten Teil dieser Arbeit werden die quantendynamischen Resultate mithilfe von klassischen Trajektorien und einer numerischen Lösung der SFN im Detail analysiert. Die gewählten Methoden sind dabei geeignet um sowohl die langreichweitigen Wechselwirkungen im Kontinuum sowie den Einfluss des Grundzustands auf die finale Impulsverteilung des Photoelektronenspektrums zu untersuchen. Um die Anzahl an angeregten Zuständen systematisch reduzieren zu können, wird die Reichweite des Potenzials artifiziell verringert. Die zeitabhängige Schrödinger-Gleichung wird für solche unterschiedlich weitreichenden Potenziale gelöst und die Resultate mithilfe von klassischen Trajektorien und der SFN

analysiert. Die berechneten Photoelektronenspektren zeichnen sich durch eine ähnliche Dreifach-Peak-Struktur (mit ATI-Ringen) aus, wobei jedoch die relative Lage und die Intensität der drei Peaks für die verschiedenen Systeme voneinander abweichen. Der Ursprung dieser Dreifach-Struktur lässt sich auf drei primäre Ionisationsevents zurückführen, welche mithilfe von drei klassischen Trajektorien simuliert werden. Die repräsentativ gewählten Trajektorien starten dabei zu unterschiedlichen Zeiten von jeweils einem der drei Kerne, da hier die berechneten Breiten der Tunnelbarrieren am kleinsten und die dazugehörigen Ionisationswahrscheinlichkeiten am größten sind. Die finalen Impulse der Trajektorien lassen sich anschließend eindeutig den drei im Photoelektronspektrum beobachteten Peaks zuordnen. Im Vergleich dazu ist die Dreifach-Struktur im Photoelektronenspektrum des symmetrischen Systems mit langreichweitigem Coulomb-Potenzial im Uhrzeigersinn verschoben. Diese Verschiebung lässt sich mithilfe der Coulomb-korrigierten Trajektorien reproduzieren. Zusätzlich weist das Coulomb-System eine "Finger-artige" Struktur bei kleinen Elektronenimpulsen auf, welche durch die Ionisation aus höheren angeregten elektronischen Zuständen hervorgerufen wird. Für symmetrische Systeme verhalten sich die durch LZP- und RZP- Licht erzeugten Photoelektronenspektren spiegelsymmetrisch zueinander. Für asymmetrische Systeme gilt diese Beziehung nicht mehr. Je höher dabei die Asymmetrie im Modellpotenzial ist, desto höher fallen auch die Unterschiede zwischen beiden Spektren aus. In beiden Fällen (σ^{LZP} und σ^{RZP}) verschwindet jedoch die Dreifach-Struktur bei hohen Asymmetrien. Durch die Berücksichtigung des permanenten Dipols in das Trajektorienmodell (über den Stark-Effekt), lassen sich die Resultate der quantendynamischen ab initio Simulationen für kurzreichweitige asymmetrische Potenziale weitestgehend reproduzieren.

Im dritten Teil dieser Arbeit liegt der Fokus auf der Untersuchung der Ionisationsdynamik von dreiatomigen Molekülen mit erhöhten Bindungsabständen und unterschiedlicher räumlicher Orientierung. Dabei werden die Methoden aus dem ersten und zweiten Teil dieser Arbeit so modifiziert, dass eine Beschreibung der Ionisationsdynamik auch für Systeme mit höheren Kernabständen möglich ist. Im Falle hoher Bindungsabstände und kurzreichweitiger Wechselwirkungen werden die Anfangsbedingungen der Trajektorien so gewählt, dass der Ionisationsprozess über den angeregten Zustand vom sogenannten "Up-Field-site"-Kern erfolgt. Im Gegensatz zu Systemen mit kleinen Bindungsabständen, in denen die Ionisation vom sogenannten "Down-Field-site"-Kern erfolgt, starten die hier gewählten Trajektorien zu anderen Zeiten und führen folglich zu einer komplett anderen Photoelektronendynamik. Die klassischen Trajektorien reproduzieren dabei die Evolution der Elektronendichte im Kontinuum, also die quantendynamischen Resultate, sehr gut. Auch die finalen Impulse der Trajektorien sind in sehr guter Übereinstimmung mit der relativen Lage der drei in den Photoelektronenspektren beobachteten Peaks. Eine

Analyse der Dynamik des zeitabhängigen Superpositionszustands $\psi_s(\mathbf{r}, t)$ (für Details siehe Abschnitt 3.3) zeigt, wie sich die relative Lage der dazugehörigen Elektronendichtemaxima während der Propagation verändert. Je nach Länge des Bindungsabstands wird eine starke Lokalisierung der Elektronendichte entweder in Richtung ($R_{ij} = 3.5$ au, "down-field side") oder in entgegengesetzter Richtung ($R_{ij} = 5.5$ au, "up-field side") zum elektrischen Feldvektor beobachtet. Nur der erweiterten Variante der SFN, in der die Ionisation aus dem Superpositionszustand $\psi_s(\mathbf{r}, t)$ erfolgt, gelingt es die komplexe Struktur des aus der Lösung der zeitabhängigen Schrödinger Gleichung berechneten Photoelektronenspektrums erfolgreich zu reproduzieren. Gerade für die hier betrachteten dreiatomigen Systeme nehmen die elektronisch angeregten Zustände folglich eine entscheidende Rolle während des Ionisationsvorgangs ein. Für Coulomb-Systeme mit größerem Bindungsabstand wird die Anfangsbedingung der Trajetorien so gewählt, dass der sogenannte "over-the-barrier" Mechanismus simuliert werden konnte. Die veränderten Startbedingungen der Trajetorien haben zur Folge, dass sich die finalen Impulse der gewählten Trajektorien entgegen dem Uhrzeigersinn verschieben, wobei die in den Photoelektronenspektren beobachteten Peaks eine ähnliche Rotation zeigen. Die Spektren, die aus der erweiterten Version der SFN für Coulomb-Systeme hervorgehen, stimmen sehr gut mit den Resultaten aus den quantendynamischen Rechnungen überein. Das bedeutet, dass die elektronisch angeregten Zustände genau wie die langreichweitigen Wechselwirkungen im Kontinuum eine im Uhrzeigersinn verlaufende Rotation der Peak-Struktur hervorrufen (nur beim kleinem Bindungsabstand). Für asymmetrische Modellsysteme hingegen lässt sich das Intensitätsprofil der quantendynamisch berechneten Photoelektronenspektren nur mithilfe des semi-klassischen Trajektorienmodells reproduzieren, wenn elektrische Felder mit Wellenlängen von $\lambda = 3000$ nm (Tunnelregime) für die Simulationen verwendet werden. Hierbei zeigen klassische Trajektorien, wie sich der Tunnelmechanismus für asymmetrische Systeme verändert, d.h. wie sich die Ionisationswahrscheinlichkeit und die Tunnelzeiten für die drei gewählten Trajektorien verändern. Im Multiphotonenregime ($\lambda = 800$ nm) ist der Beitrag der elektronisch angeregten Zustände zu hoch und das Trajetorienmodell ist nicht mehr in der Lage die komplexe Struktur der quantendynamisch berechneten Photoelektronenspektren zu simulieren. Auch die erweiterte Version der SFN ist nicht in der Lage, die vollständige Struktur des Photoelektronenspektrums zu reproduzieren; sowohl für Modellsysteme mit kurzreichweitigem als auch mit langreichweitigem Potenzial, obwohl hier die signifikant zur Ionisation beitragenden elektronisch angeregten Zuständen in den Rechnungen berücksichtigt werden. Des Weiteren wird untersucht, wie sich die molekulare Orientierung des dreiatomigen Modellsystems auf die Struktur des Photoelektronspektrums auswirkt. Die über alle Raumrichtung des Moleküls gemittelten Photoelektronenspektren besitzen keine Dreifach-Struktur mehr, wohingegen

die ATI-Ring-Struktur erhalten bleibt. Das dazugehörige Intensitätsprofil hängt dabei nur noch von den Parametern des elektrischen Feldes ab. Insbesondere hängt der aus den gemittelten Photoelektronenspektren berechnete ZDPW nur noch von der TE-Phase des elektrischen Feldes ab und verschwindet folglich für sehr hohe Pulsdauern. Der ZDPW unterscheidet sich dabei kaum für symmetrische und asymmetrische Modellsysteme. Das deutet darauf hin, dass der überwiegende Teil des ZDPW nur durch die TE-Phase des elektrischen Feldes und nicht durch das asymmetrische Potenzial erzeugt wird.
Zusammenfassend beleuchten die in dieser Arbeit vorgestellten Ergebnisse die Stark-Feld-induzierte Dynamik von dreiatomigen Systemen in zwei Dimensionen. Insbesondere werden die langreichweitige Wechselwirkung des Photoelektrons im Kontinuum mit dessen Ursprungsion sowie der Einfluss elektronisch angeregter Zustände untersucht. Dazu werden für unterschiedliche Bindungsabstände und räumliche Orientierungen quantendynamische Simulationen durchgeführt und mit klassischen Trajektorien und einer erweiterten Variante der SFN verglichen. Es wird gezeigt, dass der aus den gemittelten Photoelektronenspektren berechnete ZDPW sich für symmetrische und asymmetrische Modellsysteme kaum unterscheidet. Das deutet darauf hin, dass dieser Effekt überwiegend durch die TE Phase des elektrischen Feldes erzeugt wird. Eine detaillierte Analyse der Auswirkung der TE-Phase des elektrischen Feldes auf den Photoelektronen-Zirkularen-Dichroismus (PEZD) würde jedoch eine dreidimensionale Simulation im Feld vierer Kerne erfordern, was jedoch über den Rahmen dieser Arbeit hinaus geht. Eine derartige Ergänzung des hier präsentierten Modells wäre jedoch unkompliziert. Diese Arbeit stellt damit ein wichtiges Fundament für weiterführende Forschung zum PEZD und dem zugrundeliegenden Ionisationsmechanismus dar.

Appendix: 3D Simulations

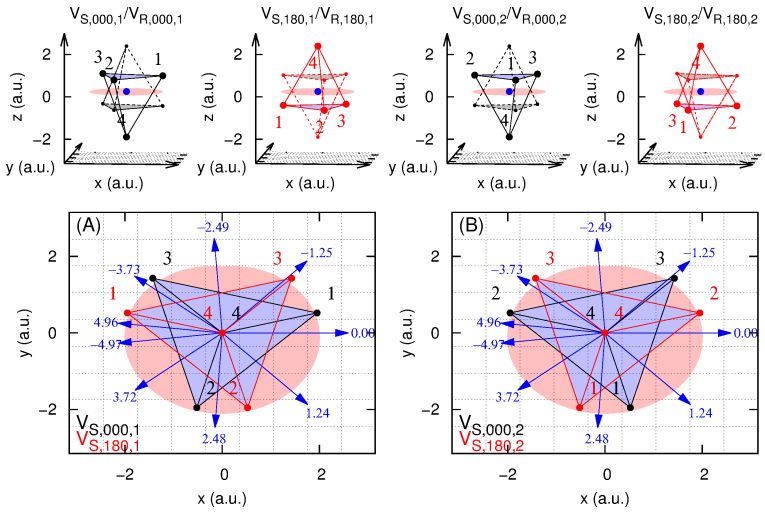

Figure 5.1: Top layer: Four representative molecular orientations $V_{K,000,1}$, $V_{K,180,1}$, $V_{K,000,2}$, and $V_{K,180,2}$ for the S ($K = S$; solid lines) and R enantiomer ($K = R$; dashed lines) of a chiral model molecule, consisting of four nuclei and one single electron. The nuclei ($i = \{1, 2, 3, 4\}$) are represented by the black and red dots, respectively. The electron (blue dot) resides at the orgin of the coordinate system. Bottom layer: Top views of the first two molecular orientations $V_{S,000,1}$, $V_{S,180,1}$ (A), and the other two orientations $V_{S,000,2}$, and $V_{S,180,2}$ (B) of the S-enantiomer model with the electric vector (blue arrows) at certain times t (blue numbers in fs).

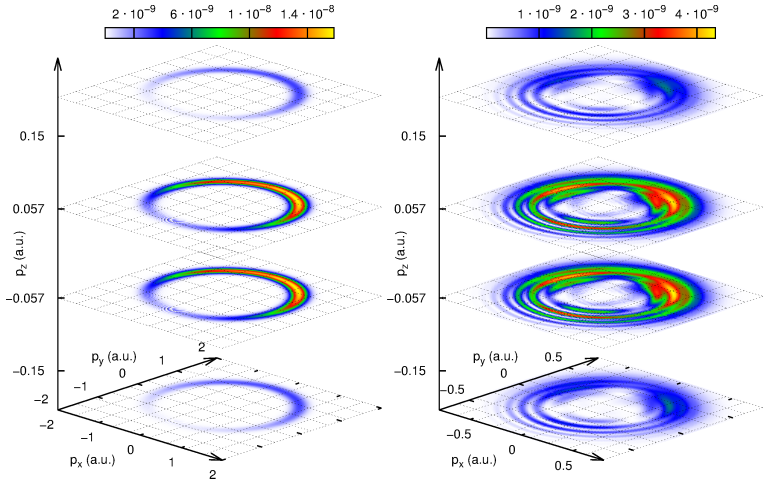

Figure 5.2: Extracts of the full 3D Photoelectron Momentum Distribution (PEMD) for a simulation for a symmetric short-range modelsystem $V_{S,000,1}$ interacting with left-circularly polarized electric fields with wavelengths of $\lambda = 800$ (left column) and $\lambda = 3000$ nm (right column). Shown are four different 2D PEMD slices for different values of p_z.

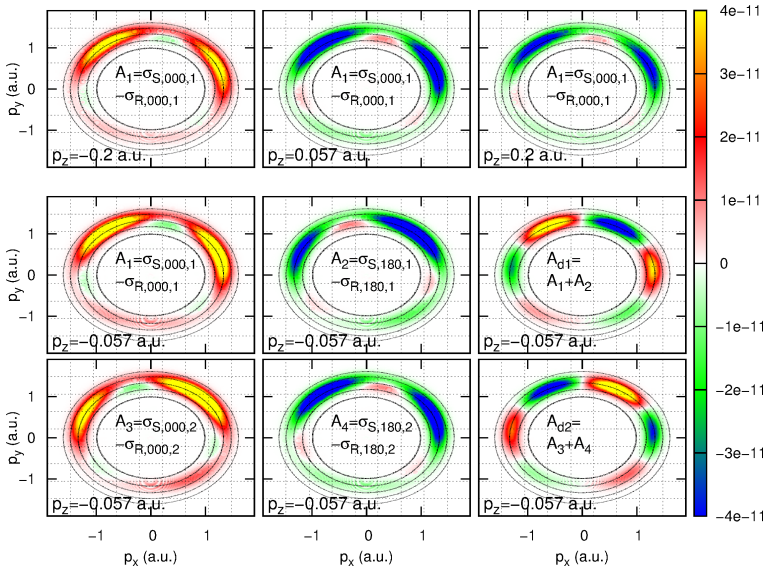

Figure 5.3: Shown are the differences of the 2D Photoelectron momentum distribution slices (for specific p_z) of the S and R molecular configurations $\sigma_{S,K} - \sigma_{R,K}$ for symmetric Coulomb modelsystems, $V_{S,K}$ and $V_{R,K}$, interacting with left-circularly polarized electric fields with wavelengths of $\lambda = 3000$ nm. Differences are shown for four different molecular orientations with $K = \{(000, 1), (180, 1), (000, 2), (180, 2)\}$.

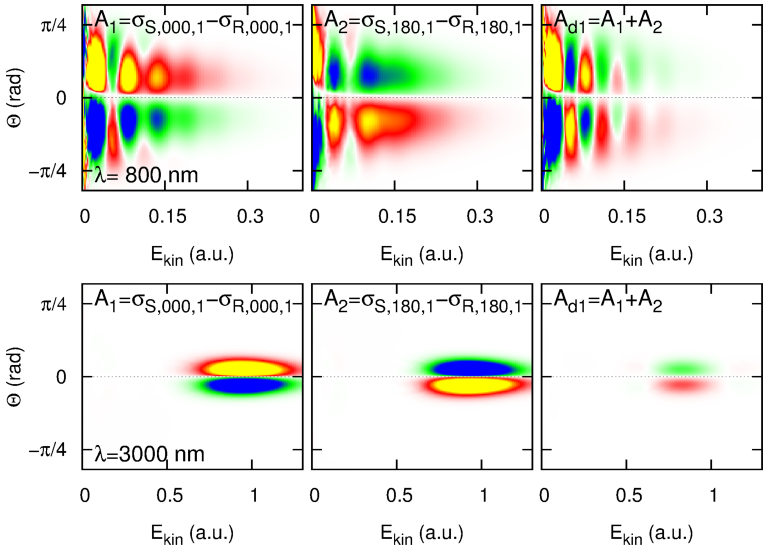

Figure 5.4: Shown are the differences of the 3D Photoelectron momentum distribution $\sigma_{S,K}(E_{kin},\theta) - \sigma_{R,K}(E_{kin},\theta)$ integrated over the azimuthal angle ϕ for symmetric Coulomb model systems, $V_{S,K}$ and $V_{R,K}$, interacting with left-circularly polarized electric fields with wavelengths of $\lambda = 800$ and $\lambda = 3000$ nm. Differences are shown for two different molecular orientations with $K = \{(000,1),(180,1)\}$. E_{kin} is the kinetic energy of the photoelectron and θ is the polar angle, which is defined along the propagation direction of the z axis. This characteristic forward-/backward asymmetry is related to the Photoelectron Circular Dichroism.

Bibliography

[1] Voronov, G. S. & Delone, N. B. Many-photon ionization of the xenon atom by ruby laser radiation. Sov. Phys. JETP **23** (1966).

[2] Voronov, G. S., Delone, G. A., Delone, N. B. & Kudrevatova, O. V. Multiphoton Ionization of the Hydrogen Molecule in the Strong Electric Field of Ruby Laser Emission. JETP Letters **2**, 377 (1965).

[3] Reiss, H. R. Absorption of Light by Light. J. Math. Phys. **59**, 59–67 (2016).

[4] Reiss, H. R. A convergent perturbation expansion in first quantized electrodynamics. J. Math. Phys. **3**, 387–395 (1962).

[5] Bunkin, F. & Prokhorov, A. Excitation and ionization of atoms in a strong radiation field. Sov. Phys. JETP **19**, 739 (1964).

[6] Keldysh, L. V. Ionization in the field of a strong electromagnetic wave. Sov. Phys. JETP **20**, 1307–1314 (1965).

[7] Gordon, W. Der comptoneffekt nach der schrödingerschen theorie. Zeitschrift für Physik **40**, 117–133 (1926).

[8] Berestetskii, V. B., Pitaevskii, L. P. & Lifshitz, E. M. Quantum Electrodynamics: Volume 4 (Course of Theoretical Physics) (Butterworth-Heinemann, 2012).

[9] Feshbach, H., Morse, P. M. & Michio, M. Methods of Theoretical Physics: Part II: Second Edition (Dover Books on Physics) (Dover Publications, 2019).

[10] Popruzhenko, S. V. Keldysh theory of strong field ionization: history, applications, difficulties and perspectives. J. Phys. B: At. Mol. Opt. Phys. **47**, 204001 (2014).

[11] Landau, L. D. & Lifshitz, L. M. Quantum Mechanics: Non-Relativistic Theory (Butterworth-Heinemann, 1981).

[12] Perelomov, A., Popov, V. & Terentev, M. Ionization of atoms in an alternating electric field. Sov. Phys. JETP **23**, 924–934 (1966).

[13] NIKISHOV, A. I. & RITUS, V. I. Ionization of systems bound by short-range forces by the field of an electromagnetic wave. Sov. Phys. JETP **23**, 168–177 (1966).

[14] NIKISHOV, A. I. & RITUS, V. Ionization of atoms by an electromagnetic wave field. Sov. Phys. JETP **25**, 145–156 (1967).

[15] A.M. PERELOMOV, V. S. P. & TERENT'EV, M. V. Ionization of atoms in an alternating electric field: II. Sov. Phys. JETP **24**, 207–217 (1967).

[16] Perelomov, A. M. & Popov, V. S. IONIZATION OF ATOMS IN AN ALTERNATING ELECTRICAL FIELD. III. Sov. Phys. JETP **25**, 336–343 (1967).

[17] Kopold, R., Becker, W. & Kleber, M. Quantum path analysis of high-order above-threshold ionization. J. Phys. B: At. Mol. Opt. Phys. **179**, 39–50 (2000).

[18] Salieres, P. et al. Feynman's Path-Integral Approach for Intense-Laser–Atom Interactions. SCIENCE **292**, 902–906 (2001).

[19] Popov, V. S., Kuznetsov, V. P. & Perelomov, A. M. Quasiclassical approximation for nonstationary problems. JETP **26**, 222–232 (1968).

[20] Popov, V. S. Imaginary-Time Method in Quantum Mechanics and Field Theory. Phys. At. Nuclei **68**, 686–708 (2005).

[21] Popruzhenko, S. V., Mur, V. D., Popov, V. S. & Bauer, D. Strong field ionization rate for arbitrary laser frequencies. Phys. Rev. Lett. **101**, 1–4 (2008).

[22] Popruzhenko, S. V. & Bauer, D. Strong field approximation for systems with Coulomb interaction. J. Mod. Opt. **55**, 2573–2589 (2008).

[23] Popruzhenko, S. B., Mur, V. D., Popov, V. S. & Bauer, D. Multiphoton ionization of atoms and ions by high-intensity X-ray lasers. JETP **108**, 947–962 (2009).

[24] Faisal, F. H. M. Multiphoton transitions. IV. bound-free transition integrals in compact forms. J. Phys. B: At. Mol. Opt. Phys. **6**, 553–558 (1973).

[25] Reiss, H. R. Effect of an intense electromagnetic field on a weakly bound system. Phys. Rev. A **22**, 1786–1813 (1980).

[26] Agostini, P., Fabre, F., Mainfray, G., Petite, G. & Rahman, N. K. Free-free transitions following six-photon ionization of xenon atoms. Phys. Rev. Lett. **42**, 1127–1130 (1979).

[27] Gaponov, A. V. & Miller, M. A. Potential wells for charged particles in a high-frequency electromagnetic field. JETP 242–243 (1958).

[28] Kibble, T. W. B. Mutual refraction of electrons and photons. Phys. Rev. A **150**, 1060–1069 (1966).

[29] Strickland, D. & Mourou, G. Compression of amplified chirped optical pulses. Opt. Commun. **56**, 219 – 221 (1985).

[30] Chin, S., Yergeau, F. & Lavigne, P. Tunnel ionisation of Xe in an ultra-intense CO_2 laser field (10^{14} Wcm^{-2}) with multiple charge creation. J. Phys. B: At. Mol. Opt. Phys. **18**, L213–L215 (1985).

[31] Mainfray, G. & Manus, G. Multiphoton ionization of atoms. Rep. Prog. Phys. **54**, 1333–1372 (1985).

[32] Posthumus, J. H. The dynamics of small molecules in intense laser fields. Rep. Prog. Phys. **67**, 623–665 (2004).

[33] Paulus, G. G. et al. Absolute-phase phenomena in photoionization with few-cycle laser pulses. Nature **414**, 2000–2002 (2001).

[34] Ullrich, J. et al. Recoil-ion and electron momentum spectroscopy: reaction-microscopes. Rep. Prog. Phys. **66**, 1463–1545 (2003).

[35] Lux, C., Wollenhaupt, M., Sarpe, C. & Baumert, T. Photoelectron circular dichroism of bicyclic ketones from multiphoton ionization with femtosecond laser pulses. ChemPhysChem **16**, 115–137 (2015).

[36] Bashkansky, M., Bucksbaum, P. H. & Schumacher, D. W. Asymmetries in above-threshold ionization. Phys. Rev. Lett. **60**, 2458–2461 (1988).

[37] L. Chin, S., Rolland, C., B. Corkum, P. & Kelly, P. Multiphoton ionization of Xe and Kr with intense 0.62 μm femtosecond pulses. Phys. Rev. Lett. **61**, 153–156 (1988).

[38] Goreslavski, S. P., Paulus, G. G., Popruzhenko, S. V. & Shvetsov-Shilovski, N. I. Coulomb asymmetry in above-threshold ionization. Phys. Rev. Lett. **93**, 1–4 (2004).

[39] Popruzhenko, S. V., Kundu, M., Zaretsky, D. F. & Bauer, D. Harmonic emission from cluster nanoplasmas subject to intense short laser pulses. Phys. Rev. A **77**, 1–11 (2008).

[40] Chen, P.-X., Liang, L.-M., Li, C.-Z. & Huang, M.-Q. Necessary and sufficient condition for distillability with unit fidelity from finite copies of a mixed state: The most efficient purification protocol. Phys. Rev. A **66**, 1–4 (2002).

[41] Moshammer, R. et al. Rescattering of ultralow-energy electrons for single ionization of Ne in the tunneling regime. Phys. Rev. Lett. **91**, 113002 (2003).

[42] Dimitriou, K. I., Arbó, D. G., Yoshida, S., Persson, E. & Burgdörfer, J. Origin of the double-peak structure in the momentum distribution of ionization of hydrogen atoms driven by strong laser fields. Phys. Rev. A **70**, 1–4 (2004).

[43] Blaga, C. I. et al. Strong-field photoionization revisited. Nature Physics **5**, 335–338 (2009).

[44] Quan, W. et al. Classical aspects in above-threshold ionization with a midinfrared strong laser field. Phys. Rev. Lett. **103**, 093001 (2009).

[45] Liu, C. & Hatsagortsyan, K. Z. Origin of unexpected low energy structure in photoelectron spectra induced by midinfrared strong laser fields. Phys. Rev. Lett. **105**, 1–4 (2010).

[46] Yan, T.-M., Popruzhenko, S. V., Vrakking, M. J. J. & Bauer, D. Low-energy structures in strong field ionization revealed by quantum orbits. Phys. Rev. Lett. **105**, 253002 (2010).

[47] Saalmann, U. & Rost, J. M. Electron-Energy Bunching in Laser-Driven Soft Recollisions. Phys. Rev. Lett. **108**, 1–4 (2012).

[48] Huismans, Y. et al. Time-resolved holography with photoelectrons. Science **331**, 61–64 (2011).

[49] Kuchiev, M. Y. Atomic antenna. JETP Lett. **45**, 404–406 (1987).

[50] Corkum, P. B. Plasma perspective on strong field multiphoton ionization. Phys. Rev. Lett. **71**, 1994–1997 (1993).

[51] Becker, W., Lohr, A. & Kleber, M. Effects of rescattering on above-threshold ionization. J. Phys. B: At. Mol. Opt. Phys. **27** (1994).

[52] Lewenstein, M., Balcou, P., Ivanov, M. Y., L'Huillier, A. & Corkum, P. B. Theory of high-harmonic generation by low-frequency laser fields. Phys. Rev. A **49**, 2117–2132 (1994).

[53] Becker, W., Long, S. & McIver, J. K. Modeling harmonic generation by a zero-range potential. Phys. Rev. A **50**, 1540–1560 (1994).

[54] Freeman, R. R. et al. Above-threshold ionization with subpicosecond laser pulses. Phys. Rev. Lett. **59**, 1092–1095 (1987).

[55] Becker, W., Chen, J., Chen, S. G. & Milošević, D. B. Dressed-state strong-field approximation for laser-induced molecular ionization. Phys. Rev. A **76**, 1–7 (2007).

[56] Becker, W., Long, S. & McIver, J. Short-range potential model for multiphoton detachment of the H^- ion. Phys. Rev. A **42**, 4416–4419 (1990).

[57] Kiyan, I. & Helm, H. Production of energetic electrons in the process of photodetachment of F^-. Phys. rev. Lett. **90**, 1–4 (2003).

[58] Reichle, R., Helm, H. & Kiyan, I. Y. Detailed comparison of theory and experiment of strong-field photodetachment of the negative hydrogen ion. Phys. Rev. A **68**, 1–11 (2003).

[59] Bergues, B., Ni, Y., Helm, H. & Kiyan, I. Y. Experimental study of photodetachment in a strong laser field of circular polarization. Phys. Rev. Lett. **95**, 1–4 (2005).

[60] Bergues, B., Ansari, Z., Hanstorp, D. & Kiyan, I. Y. Photodetachment in a strong laser field: An experimental test of keldysh-like theories. Phys. Rev. A **75**, 1–11 (2007).

[61] Gazibegović-Busuladžić, A. et al. Electron rescattering in above-threshold photodetachment of negative ions. Phys. Rev. Lett. **104**, 1–4 (2010).

[62] Gribakin, G. F. & Kuchiev, M. Y. Multiphoton detachment of electrons from negative ions. Phys. Rev. A **55**, 3760–3771 (1997).

[63] Borzunov, S. V. et al. Zero-range-potential model for strong-field molecular processes: Dynamic polarizability and photodetachment cross section. Phys. Rev. A **88**, 1–18 (2013).

[64] Kulander, K., Schafer, K. & Krause, K. L. Super-Intense Laser-Atom Physics (Nato Science Series II:) (Springer, 2001).

[65] Paulus, G. G., Becker, W., Nicklich, W. & Walther, H. Rescattering effects in above-threshold ionization: a classical model. J. Phys. B: At. Mol. Opt. Phys. **27**, L703–L709 (1994).

[66] Paulus, G. G., Becker, W. & Walther, H. Classical rescattering effects in two-color above-threshold ionization. Phys. Rev. A **52**, 4043–4053 (1995).

[67] Zhao, J. & Lein, M. Determination of ionization and tunneling times in high-order harmonic generation. Phys. Rev. Lett. **111**, 1–5 (2013).

[68] McDonald, C. R., Orlando, G., Vampa, G. & Brabec, T. Tunnel ionization dynamics of bound systems in laser fields: How long does it take for a bound electron to tunnel? Phys. Rev. Lett. **111**, 1–5 (2013).

[69] Delone, N. B. & Krainov, V. P. Energy and angular electron spectra for the tunnel ionization of atoms by strong low-frequency radiation. J. Opt. Soc. Am. B **8**, 1207–1211 (2008).

[70] Muller, H. G. et al. Attosecond Ionization and Tunneling Delay Time Measurements in Helium. Science **322**, 1525–1529 (2008).

[71] Pfeiffer, A. N. et al. Attoclock reveals natural coordinates of the laser-induced tunnelling current flow in atoms. Nature Physics **8**, 76–80 (2012).

[72] Pfeiffer, A. N., Cirelli, C., Smolarski, M. & Keller, U. Recent attoclock measurements of strong field ionization. Chem. Phys. **414**, 84–91 (2013).

[73] Shvetsov-Shilovski, N. I., Dimitrovski, D. & Madsen, L. B. Ionization in elliptically polarized pulses: Multielectron polarization effects and asymmetry of photoelectron momentum distributions. Phys. Rev. A **85**, 1–11 (2012).

[74] Shvetsov-Shilovski, N. I., Dimitrovski, D. & Madsen, L. B. Ehrenfest's theorem and the validity of the two-step model for strong-field ionization. Phys. Rev. A **87**, 1–16 (2013).

[75] Zuo, T. & Bandrauk, A. D. Charge-resonance-enhanced ionization of diatomic molecular ions by intense lasers. Phys. Rev. A **52**, R2511–R2514 (1995).

[76] Pavičić, D., Kiess, A., Hänsch, T. W. & Figger, H. Intense-laser-field ionization of the hydrogen molecular ions H_2^+ and D_2^+ at critical internuclear distances. Phys. Rev. Lett. **94**, 1–4 (2005).

[77] Bandrauk, A. D. & Sink, M. L. Photodissociation in intense laser fields: Predissociation analogy. J. Chem. Phys. **74**, 1110–1117 (1981).

[78] H. Bucksbaum, P., Zavriyev, A., G. Muller, H. & Schumacher, D. Softening of the H^{2+} molecular bond in intense laser fields. Phys. rev. lett. **64**, 1883–1886 (1990).

[79] Zavriyev, A., Bucksbaum, P. H., Squier, J. & Saline, F. Light-induced vibrational structure in H_2^+ and D_2^+ in intense laser fields. Phys. Rev. Lett. **70**, 1077–1080 (1993).

[80] Busuladžić, M. & Milošević, D. B. Simulation of the above-threshold-ionization experiment using the molecular strong-field approximation: The choice of gauge. Phys. Rev. A **82**, 015401 (2010).

[81] Milošević, D. B. Strong-field approximation for ionization of a diatomic molecule by a strong laser field. Phys. Rev. A **74**, 1–14 (2006).

[82] Bauer, D., Milošević, D. B. & Becker, W. Strong-field approximation for intense-laser–atom processes: The choice of gauge. Phys. Rev. A **72**, 023415 (2005).

[83] Kjeldsen, T. K. & Madsen, L. B. Strong-field ionization of N_2: length and velocity gauge strong-field approximation and tunnelling theory. J. Phys. B: At. Mol. Opt. Phys. **37**, 2033–2044 (2004).

[84] Liu, K. & Barth, I. Identifying the tunneling site in strong-field ionization of $H_2{}^+$. Phys. Rev. Lett. **119**, 1–5 (2017).

[85] KELDYSH, L. V. Ionization in the field of a strong electromagnetic wave. Sov. Phys. JETP **20**, 1307–1314 (1965).

[86] Faisal, F. H. M. Multiple absorption of laser photons by atoms. J. Phys. B: At. Mol. Opt. Phys. **6**, L89–L92 (1973).

[87] Reiss, H. R. Effect of an intense electromagnetic field on a weakly bound system. Phys. Rev. A **22**, 1786–1813 (1980).

[88] Lewenstein, M., Balcou, P., Ivanov, M. Y., L'Huillier, A. & Corkum, P. B. Theory of high-harmonic generation by low-frequency laser fields. Phys. Rev. A **49**, 2117–2132 (1994).

[89] Becker, A. & Faisal, F. H. M. Intense-field many-bodyS-matrix theory. J. Phys. B: At. Mol. Opt. Phys. **38**, R1–R56 (2005).

[90] Kjeldsen, T. K., Bisgaard, C. Z., Madsen, L. B. & Stapelfeldt, H. Influence of molecular symmetry on strong-field ionization: Studies on ethylene, benzene, fluorobenzene, and chlorofluorobenzene. Phys. Rev. A **71**, 013418 (2005).

[91] Hasović, E. & Milošević, D. B. Strong-field approximation for above-threshold ionization of polyatomic molecules. Phys. Rev. A **86**, 043429 (2012).

[92] Jaroń-Becker, A. & Becker, A. Suppressed molecular ionization due to interferences effects. Laser Physics **19**, 1705–1711 (2009).

[93] Ritchie, B. Theory of the angular distribution of photoelectrons ejected from optically active molecules and molecular negative ions. Phys. Rev. A **13**, 1411–1415 (1976).

[94] Cherepkov, N. Circular dichroism of molecules in the continuous absorption region. Chem. Phys. Lett. **87**, 344 – 348 (1982).

[95] Dreissigacker, I. & Lein, M. Photoelectron circular dichroism of chiral molecules studied with a continuum-state-corrected strong-field approximation. Phys. Rev. A **89**, 1–6 (2014).

[96] Lowry, T. M. Optical rotatory power (Dover publications Inc., 1964).

[97] Ai Nguyen, L., He, H. & Pham-Huy, C. Chiral drugs: An overview. Int. J. Biomed. Sci. **2**, 85–100 (2006).

[98] Nahon, L., Garcia, G. A., Harding, C. J., Mikajlo, E. & Powis, I. Determination of chiral asymmetries in the valence photoionization of camphor enantiomers by photoelectron imaging using tunable circularly polarized light. J. Chem. Phys. **125**, 1–14 (2006).

[99] Böwering, N. et al. Asymmetry in photoelectron emission from chiral molecules induced by circularly polarized light. Phys. Rev. Lett. **86**, 1187–1190 (2001).

[100] Powis, I., Harding, C. J., Garcia, G. A. & Nahon, L. A valence photoelectron imaging investigation of chiral asymmetry in the photoionization of fenchone and camphor. ChemPhysChem **9**, 475–483 (2008).

[101] Catone, D. et al. Resonant circular dichroism of chiral metal-organic complex. Phys. Rev. Lett. **108**, 1–5 (2012).

[102] Schönhense, G. Circular dichroism and spin polarization in photoemission from adsorbates and non-magnetic solids. Physica Scripta **T31**, 255–275 (1990).

[103] Westphal, C., Bansmann, J., Getzlaff, M. & Schönhense, G. Circular dichroism in the angular distribution of photoelectrons from oriented co molecules. Phys. rev. lett. **63**, 151—154 (1989).

[104] Sen, A., Pratt, S. T. & Reid, K. L. Circular dichroism in photoelectron images from aligned nitric oxide molecules. J. Chem. Phys. **147**, 013927 (2017).

[105] Reid, K. L. Photoelectron angular distributions. Annu. Rev. Phys. Chem. **54**, 397–424 (2003).

[106] L. Reid, K., J. Leahy, D. & Zare, R. Complete description of molecular photoionization from circular dichroism of rotationally resolved photoelectron angular distributions. Phys. rev. lett. **68**, 3527–3530 (1992).

[107] Jahnke, T. et al. Circular dichroism in K-shell ionization from fixed-in-space CO and N_2 molecules. Phys. Rev. Lett. **88**, 073002 (2002).

[108] Lux, C. et al. Zirkulardichroismus in den photoelektronen-winkelverteilungen von campher und fenchon aus der multiphotonenionisation mit femtosekunden-laserpulsen. Angew. Chem. **124**, 5086 (2012).

[109] Müller, A. D., Artemyev, A. N. & Demekhin, P. V. Photoelectron circular dichroism in the multiphoton ionization by short laser pulses. ii. three- and four-photon ionization of fenchone and camphor. J. Chem. Phys. **148**, 214307 (2018).

[110] Artemyev, A. N., Müller, A. D., Hochstuhl, D. & Demekhin, P. V. Photoelectron circular dichroism in the multiphoton ionization by short laser pulses. i. propagation of single-active-electron wave packets in chiral pseudo-potentials. J. Chem. Phys. **142**, 244105 (2015).

[111] Goetz, R. E., Isaev, T. A., Nikoobakht, B., Berger, R. & Koch, C. P. Theoretical description of circular dichroism in photoelectron angular distributions of randomly oriented chiral molecules after multi-photon photoionization. J. Chem. Phys. **146**, 024306 (2017).

[112] Yuan, K.-J., Lu, H. & Bandrauk, A. D. Photoionization of triatomic molecular ions by intense bichromatic circularly polarized attosecond UV laser pulses. J. Phys. B: At. Mol. Opt. Phys. **50**, 124004 (2017).

[113] Lefebvre, C., Lu, H. Z., Chelkowski, S. & Bandrauk, A. D. Electron-nuclear dynamics of the one-electron nonlinear polyatomic molecule h_3^{2+} in ultrashort intense laser pulses. Phys. Rev. A **89**, 023403 (2014).

[114] Cohen-Tannoudji, C., Dupont-Roc, J. & Grynberg, G. Photons and Atoms: Introduction to Quantum Electrodynamics (Wiley-VCH, 1989).

[115] Jackson, J. D. Historical roots of gauge invariance. Rev. Mod. Phys. **73**, 663–680 (2001).

[116] Jackson, J. D. Classical Electrodynamics Third Edition (Wiley, 1998).

[117] Bandrauk, A. D., Fillion-Gourdeau, F. & Lorin, E. Atoms and molecules in intense laser fields: gauge invariance of theory and models. J. Phys. B: At. Mol. Opt. Phys. **46**, 153001 (2013).

[118] Goldstein, H., Jr., C. P. P. & Safko, J. L. Classical Mechanics (3rd Edition) (Pearson, 2001).

[119] Tannor, D. J. Introduction to Quantum Mechanics: A Time-Dependent Perspective (University Science Books, 2006).

[120] Walser, M. W., Keitel, C. H., Scrinzi, A. & Brabec, T. High harmonic generation beyond the electric dipole approximation. Phys. Rev. Lett. **85**, 5082–5085 (2000).

[121] Reiss, H. R. Limits on tunneling theories of strong-field ionization. Phys. Rev. Lett. **101**, 1–4 (2008).

[122] Chirilă, C. C., Kylstra, N. J., Potvliege, R. M. & Joachain, C. J. Nondipole effects in photon emission by laser-driven ions. Phys. Rev. A **66**, 13 (2002).

[123] Haessler, S., Caillat, J. & Salières, P. Self-probing of molecules with high harmonic generation. J. Phys. B: At. Mol. Opt. Phys. **44**, 203001 (2011).

[124] Kamta, G. L. & Bandrauk, A. D. Three-dimensional time-profile analysis of high-order harmonic generation in molecules: Nuclear interferences in H_2^+. Phys. Rev. A **71**, 053407 (2005).

[125] Kosloff, R. Time-Dependent Quantum-Mechanical Methods for Molecular Dynamics. J. Phys. Chem. **92**, 2087–2100 (1988).

[126] Cooley, J. W. & Tukey, J. W. An Algorithm for the Machine Calculation of Complex Fourier Series. Math. Comput. **19**, 297–301 (1965).

[127] Temperton, C. Self-sorting mixed-radix fast Fourier transforms. J. Comput. Phys **52**, 1–23 (1983).

[128] Nussbaumer, H. J. Fast Fourier Transform and Convolution Algorithms (Springer, 1990).

[129] Dautray, R. Mathematical Analysis and Numerical Methods for Science and Technology (Springer, 2000).

[130] SUZUKI, M. General decomposition theory of ordered exponentials. Proceedings of the Japan Academy, Series B **69**, 161–166 (1993).

[131] Bandrauk, A., Dehghanian, E. & Lu, H. Complex integration steps in decomposition of quantum exponential evolution operators. Chem. Phys. Lett. **419**, 346–350 (2006).

[132] Feit, M. D., Fleck Jr., J. A. & Steiger, A. Solution of the Schrödinger equation by a spectral method. J. Comput. Phys **47**, 412–433 (1982).

[133] Strang, G. On the construction and comparison of difference schemes. SIAM J. Numer. Anal. **5**, 506–517 (1968).

[134] Kosloff, R. & Tal-Ezer, H. A direct relaxation method for calculating eigenfunctions and eigenvalues of the schrödinger equation on a grid. Chem. Phys. Lett. **127**, 223 – 230 (1986).

[135] Tal-Ezer, H. & Kosloff, R. An accurate and efficient scheme for propagating the time dependent schrödinger equation. J. Chem. Phys. **81**, 3967–3971 (1984).

[136] Kosloff, R. & Kosloff, D. Absorbing boundaries for wave propagation problems. J. Comput. Phys **63**, 363 – 376 (1986).

[137] Heather, R. & Metiu, H. An efficient procedure for calculating the evolution of the wave function by fast fourier transform methods for systems with spatially extended wave function and localized potential. J. Chem. Phys. **86**, 5009–5017 (1987).

[138] Keller, A. Asymptotic analysis in time-dependent calculations with divergent coupling. Phys. rev. A **52**, 1450–1457 (1995).

[139] Ivanov, M. Y., Spanner, M. & Smirnova, O. Anatomy of strong field ionization. J. Mod. Opt. **52**, 165–184 (2005).

[140] Press, W. H., Teukolsky, S. A., Vetterling, W. T. & Flannery, B. P. Numerical Recipes in C (2Nd Ed.): The Art of Scientific Computing (Cambridge University Press, New York, NY, USA, 1992).

[141] Gentle, J. E. Random Number Generation and Monte Carlo Methods (Springer, 2004).

[142] M. Frigo, S. G. J. Fftw. ICASSP conference proceedings **3**, 1381 (1998).

[143] Verstraete, M. J. et al. Real-space grids and the Octopus code as tools for the development of new simulation approaches for electronic systems. Phy. Chem. Chem. Phys. **17**, 31371–31396 (2015).

[144] Castro, A., Marques, M. A. L. & Rubio, A. Propagators for the time-dependent Kohn–Sham equations. J. Chem. Phys. **121**, 3425–3433 (2004).

[145] De Giovannini, U. et al. Ab initio angle- and energy-resolved photoelectron spectroscopy with time-dependent density-functional theory. Phys. Rev. A **85**, 1–14 (2012).

[146] Saenz, A. Photoabsorption and photoionization of HeH^+. Phys. Rev. A **67**, 1–10 (2003).

[147] Arbó, D. G. et al. Coulomb-volkov approximation for near-threshold ionization by short laser pulses. Phys. Rev. A **77**, 013401 (2008).

Acknowledgments

First of all, I would like to thank my PhD supervisor Prof. Dr. **Stefanie Gräfe** for the opportunity to persue my PhD in her group at the Friedrich-Schiller-Universität Jena. I am grateful for all her excellent guidance, support, and enthusiasm during the three years, and the fact that she always took the time out of her busy schedule for discussions. Special thanks goes to Dr. **Lun Yue**, who helped me with the numerical aspects of my project in the beginning of my PhD, and to Dr. **Alexander Schubert**, who carefully read and corrected my PhD-thesis. Of fundamental importance for this thesis is Dr. **Stefan Kupfer**; I am very grateful to you for the many things I learned from you since I started my Bachelor program in the field of theoretically chemistry 2013.
Thanks goes to my colleagues, friends and fellow PhD students **Philipp Traber**, **Johannes Steinmetzer**, **Kevin Fiederling**, **Karl Micheal Ziems**, **Friedrich Georg Fröbel**, **Phillip Seeber**, and Dr. **Daniel Kinzel**. You helped me in countless scientific as well as non-scientific issues and made the time in the office more pleasant.
Furthermore, I would like to thank Dr. **Dirk Bender** for support concerning technical issues.

Finally, I would like to thank for financial support within the priority programme QUTIF (SPP) from the German Science Foundation (DFG).

Selbständigkeitserklärung

Ich erkläre, dass ich die vorliegende Arbeit selbstständig und unter Verwendung der angegebenen Hilfsmittel, persönlichen Mitteilungen und Quellen angefertigt habe.

.....	.....
Ort, Datum	Matthias Paul

Erklärung zu den Eigenanteilen

Erklärung zu den Eigenanteilen der Promovendin/des Promovenden sowie der weiteren Doktorandinnen/Doktoranden als Co-Autorinnen/-Autoren an den Publikationen und Zweitpublikationsrechten bei einer kumulativen Dissertation

Für alle in dieser kumulativen Dissertation verwendeten Manuskripte liegen die notwendigen Genehmigungen der Verlage ("Reprint permissions") für die Zweitpublikation vor. Die Co-Autorinnen/-Autoren der in dieser kumulativen Dissertation verwendeten Manuskripte sind sowohl über die Nutzung, als auch über die oben angegebenen Eigenanteile der weiteren Doktorandinnen/Doktoranden als Co-Autorinnen/-Autoren an den Publikationen und Zweitpublikationsrechten bei einer kumulativen Dissertation informiert und stimmen dem zu. Die Anteile der Promovendin/des Promovenden sowie der weiteren Doktorandinnen/Doktoranden als Co-Autorinnen/Co-Autoren an den Publikationen und Zweitpublikationsrechten sind in der kumulativen Dissertation aufgeführt.

.....	.....
Ort, Datum	Matthias Paul

Ich bin mit der Abfassung der Dissertation als publikationsbasierte Dissertation, d.h. kumulativ, einverstanden und bestätige die vorstehenden Angaben.

.....	.....
Ort, Datum	Prof. Dr. Stefanie Gräfe

Curriculum vitae

Pesonal data

Name	Matthias Paul
Birth	11th April 1990, 07973 Greiz
Citizenship	Federal Republic of Germany
Nationality	Germany
personal status	unmarried
Working address	Friedrich-Schiller-University Jena
	Institute of Physical Chemistry
	Helmholtzweg 4, 07743 Jena
E-mail	`m.paul@uni-jena.de`

Scientific experience

2016–2019	Doctoral studies in the group of Prof. Dr. Stefanie Gräfe at the Institute of Physical Chemistry, Friedrich-Schiller-University Jena, Germany

Degrees and education

2013–2016	Studies of Chemistry, Friedrich-Schiller-University Jena, Germany Master of Science (M.Sc.) Masterthesis: "Dynamik an chiralen Modellsystemen"
2010–2013	Studies of Chemistry, Friedrich-Schiller-University Jena, Germany Bachelor of Science (B.Sc.) Bachelorthesis: "Quantenchemische Berechnungen von Ruthenium-Lichtsammeleinheiten"
2006–2009	Berufliches Gymnasium Fachrichtung Technikwissenschaft - Schwerpunkt Elektrotechnik - BSZ e.o.plauen

Civillian Service

2009-2010	Helios Vogtland-Klinikum Plauen

Attented conferences

Mai 2016	QUTIF Annual Meeting ALTES SCHLOSS DORNBURG
September 2016	QUTIF Research School at University of Rostock
February 2017	QUTIF Annual Meeting at Max Planck Institute for the Physics of Complex Systems (MPIPKS), Dresden
September 2017	QUTIF International Conference 2017 in Bad Honnef
February 2018	QUTIF Annual Meeting 2018 at the Center for Free-Electron Laser Science (CFEL), DESY and Universität Hamburg
November 2018	DPG-Tagung: "Forschung-Entwicklung-Innovation", Bad Honnef

Poster Presentations

February 2017	"Strong-field ionization of triatomic model systems by few-cycle circularly polarized laser pulses", Matthias Paul und Stefanie Gräfe, QUTIF Annual Meeting at Max Planck Institute for the Physics of Complex Systems (MPIPKS), Dresden
February 2018	"Imprints of the Molecular Electronic Structure in the Photoelectron Spectra of Strong-Field Ionized Asymmetric Triatomic Model Molecules", Matthias Paul und Stefanie Gräfe, QUTIF Annual Meeting 2018

Complementary training in foreign laboratories

July 2018	Two weeks staying in the group of Prof. Dr. Christiane Koch at the Department of Theoretical Physics III Quantum Dynamics and Control, Universität Kassel, Germany

Teaching experience

2016-2018	Quantum Dynamics practica (Vertiefungsfach; 8^{th} and 9^{th} semester)

Language skills

German	Mother tongue
English	Fluent in writing and speaking
French	Basic knowledge

IT skills

Scientific	Quantum chemistry suites (Gaussian 09, Molcas, Turbomole), Fortran and shell programing, molecular and scientific visualization software (gnuplot, GaussView, Avogadro, gabedit), LaTeX
General	Office suites, Windows and UNIX/Linux based OSs

....

Ort, Datum Matthias Paul

List of Publications

1. Paul, M., Yue, L. and Gräfe, S.
   Strong-field ionization of asymmetric triatomic model molecules by few-cycle circularly polarized laser pulses.
   J. Mod. Opt. **64**, 1104–1111 (2017)

2. Paul, M., Yue, L. and Gräfe, S.
   Imprints of the molecular electronic structure in the photoelectron spectra of strong-field ionized asymmetric triatomic model molecules.
   Phys. Rev. Lett. **120**, 233202 (2018)

3. Paul, M. and Gräfe, S.
   Strong-field ionization dynamics of asymmetric equilateral triatomic model molecules in circularly polarized laser fields
   Phys. Rev. A, (submitted), (2019)